Research Square

Preprints are preliminary reports that have not undergone peer review.
They should not be considered conclusive, used to inform clinical practice,
or referenced by the media as validated information.

# An orally bioavailable allele-selective mutant ATXN1 degrader ameliorates motor and cognitive deficits in a humanized SCA1 knock-in model

**Boxun Lu**

luboxun@fudan.edu.cn

Fudan University https://orcid.org/0000-0002-1675-9340

**Hailiang Tan**

Fudan University

**Xuanle Ji**

Fudan University

**Jiayu Chen**

Fudan University

**Yinkun Luo**

Fudan University

**Yuhua Fu**

Fudan University

**Yimin Sun**

Huashan Hospital

**Jian Wang**

Huashan Hospital

**David Rubinsztein**

University of Cambridge https://orcid.org/0000-0001-5002-5263

**Article**

**Keywords:**

**Posted Date:** November 19th, 2026

**DOI:** https://doi.org/10.21203/rs.3.rs-11461952/v1

**License:** This work is licensed under a Creative Commons Attribution 4.0 International License.
Read Full License

**Additional Declarations: Yes** there is potential Competing Interest. DCR has consulted for or is a consultant for Drishti Discoveries, PAQ Therapeutics, MindRank AI, Retro Biosciences, Alexion Pharma International Operations Limited, Carlyle Investment Management LLC, Aladdin Healthcare Technologies Ltd, Nido Biosciences, ProtosBio, and is a co-founder of Acuity Technologies Ltd. BL has consulted for and is a shareholder of PAQ Therapeutics and Shanghai ATTEC Biotechnology Co., Ltd.

# An orally bioavailable allele-selective mutant ATXN1 degrader ameliorates motor and cognitive deficits in a humanized SCA1 knock-in model

Hailiang Tan[1,2]†, Xuanle Ji[1,2]†, Jiayu Chen[1,2], Yinkun Luo[1,2], Yuhua Fu[1,2], Yimin Sun[1], Jian Wang[1]*, David Rubinsztein[3,4]*, Boxun Lu[1,2]*

[1]Neurology Department at Huashan Hospital, State Key Laboratory of Brain Function and Disorders and MOE Frontiers Center for Brain Science, School of Life Sciences, Fudan University, Shanghai, China.
[2]New Cornerstone Science Laboratory, Fudan University; Shanghai, 200438, China.
[3]Cambridge Institute for Medical Research (CIMR), Department of Genomic Medicine, University of Cambridge; Cambridge CB2 0XY, UK.
[4]UK Dementia Research Institute, Cambridge Institute for Medical Research (CIMR), University of Cambridge; Cambridge CB2 0XY, UK.

*Corresponding author. Email: wangjian_hs@fudan.edu.cn (Jian Wang); dcr1000@cam.ac.uk (David Rubinsztein); luboxun@fudan.edu.cn (Boxun Lu).
†These authors contributed equally to this work.

## Abstract

Spinocerebellar ataxia type 1 (SCA1) is a monogenic fatal neurodegenerative disorder that currently has no disease-modifying therapies. SCA1 is mainly driven by the accumulation of mutant Ataxin-1 protein (mATXN1) containing an expanded polyglutamine (polyQ) stretch, whereas its wild-type version (wtATXN1) has important neuronal and molecular functions. Similar scenarios apply to other polyQ diseases, such as Huntington's disease (HD) and several other types of SCAs. Thus, allele-selective mATXN1 lowering with orally available small molecule compounds is highly desirable, in order to avoid deleterious consequences of wtATXN1 depletion. Here, we identified the compound 715, a novel oxindole-derived, brain-penetrant, and orally available degrader that lowers both soluble and aggregated mATXN1 in an allele-selective manner. Mechanistically, 715 enhanced proteasomal but not autophagic degradation of mATXN1 by elevating its poly-ubiquitination. A ubiquitin-focused CRISPR screen identified BIRC7 as the primary E3 ligase mediating 715-induced mATXN1 poly-ubiquitination and clearance. Intraperitoneal administration of 715 significantly reduced cerebellar mATXN1 by 40-60% within 10 days and partially rescued motor deficits over 30-day dosing in *Atxn1*$^{154Q/2Q}$ knock-in mice. To improve translational assessment, we generated and characterized a humanized *Atxn1*$^{h60Q/2Q}$ knock-in model carrying a clinically representative polyQ length (60Q), in which 715 lowered endogenous mATXN1 and substantially improved motor coordination, spatial learning, and cerebellar Purkinje cell pathology. Notably, a 40-day oral dosing regimen of 715 achieved 30-40% cerebellar mATXN1 clearance and comparable functional rescue with a favorable long-term safety profile, highlighting the translational potential of the allele-selective lowering of mATXN1, even to a modest degree. Together, we identified 715 as an orally active therapeutic lead compound, providing potential new entry points for SCA1 treatment.


## INTRODUCTION

Spinocerebellar ataxia type 1 (SCA1) is a devastating, dominantly inherited neurodegenerative disorder caused by the expansion of a polyglutamine (polyQ) tract within the Ataxin-1 (ATXN1) protein[1]. The toxic accumulation and aggregation of mutant ATXN1 (mATXN1) predominantly drive the degeneration of cerebellar Purkinje cells, leading to progressive motor incoordination, cognitive decline, and ultimately premature death[2]. Currently, there are no FDA-approved disease-modifying treatments for SCA1 and clinical management remains strictly palliative[3,4]. While gene therapies such as antisense oligonucleotides (ASOs) targeting ATXN1 have shown preclinical efficacy and entered early-phase clinical evaluation[5], their reliance on intrathecal delivery hinders regular administration at home, motivating efforts to develop orally bioavailable, brain-penetrant alternatives. In addition, given the extensive sequence similarity between mutant and wild-type ATXN1 alleles, nonselective ATXN1-lowering strategies may also reduce wtATXN1. This may carry potential risks because wtATXN1 has important neuronal and molecular functions[6-8]. For example, *Atxn1*-null mice exhibit impaired spatial learning, reduced hippocampal paired-pulse facilitation, and compromised rotarod performance, supporting a role for wtATXN1 in hippocampal synaptic function, learning and memory, and motor performance[6]. Moreover, wtATXN1 participates in native nuclear protein complexes involved in transcriptional regulation, including interactions with the transcriptional repressor Capicua/CIC, and partial loss of normal ATXN1 function has been implicated in transcriptional dysregulation during SCA1 pathogenesis[7,8].

While recent efforts have explored polyQ degraders for conditions like Huntington's disease[9], compounds specifically validated for the unique structural context of ATXN1 are exceedingly rare. Furthermore, the preclinical evaluation of candidate drugs heavily relies on models with extreme,

supraphysiological polyQ expansions within the murine *Atxn1* locus (e.g., the severe *Atxn1*$^{154Q/2Q}$ knock-in mice)[10]. Although these models are invaluable for accelerating phenotypic screening due to their rapid and severe onset, their murine sequence context and accelerated disease progression driven by extreme polyQ lengths may have limitations in recapitulating the protracted, progressive nature of the human disease observed with more common clinical repeat ranges. To improve translational assessment, candidate degraders must be rigorously evaluated in humanized knock-in (KI) models carrying repeat lengths closer to the human disease range, such as 40–80Q, a critical step for establishing their clinical relevance[10,11].

To address these multidimensional challenges, we optimized a polyQ-binding scaffold that we have previously identified[9] to generate 715 ((Z)-3-((3-amino-5-fluorophenyl)((1-methyl-1H-pyrazol-4-yl)amino)methylene)-5-bromoindolin-2-one), an oxindole-derived, brain-penetrant small-molecule degrader of mATXN1. We further investigated the underlying mechanism of action, supporting a dependence on the BIRC7 E3 ligase, and evaluated its potential therapeutic effects *in vivo*.

# RESULTS

## Identification of AN1 and its optimized derivative 715 as potent, allele-selective mATXN1 degraders

We previously identified a class of oxindole-derived compounds that may interact with the expanded polyQ tract and lead to allele-selective degradation of the HD-causing mutant protein, HTT[9]. Consistent with this, AN1 (3-5-bromo-3-((3-bromo-4,5-dihydroxyphenyl)methylidene)-1H-indol-2-one), a compound from this series, also effectively reduced mutant ATXN1 (mATXN1) levels in Daoy stable cells (Fig. 1A & S1A-B, $DC_{50}$ ~3 μM). Daoy is a human cerebellar medulloblastoma cell line that possesses neuronal precursor characteristics[12], and has recently been adopted as a cellular model for spinocerebellar ataxia type 1 (SCA1)[13], a disease caused by polyglutamine expansion in ATXN1[1]. We therefore established Daoy lines stably expressing mutant ATXN1 harboring an expanded polyglutamine tract (72Q or 60Q). We further optimized AN1 and identified a novel derivative 715 that exhibited greater mATXN1-lowering potency (Fig. 1B & S1C, $DC_{50}$ ~200 nM). The mATXN1-lowering effect is unlikely to be caused by a reduction in cell viability as measured by CellTiter-Glo assays (Fig. S1D). Both AN1 and 715 induced a robust, dose- and time-dependent degradation of mATXN1 in Daoy stable cells in an allele-selective manner (Fig. 1A-B & S1A), leaving endogenous wtATXN1 levels unchanged or only minimally affected. The observed selective preservation of wtATXN1 is desirable for potential therapeutic development, given the important and disease-associated functions of wtATXN1.

We next performed live-cell imaging to visualize the temporal trajectory of ATXN1 lowering in cells. In Daoy cells expressing ATXN1-72Q-GFP, AN1 and 715 treatments caused a progressive decline in GFP fluorescence, beginning within 4–8 h and leading to marked signal loss over 24 h without significantly affecting cell confluence (Fig. 1C & S1E), consistent with the Western blot analyses (Fig. 1A-B). In contrast, fluorescence from ATXN1-2Q-GFP remained largely stable under identical treatment conditions, fluctuating by less than 20% throughout the imaging period (Fig. 1D). Thus, real-time imaging confirmed that the allele-selective effect observed by Western blotting was preserved in live cells.

Given the significantly enhanced degradative potency achieved by 715, we prioritized this optimized derivative for advanced profiling in more physiologically relevant and demanding contexts. Consistent with our observations in Daoy cells, treatment with 715 led to a dose-dependent reduction of the mATXN1 level in lentivirus-infected primary mouse cortical neurons expressing ATXN1-72Q-GFP, without causing detectable neuronal loss within the concentration range tested (Fig. 1E & S1F).

Extending these observations to human disease-derived cellular models, we next examined the activity of 715 in fibroblasts obtained from SCA1 patients carrying expanded ATXN1 alleles. Across two independent patient-derived fibroblast lines harboring *ATXN1*$^{29Q/57Q}$ or *ATXN1*$^{28Q/49Q}$ genotypes, 715 treatment led to a measurable dose-dependent reduction of expanded ATXN1 protein levels (Fig. 1F-G). Importantly, treatment with 715 did not affect the viability of wild-type primary dermal fibroblasts within the tested concentration range (Fig. S1G), indicating that the observed ATXN1-lowering activity is not associated with generalized fibroblast toxicity. Together, these findings demonstrate that 715 maintains its mATXN1-lowering activity across distinct cellular contexts, including patient-derived SCA1 models carrying clinically relevant polyQ expansions.

Furthermore, to evaluate the proteome-wide selectivity of our lead compound 715, we performed global quantitative proteomic analyses in both wild-type Daoy cells and Daoy stable cells expressing ATXN1-72Q. Remarkably, in wild-type Daoy cells, 715 induced minimal proteome-wide perturbation and no significant changes in wtATXN1 (Fig. S2A). In ATXN1-72Q-expressing cells, 715 led to substantial downregulation of the ATXN1 level with minimal off-target changes (Fig. S2B), with only a few additional proteins showing significant downregulation. A technical limitation of conventional proteomic analyses of polyQ proteins is that peptide-level quantification generally cannot distinguish wild-type from mutant alleles when the two proteins differ only in the length of the polyQ tract, as previously noted for mutant and wild-type HTT[9]. To overcome this, we quantified the ratio of mutant to wild-type ATXN1 using parallel Western blot densitometry from the identically treated samples (Fig. S2C). By mathematically projecting this ratio onto the mass spectrometry readouts, we calculated a virtual quantitative value for ATXN1-72Q by subtracting the predicted contribution of wtATXN1 in these cells, resulting in a predicted position in the volcano plot that provides a more accurate estimation of the ATXN1-72Q change (Fig. S2B, point indicated by the purple arrow). This analysis identified ATXN1-72Q as the most significantly altered protein following 715 treatment. Apart from ATXN1-72Q, only very few proteins, including COL1A1/2, PDCD4, and UBALD2, showed relatively pronounced decreases. Unlike the polyQ length-dependent ATXN1 decrease, these proteins were lowered by 715 in both wild-type and ATXN1-72Q-expressing Daoy cells. These shared changes likely reflect limited ATXN1-independent cellular responses, such as extracellular matrix remodeling or adaptive proteostasis regulation, rather than broad proteome-wide destabilization[14-16]. Together, these data support the high proteome-wide selectivity of 715 in vitro, with minimal evidence of non-specific proteotoxicity.

Based on its superior potency, high selectivity, and favorable cellular tolerability, 715 was designated as our definitive therapeutic lead for further characterization of its activity across the complex physical states of mATXN1 and for subsequent *in vivo* evaluation. Meanwhile, both AN1 and 715 were retained as valuable pharmacological tools to dissect the fundamental degradation mechanism underlying this oxindole series in our subsequent *in vitro* studies.

## 715 degrades both diffuse and aggregate-associated mutant ATXN1 across distinct subcellular localizations

Because mATXN1 toxicity is influenced by nuclear localization and by the aggregation/solubility state of the mutant protein[2,10], we first investigated whether the degradative action of 715 was restricted to specific subcellular compartments. We deleted the nuclear localization signal of mATXN1 (ΔNLS), which predominantly redistributed the mutant protein to the cytoplasm (Fig. S3A). Although ΔNLS increased the basal expression level of ATXN1-72Q, treatment with 715 still resulted in a significant reduction of the cytoplasmic mATXN1 species (Fig. 2A). This indicates that the degradative efficacy of 715 is not restricted to nuclear-localized mATXN1.

Intracellular mutant ATXN1 is highly prone to forming protein aggregates with varying physical properties[1,2]. To assess whether 715 preferentially affects a specific mATXN1 population, we first performed detergent-based fractionation to separate Daoy ATXN1-60Q cell lysates into NP-40-soluble and SDS-soluble fractions. Western blot analyses revealed that 300 nM 715 significantly reduced mATXN1 levels in both fractions (Fig. 2B), suggesting that 715 targets mATXN1 across distinct solubility states. We next examined the effect of 715 on highly insoluble ATXN1 species in Daoy ATXN1-72Q cells using mild RIPA lysis followed by ultracentrifugation, which separated cell lysates into soluble supernatant and insoluble pellet fractions. In the insoluble fraction, ATXN1 signals retained at the gel wells were detected, and both soluble mATXN1 levels and insoluble gel-well-retained ATXN1 species were significantly reduced following 715 treatment (Fig. 2C). Together, these results demonstrate that 715 reduces mATXN1 across different biochemical states, including soluble and aggregation-associated populations. To further investigate the effect of the compound on the microscopic physical state of these aggregates, we performed fluorescence recovery after photobleaching (FRAP) assays. Following photobleaching, 2Q-GFP rapidly recovered to over 80% of its initial fluorescence within approximately one minute, indicative of a highly dynamic, liquid-like state[17]. In contrast, 72Q-GFP showed markedly slower and incomplete recovery, plateauing at only ~20%, consistent with the formation of dense, poorly dynamic aggregates[18]. Interestingly, after a short-term (3 h) treatment with 715, the 72Q-GFP aggregates exhibited an even more restricted fluorescence recovery curve (Fig. 2D). This phenomenon could occur if 715 dissociated and then degraded the relatively loosely packed protein molecules on the surface of the mATXN1 aggregates, leaving behind a denser, less dynamic aggregate core. The altered recovery kinetics may also reflect changes in the equilibrium between soluble and aggregated mATXN1 pools following compound treatment.

Building upon these observations regarding the physical properties of the aggregates, we subsequently employed time-lapse confocal microscopy to spatiotemporally track the degradation of mATXN1 aggregates (Fig. 2E). To quantitatively assess this process, we independently measured the overall ATXN1 fluorescence intensity and the fluorescence signal specifically localized to the aggregates (puncta) in ATXN1-72Q cells. The results revealed that 715 treatment significantly reduced the overall mATXN1 fluorescence intensity, and remarkably, the decline in the puncta-specific signal occurred largely synchronously with the decrease in overall fluorescence (Fig. 2F). Taken together, these data demonstrate that 715 efficiently targets mATXN1 across distinct subcellular localizations and physical states, including both soluble and aggregate-associated species.

## AN1 and 715 promote mutant ATXN1 degradation via the ubiquitin-proteasome system rather than autophagy

To delineate the mechanisms underlying the clearance of mATXN1 by this oxindole series, we utilized AN1 and 715 to interrogate the relevant degradation pathways. Quantitative PCR (qPCR) analysis revealed that treatment with AN1 or 715 did not significantly alter the mRNA levels of ATXN1-72Q (Fig. 3A), suggesting that the reduction of mATXN1 is not attributable to decreased transcript abundance. This was further corroborated by cycloheximide (CHX) chase assays. By utilizing CHX to block de novo protein synthesis, we still observed compound-induced mATXN1 reduction, supporting accelerated clearance of pre-existing mATXN1 protein (Fig. 3B & S4A-B).

We next investigated the two major intracellular protein clearance systems: the autophagy-lysosome pathway and the ubiquitin-proteasome system (UPS). We first tested autophagy, the anticipated degradation mechanism based on our previous studies of mHTT degradation induced by similar compounds with the arylidene-indolinone scaffold[9]. Surprisingly, the degradative effects of

both compounds were not hindered by autophagy-lysosome inhibitors ($NH_4Cl$, chloroquine, and bafilomycin A1), genetic ablation of the key autophagy gene *ATG5*[19], or siRNA-mediated knockdown of LC3, a canonical autophagosome-associated protein[20] (Fig. 3C-D & S5A). Conversely, co-treatment with the proteasome inhibitor MG132 substantially reversed this reduction in mATXN1 levels (Fig. 3B). Furthermore, a second proteasome inhibitor, epoxomicin, as well as the E1 ubiquitin-activating enzyme inhibitor TAK-243[21], similarly impaired compound-induced mATXN1 degradation (Fig. 3E). Consistent with this, genetic knockdown of the 20S proteasome subunit PSMA7 also markedly attenuated AN1/715-induced clearance of ATXN1-72Q-GFP (Fig. 3F), providing an orthogonal genetic confirmation of proteasome dependence. These data indicate that AN1 and 715 promote mATXN1 degradation predominantly through a ubiquitin-proteasome-dependent mechanism.

Given that TAK-243 impaired compound-induced mATXN1 degradation and that ubiquitination serves as a canonical signal for proteasomal degradation, we next assessed whether 715 preferentially enhances this modification on mutant ATXN1. In the presence of MG132, 715 treatment significantly increased ubiquitin modification of ATXN1-60Q, whereas the corresponding signal on non-expanded ATXN1-2Q remained largely unchanged (Fig. 3G). This polyQ-expanded ATXN1-selective enhancement is consistent with the observed selective degradation of mATXN1 and provides biochemical evidence supporting ubiquitin-proteasome-mediated clearance of the mutant protein.

Since targeted protein degradation and small-molecule-induced clearance have been linked to several specific pathways involving E3 ligases, chaperones, and molecular glues in the literature, we systematically tested whether AN1/715 co-opt any of these previously implicated routes to define the specificity of their mechanism. Many E3 ligases and molecular chaperones, such as TRIM11, TRIM21, MDM2, STUB1, and HSP70, have been previously established as key regulators of mutant ATXN1 stability and aggregation[22-26]. We therefore hypothesized that our compounds might co-opt these canonical pathways. However, siRNA-mediated depletion of TRIM11, TRIM21, and STUB1, or pharmacological inhibition of MDM2 (with Nutlin-3) and HSP70 (with VER-155008), failed to impede the degradative efficacy of AN1/715 (Fig. S5A, S5B, S5D, S5E, S5F). We also examined the substrate-extracting AAA+ ATPase VCP/p97. Blocking VCP/p97 led to a striking accumulation of baseline mATXN1 (without altering mRNA levels) but only partially abrogated the AN1/715-induced clearance (Fig. S5B-C), indicating that VCP/p97 contributes to, but is not strictly required for, AN1/715-induced mATXN1 clearance. This partial dependence is consistent with the established role of VCP/p97 as a ubiquitin-directed segregase/unfoldase that facilitates the proteasomal processing of ubiquitinated or aggregate-associated substrates[27,28]. Together with our earlier observation that 715 reduces aggregation-associated mATXN1 species (Fig. 2B-C, 2E-F), these findings support the idea that the aggregate-associated mATXN1 populations targeted by this compound series may, at least in part, require VCP/p97-facilitated processing before proteasomal degradation. In addition, broad pharmacological inhibition of HECT-family E3 ligases with Heclin did not impair AN1/715-induced degradation (Fig. S5G), further excluding this class of E3 ligases.

Furthermore, PML has been shown to associate with mutant ATXN1 inclusions and has been implicated in the recognition and clearance of misfolded, aggregate-prone nuclear proteins[29]. In the context of SCA1, PML promotes SUMOylation of pathogenic ATXN1 and facilitates its subsequent RNF4-dependent ubiquitination and proteasomal degradation[29]. We therefore investigated whether this PML-SUMO-RNF4 regulatory axis contributes to AN1/715-induced mATXN1 clearance. However, knockdown of PML or DAXX, a PML nuclear body-associated protein[30], the STUbL RNF4, or SUMO1/2/3 had no discernible impact on the degradative effects of either compound (Fig. S5B, S5D).

Structurally, both AN1 and 715 contain an arylidene-indolinone scaffold with an α, β-unsaturated carbonyl (Michael acceptor) moiety, a chemical feature shared by several reported molecular glues that recruit the DCAF11 substrate receptor of the Cullin-RING ligase 4 (CRL4) complex[31,32]. We therefore first examined whether DCAF11 serves as a substrate receptor for AN1/715-mediated mATXN1 degradation. However, direct silencing of DCAF11 failed to impair compound-induced mATXN1 clearance (Fig. S5H), arguing against a DCAF11-dependent mechanism. To further determine whether the broader Cullin-RING ligase (CRL) machinery contributes to this process, we globally inhibited CRL activity through blockade of cullin neddylation using pevonedistat (MLN4924). This intervention likewise did not prevent AN1/715-induced mATXN1 degradation (Fig. S5F), demonstrating that the degradation mechanism is independent of the canonical CRL-neddylation pathway. Collectively, these negative results across multiple candidate pathways suggest that AN/715 operates through an unconventional proteasomal degradation mechanism. By excluding previously characterized ATXN1 clearance pathways and canonical CRL-dependent molecular glue receptors, our findings point to the involvement of an alternative or previously uncharacterized E3 ligase involved in mATXN1 degradation.

## A functional CRISPR screen reveals BIRC7 as the primary E3 ligase for 715-induced mATXN1 clearance

To elucidate the molecular machinery co-opted by 715, we conducted a functional CRISPR-Cas9 knockout screen utilizing a human ubiquitin-related gene sgRNA library in Daoy ATXN1-72Q-GFP-p2A-mCherry cells (Fig. 4A, schematic was prepared using Biorender). To isolate the key regulators, we analyzed sgRNA enrichment in the 715-resistant cell population (retaining high ATXN1-72Q-GFP signal alongside stable mCherry expression), ranking candidate genes by DrugZ analysis (Fig. 4B). By focusing on the E3 ubiquitin ligase family, we sought to identify the principal mediators of 715-induced degradation.

To maximize the likelihood of identifying the key mediator of 715-induced mATXN1 clearance, we assembled a candidate pool for downstream validation from the top-ranked E3 ligase hits of the CRISPR screen. To assess the functional relevance of these candidates, we systematically knocked them down and employed the Incucyte live-cell imaging system to dynamically monitor their effects on 715-induced degradation of ATXN1-72Q-GFP in Daoy stable cells (Fig. 4C). Among the tested E3 ligase candidates, knockdown of BIRC7, also known as Livin, an inhibitor-of-apoptosis protein with E3 ubiquitin ligase activity[33], most strongly impaired 715-induced ATXN1-72Q-GFP clearance (Fig. 4C; siRNA knockdown efficiency validated in Fig. 4D). We then validated the discovery by an independent Western blot approach and confirmed that BIRC7 knockdown largely abolished 715-induced degradation of ATXN1-72Q-GFP (Fig. 4E), supporting a role for BIRC7 in mediating 715-induced mATXN1 clearance. In contrast, knockdown of the other candidate E3 ligases produced little or no attenuation of 715 efficacy (Fig. 4C). Thus, BIRC7 is likely the primary E3 ligase mediating 715-induced mATXN1 degradation.

To further establish a biochemical link between BIRC7 and 715-induced clearance, we examined the ubiquitination status of mutant ATXN1. Western blot analysis revealed that under proteasomal blockade with MG132, the 715-induced increase in mATXN1 polyubiquitination was significantly attenuated by BIRC7 knockdown (Fig. 4F), indicating that BIRC7 is required for 715-induced ubiquitination of the mutant protein. We next investigated whether 715 promotes the association between BIRC7 and expanded ATXN1. Co-immunoprecipitation analysis revealed that 715 treatment significantly enhanced the interaction between BIRC7 and ATXN1-72Q-GFP, whereas the association between BIRC7 and ATXN1-2Q-GFP remained largely unchanged (Fig. 4G). These

findings indicate that 715 preferentially enhances the association between BIRC7 and expanded ATXN1, providing biochemical support for a BIRC7-dependent ubiquitination mechanism underlying mATXN1 degradation.

Finally, to further investigate whether 715 engages its targets, we performed a cellular thermal shift assay (CETSA). Treatment with 715 reduced the thermal stability of ATXN1-72Q, consistent with compound-induced engagement and conformational modulation of the mutant protein (Fig. 4H-I). In contrast, the polyglutamine-binding protein PQBP1, which has been reported to associate with expanded ATXN1 through its polyQ-binding activity[34], increased ATXN1-72Q thermal stability and served as a positive control for ATXN1-targeting thermal shifts (Fig. 4H-I). Notably, CETSA shifts can occur in either direction depending on how a ligand influences protein conformation or molecular interactions. Therefore, the decreased thermal stability induced by 715 is compatible with its role as a degrader and may reflect compound-induced conformational changes in mATXN1 associated with its subsequent BIRC7-dependent ubiquitination and proteasomal degradation. Together, these data indicate that 715 promotes BIRC7-dependent mATXN1 polyubiquitination and proteasomal degradation.

**Intraperitoneal administration of 715 selectively lowers cerebellar mutant ATXN1 and improves behavioral deficits in *Atxn1*$^{154Q/2Q}$ mice**

Building upon its demonstrated *in vitro* efficacy and the characterization of its targeted degradation mechanism, we next evaluated the i*n vivo* therapeutic potential of 715. We utilized the *Atxn1*$^{154Q/2Q}$ knock-in mouse model, a classical and widely recognized *in vivo* platform for SCA1 research[10], which recapitulates the severe, early-onset motor phenotypes and core cerebellar pathology of the disease. To ensure precise and high-throughput quantification of mATXN1 *in vivo*, we established and validated an electrochemiluminescence-based Meso Scale Discovery (MSD) assay (Fig. 5A, schematic was prepared using BioGDP (Generic Diagramming Platform)[35]). This platform demonstrated sufficient sensitivity and a linear dynamic range for detecting mATXN1 in brain homogenates (Fig. S6), providing a reliable tool for our pharmacodynamic evaluations. Single-dose pharmacokinetic (PK) analysis further demonstrated appreciable brain exposure of 715 following i.p. administration, confirming its ability to penetrate the blood-brain barrier (BBB) (Fig. S7A-B, the schematic in Fig. S7A was prepared using BioGDP (Generic Diagramming Platform)[35]) and supporting subsequent evaluation of its cerebellum mATXN1-lowering efficacy.

To directly evaluate the *in vivo* degradative efficacy of 715, *Atxn1*$^{154Q/2Q}$ mice of both sexes received daily intraperitoneal (i.p.) injections of 715 or vehicle for 10 consecutive days. Following this short-term treatment regimen, 715 treatment resulted in an approximately 40-60% reduction in cerebellar mATXN1 levels across both sexes, as quantified by MSD and independently confirmed by Western blot analysis (Fig. 5B-D). Importantly, mirroring our *in vitro* findings, this i*n vivo* degradation was highly allele-selective; the levels of endogenous wild-type ATXN1 (2Q) remained unperturbed following 715 treatment (Fig. 5C-D). These data demonstrate that the brain exposure achieved by 715 is sufficient to engage its target within the disease-vulnerable cerebellum and promote selective mATXN1 clearance *in vivo*.

We then investigated whether this biochemical clearance could translate into meaningful phenotypic benefits. Following a chronic i.p. administration paradigm, we evaluated the motor coordination and behavioral profiles of the mice. In the accelerating rotarod test, we noted a baseline sex difference, where male mutant mice exhibited more severe motor deficits compared to their female counterparts (Fig. 5E). This male-predominant motor phenotype is consistent with a recent report of sex differences in an SCA1 knock-in mouse model, in which male mice similarly displayed

worse motor performance and greater cerebellar microglial activation[36]. Consistent with this baseline difference, the therapeutic benefit of 715 on rotarod performance was predominantly observed in male mice, which maintained their balance on the rod for significantly longer durations compared to vehicle-treated mutant littermates (Fig. 5E). In contrast, the improvement in female mice was not statistically significant, possibly due in part to the weaker deficits of female SCA1 mice in this assay. This sex-specific discrepancy was restricted to the rotarod assay; no evident sex differences were observed in other behavioral paradigms. In the open field test (OFT), the 715-treated group overall displayed significantly restored general motor activity and enhanced exploration, as evidenced by comprehensive improvements across multiple tracking metrics, including the traveled distance in the center zone (Fig. 5F-H).

Finally, to determine the systemic tolerability of 715 under the same i.p. dosing regimen used for behavioral assessment, we monitored body weight during the first 21 days of dosing prior to behavioral testing and conducted terminal safety evaluations after the full 30-day treatment course. The treated mice exhibited normal body weight trajectories indistinguishable from vehicle controls (Fig. S8A). Moreover, detailed blood biochemistry profiling, along with histopathological (H&E) examinations of the liver and kidneys, revealed no overt signs of toxicity or tissue damage (Fig. S8B-H). Collectively, these results demonstrate that systemic administration of 715 effectively lowers cerebellar mATXN1 without causing overt toxicity under this regimen, leading to significant functional amelioration in a severe preclinical model of SCA1.

**715 reduces mATXN1 and ameliorates behavioral and cerebellar pathological deficits in a newly characterized SCA1 Q60 knock-in (KI) mouse model**

While the *Atxn1*$^{154Q/2Q}$ model effectively captures the core, severe pathology of the disease, expansions of 154 glutamines represent an extreme condition that is rarely observed in clinical settings[10,37]. To better recapitulate the physiological and genetic context of human SCA1 patients, we engineered a humanized *Atxn1*$^{h60Q/2Q}$ knock-in (h60Q KI) mouse model (Fig. 6A). Successful chromosomal integration of the human ATXN1 CDS encoding a 60-glutamine tract was confirmed by Southern blot analysis and standard genotyping (Fig. S9A-C). Preliminary behavioral assessment using the accelerating rotarod test confirmed that h60Q KI mice exhibit baseline motor coordination deficits typical of SCA1 (Fig. S9D). The onset of these motor symptoms occurs significantly later than in the *Atxn1*$^{154Q/2Q}$ model (at approximately 11 months of age), representing a delayed, adult-onset disease trajectory that better mimics the typical clinical presentation of most human SCA1 patients[37,38]. This establishes a physiologically and clinically relevant pathological context for our translational evaluation.

We then verified the target degradation by 715 using this newly established disease model. In primary cortical neurons cultured directly from h60Q mice, 715 treatment elicited a significant, dose-dependent clearance of the endogenous mutant ATXN1 protein (Fig. 6B). To translate this degradative efficacy *in vivo*, daily i.p. administration of 715 for 7 consecutive days significantly reduced the endogenous mATXN1 burden in the cerebellum of h60Q mice, as demonstrated by both Western blot and quantitative MSD assays (Fig. 6C-D).

Given that the h60Q model exhibited characteristic pathological manifestations of SCA1, we conducted a comprehensive battery of behavioral tests to evaluate whether chronic i.p. 715 treatment could provide multimodal functional rescue. In the accelerating rotarod test, unlike the sex-specific discrepancy observed in the severe *Atxn1*$^{154Q/2Q}$ model (Fig. 5E), the h60Q mice did not exhibit significant baseline sex differences. Importantly, chronic 715 treatment effectively prolonged the latencies to fall in both male and female mutant mice, indicating a robust restoration of motor

coordination (Fig. 6E). Consistent with this motor recovery, treadmill-based gait analysis using TreadScan revealed that 715 treatment mitigated ataxia-associated gait abnormalities, notably reducing the horizontal sway variability (standard deviation of the lateral position) during running (Fig. 6F). Beyond these prominent motor impairments, human SCA1 pathogenesis also frequently features concurrent cognitive decline[39-42]. Remarkably, in the Morris Water Maze (MWM) test, compared to wild-type controls, h60Q mice exhibited a significantly reduced percentage of time spent in the target quadrant during the probe trial on day 7, with no significant differences in swimming speed among the groups (Fig. 6G-H), confirming that h60Q mice indeed possess spatial memory impairments. Importantly, this performance was significantly improved in the 715-treated group, demonstrating that 715 effectively mitigates these cognitive deficits.

To determine whether the functional improvements induced by 715 were accompanied by amelioration of cerebellar pathology, we further examined Purkinje cell integrity in h60Q KI mice. Compared with WT controls, h60Q KI mice exhibited a significant reduction in Purkinje cell body linear density in the posterior cerebellum, consistent with the well-established Purkinje cell pathology associated with SCA1[43]. Importantly, chronic 715 treatment significantly improved this Purkinje cell deficit in h60Q KI mice (Fig. 6I). These findings indicate that despite its milder and adult-onset disease phenotype, the h60Q KI model develops measurable cerebellar pathological abnormalities that are responsive to 715 treatment, linking molecular ATXN1 lowering and behavioral improvements with amelioration of cerebellar pathology.

Interestingly, compared to the severe *Atxn1*$^{154Q/2Q}$ mice, the *Atxn1*$^{h60Q/2Q}$ mice presented a milder and more selective phenotypic profile. They did not exhibit significant baseline deficits in general locomotor activity or elevated anxiety-like behaviors[44], as assessed by the open field and elevated plus maze tests, respectively (Fig. S10). This milder phenotypic baseline is also consistent with their unimpaired swimming speed in the MWM test (Fig. 6H). Crucially, chronic 715 administration did not induce any abnormal hyperactivity or anxiety-like side effects in these mice (Fig. S10). Together, these data demonstrate that systemic 715 treatment substantially reduces endogenous mATXN1 and mitigates motor, cognitive, and cerebellar pathological deficits in a physiologically relevant, humanized SCA1 *in vivo* model.

## Oral administration of 715 reduces mATXN1 and improves motor deficits without overt toxicity in *Atxn1*$^{h60Q/2Q}$ mice

While intraperitoneal administration successfully established the in vivo proof-of-concept for the efficacy of 715, an orally bioavailable therapeutic would be highly desirable for the long-term clinical management of chronic neurodegenerative diseases like SCA1. We therefore further examined the oral pharmacokinetic properties of 715. Following a single oral dose of 8 mg/kg in wild-type mice, 715 achieved appreciable systemic and brain exposure, with favorable oral bioavailability and blood-brain barrier penetrance (Fig. S7A & S7C). Together with the i.p. pharmacokinetic profile described above, these findings supported the feasibility of advancing 715 to a chronic oral dosing regimen.

To rigorously evaluate oral efficacy, *Atxn1*$^{h60Q/2Q}$ mice of both sexes were subjected to a chronic oral administration paradigm via daily gavage for 40 consecutive days. Based on single-dose p.o. and i.p. PK profiles, we selected a daily oral gavage dose of 17 mg/kg to approximate the systemic exposure, measured by area under the concentration–time curve (AUC), achieved with the efficacious 5 mg/kg i.p. regimen (Fig. S7B-C). Consistent with the i.p. injection results, long-term oral treatment with 715 resulted in an approximately 30-40% reduction in endogenous cerebellar mATXN1 levels across both sexes, as quantified by MSD and Western blot assays (Fig. 7A-D). Notably, this oral

regimen maintained the allele-selectivity previously observed, leaving the wild-type ATXN1 (2Q) protein levels largely unperturbed.

We next examined whether this biochemically confirmed, oral-route lowering of mATXN1 could translate into functional phenotypic benefits. In the accelerating rotarod test, the h60Q mice orally treated with 715 demonstrated a significant improvement in motor coordination, exhibiting prolonged latencies to fall compared to their vehicle-treated counterparts (Fig. 7E). Furthermore, unlike intraperitoneal administration, orally administered drugs undergo the hepatic first-pass effect via the portal vein, potentially imposing a greater metabolic burden on the liver. We therefore re-evaluated the systemic safety of 715 following the 40-day oral regimen. The treated h60Q mice maintained stable body weights (Fig. S11A), and histopathological (H&E) examinations of the liver and kidneys revealed no discernible differences from the control group (Fig. S11B). Interestingly, plasma biochemical profiling showed a moderate elevation in uric acid levels in the 715-treated group, while no significant abnormalities were observed in the other renal markers (Fig. S11C-H). Given that this isolated uric acid elevation was absent following i.p. administration (Fig. S8E) and was not accompanied by abnormalities in other renal markers (Fig. S11G-H), it did not appear to reflect overt renal toxicity. Uricase-peroxidase-based colorimetric assays are known to be susceptible to chemical interference, raising the possibility that this isolated change reflects assay interference or a route-specific metabolic effect[45,46]. Collectively, these findings support 715 as a promising orally bioavailable lead compound that effectively lowers mATXN1 and improves motor function with favorable overall tolerability in a translationally relevant SCA1 model.

# DISCUSSION

In this study, we identified and characterized 715, an oxindole-derived, brain-penetrant, and orally bioavailable small-molecule degrader that selectively lowers mutant ATXN1 while largely preserving wild-type ATXN1 (Fig. 1B). Mechanistically, 715 promotes BIRC7-dependent clearance of mATXN1 in a ubiquitin–proteasome-dependent manner (Fig. 3 & 4). In two SCA1 knock-in mouse models, 715 reduced endogenous mATXN1 and ameliorated disease-related behavioral deficits (Fig. 5 & 6). Notably, these effects were reproduced with chronic oral dosing in a newly generated humanized *Atxn1*$^{h60Q/2Q}$ model carrying a clinically relevant polyQ expansion and showing a favorable safety profile (Fig. 7 & S11). Together, these findings support 715 as a promising orally active therapeutic candidate for SCA1 and provide a proof-of-concept for allele-selective targeted degradation of pathogenic polyQ-expanded proteins.

A central challenge in developing ATXN1-lowering therapies is how to reduce the toxic mutant protein while avoiding unnecessary depletion of the wild-type allele. Although SCA1 is primarily driven by toxic gain-of-function mechanisms associated with polyQ-expanded mATXN1, loss of normal ATXN1 function can impair spatial learning, motor performance, hippocampal synaptic function, and CIC-associated transcriptional regulation[6-8]. Therefore, nonselective ATXN1-lowering approaches, while potentially effective in reducing mutant protein burden, may carry risks related to chronic wtATXN1 suppression. In this context, the allele-selective activity of 715 is particularly important. Across Daoy cells, primary neurons, SCA1 patient-derived fibroblasts, and mouse cerebellar tissues, 715 preferentially reduced polyQ-expanded ATXN1 (Fig. 1B-G & 5C-D & 6B-C, 7B-D) while exerting minimal effects on non-expanded ATXN1. This selectivity likely reflects preferential recognition of the expanded polyQ tract or its associated conformational features, although the precise structural basis remains to be determined. Such allele selectivity may help widen the therapeutic window for chronic SCA1 treatment.

Another notable feature of 715 is its ability to reduce multiple disease-relevant mATXN1 species. PolyQ-expanded ATXN1 can exist in multiple biochemical and conformational states, including soluble, oligomeric, and aggregate-associated forms, yet the relative contribution of these species to disease progression remains incompletely understood[2,10,18]. Because aggregate-associated polyQ pathology has been documented in affected human brain tissue, strategies that only suppress new protein synthesis may be slow to diminish existing mutant protein burden in symptomatic disease[11]. In contrast, our data indicate that 715 can promote the clearance of both diffuse and aggregate-associated mATXN1 across subcellular compartments (Fig. 2 & S3), a property that may be advantageous for treating established SCA1. In this context, defining which mATXN1 species most closely correlate with neuronal dysfunction, behavioral recovery, and therapeutic response *in vivo* will be important for evaluating this therapeutic potential.

Mechanistically, our findings indicate that 715 promotes mATXN1 clearance mainly through the ubiquitin–proteasome system rather than the autophagy–lysosome pathway (Fig. 3). A ubiquitin-focused CRISPR screen further identified BIRC7 as a key factor in this process, with BIRC7 knockdown significantly impairing 715-induced degradation and poly-ubiquitination of mATXN1 (Fig. 4). Whereas PROTACs, molecular glues, and other UPS-based small-molecule degraders have established that small molecules can induce proteasomal degradation of selected cellular proteins[47-50], 715 extends this principle to the polyQ disease protein ATXN1, achieving allele-selective clearance despite subtle repeat-length differences. More broadly, our findings indicate that 715 engages mATXN1 and that BIRC7 is required for efficient 715-induced mATXN1 clearance (Fig. 4C–H), suggesting that small-molecule degraders can recruit or potentiate target-specific ubiquitination mechanisms beyond commonly used E3 platforms. The involvement of BIRC7 in this mechanism is somewhat unexpected, because it differs from the LC3- or DCAF11-engaging mechanisms previously described for similar oxindole-derived compounds[9,32], suggesting that similar degraders may induce degradation of different targets via distinct mechanisms, possibly influenced by subtle differences in the chemical and/or the target protein structure. It nonetheless remains to be fully established whether 715 forms a stable ternary complex with BIRC7 and whether it alters the conformation or accessibility of the expanded polyQ tract. Although these molecular details are not required to support the current *in vivo* proof-of-concept, resolving them will be important for rational optimization of mutant-selective degraders for SCA1 and other polyQ diseases.

A key determinant of translational relevance is repeat length: although the Atxn1$^{154Q/2Q}$ model provided a valuable severe proof-of-concept (Fig. 5), its expansion is far longer than that of most patients[10,37]. The humanized *Atxn1*$^{h60Q/2Q}$ knock-in model generated here—with a clinically representative repeat length, a human ATXN1 sequence, and a more protracted onset—therefore offers a complementary and more clinically relevant platform, in which 715 conferred benefits across motor, cognitive, and cerebellar pathological phenotypes (Fig. 6E-I & 7E). The cognitive component is notable, as cognitive impairment is increasingly recognized as a clinically relevant feature of SCA1[41,42].

The oral activity of 715 offers a practical advantage for a chronic disease such as SCA1, where long-term treatment is likely required: unlike modalities that depend on repeated invasive delivery (e.g., intrathecal administration), an orally available, central nervous system (CNS)-active small molecule could reduce treatment burden during sustained dosing[51]. Across cellular, neuronal, and *in vivo* assays, 715 was generally well tolerated at efficacious doses (Fig. S1D-G & S8 & S11), the main exception being a moderate, route-specific rise in plasma uric acid after oral (but not i.p.) dosing (Fig. S8E & S11F)—an isolated finding that warrants cautious interpretation and longer-term toxicology with orthogonal methods.

Despite these encouraging findings, several limitations should be acknowledged. First, the 30- to 40-day dosing paradigms used here were sufficient to demonstrate mATXN1 lowering and behavioral improvement, but longer studies will be needed to determine whether 715 can durably modify disease progression, preserve Purkinje cell integrity, and extend functional benefit in this chronic neurodegenerative setting. Second, treatment was initiated at stages when behavioral deficits were detectable but disease was not yet end-stage; therefore, future studies should test whether 715 remains effective after more advanced pathology has developed, a setting that may better approximate treatment initiation in symptomatic patients. However, it is important to acknowledge that there may be a point-of-no-return in this disease with regard to therapies that lower the levels of the mutant protein[52]. In practice, this issue may be manageable in SCA1, an autosomal dominant disease where most individuals have a positive family history[38], since if one had an effective drug then this would provide encouragement for presymptomatic at-risk individuals to be tested for the mutation. Third, although our data indicate that 715 engages mATXN1, enhances its association with BIRC7, and requires BIRC7 for mutant-selective clearance, the precise molecular mechanism underlying this process remains to be fully elucidated. Finally, further preclinical development will require broader safety and pharmacology studies, including long-term toxicology, reproductive toxicity, cardiac safety, evaluation of the potential for drug–drug interactions, and validation in additional species.

Collectively, our study identifies 715 as an orally bioavailable, brain-penetrant, allele-selective degrader of mutant ATXN1. Through a BIRC7-associated ubiquitin–proteasome mechanism, 715 promotes pathogenic mATXN1 clearance while largely preserving wtATXN1. Its efficacy in both a severe SCA1 knock-in model and a humanized SCA1 model carrying a clinically representative 60Q expansion supports the translational potential of this strategy. More broadly, these findings indicate that small molecules can redirect specific cellular ubiquitination machinery to achieve selective degradation of polyQ-expanded disease proteins. Thus, 715 represents a promising therapeutic lead compound for SCA1, and the strategy established here provides a valuable framework for developing allele-selective degraders for other polyQ neurodegenerative diseases.

# Materials and Methods

## Study design

The objective of this study was to identify and characterize an orally available small-molecule degrader that selectively lowers pathogenic polyglutamine-expanded ATXN1 (mATXN1) while largely preserving wild-type ATXN1 (wtATXN1), and to evaluate its mechanism of action and therapeutic potential in preclinical models of spinocerebellar ataxia type 1 (SCA1). The activity and allele selectivity of the lead compound 715 were evaluated across multiple cellular models, including engineered Daoy cells expressing ATXN1 with different polyglutamine lengths, primary mouse cortical neurons, and patient-derived SCA1 fibroblasts. Live-cell imaging, biochemical fractionation, and imaging-based assays were used to assess the effects of 715 on soluble and aggregated mATXN1 and its clearance dynamics. Proteome-wide profiling was performed to assess the selectivity of 715 and its potential effects on the broader cellular proteome.

The mechanism underlying 715-induced mATXN1 lowering was investigated using complementary pharmacological and genetic approaches. The contributions of the ubiquitin-proteasome and autophagy-lysosome systems were examined using pathway-specific inhibitors and genetic perturbations, and changes in mATXN1 ubiquitination were assessed biochemically. A focused CRISPR screen targeting ubiquitin-related genes was performed to identify factors required for 715 activity. Candidate E3 ligases identified by the screen were subsequently evaluated using gene

knockdown, ubiquitination assays, and co-immunoprecipitation to define the molecular machinery involved in 715-induced mATXN1 degradation.

The in vivo pharmacological activity, therapeutic efficacy, and tolerability of 715 were evaluated in two SCA1 knock-in mouse models: the *Atxn1*$^{154Q/2Q}$ model and a newly generated humanized *Atxn1*$^{h60Q/2Q}$ model carrying a clinically relevant polyglutamine expansion. Compound-induced lowering of endogenous mATXN1 was assessed in cerebellar tissues using Western blotting and an electrochemiluminescence-based immunoassay. Disease-relevant motor and cognitive phenotypes were evaluated using the accelerating rotarod, open-field test, treadmill-based gait analysis, and Morris water maze, as appropriate for each experimental cohort. Additional behavioral assessments, body-weight monitoring, plasma biochemical analyses, and histopathological examination of peripheral organs were used to evaluate tolerability and potential adverse effects. The therapeutic effects of both intraperitoneal and oral administration of 715 were investigated.

To ensure a statistical power greater than 0.8, power analyses were performed before experiments using PASS 16 to estimate the minimum sample size required for each assay. Estimates were based on previously published results from comparable experiments and preliminary data from this study. Effect sizes were estimated using Cohen's d, calculated as the difference between two group means divided by the pooled standard deviation. Power analyses indicated that a minimum of three biological replicates was required for measurements of mATXN1 abundance in cellular experiments and a minimum of four animals per group for mouse behavioral experiments. For increased robustness, sample sizes exceeding these minimum requirements were used in some experiments. The numbers of biological replicates or animals are indicated in the corresponding figures or figure legends.

Data were collected at predefined experimental time points, followed by sample collection as appropriate. Data were excluded only when there was clear evidence of technical artifacts or experimental failure, including contamination, transfection or infection failure, inability of an animal to complete a designated behavioral test, or animal injury. Exclusion criteria were established before data analysis, and no data were excluded solely on the basis of statistical outlier status. For in vivo efficacy studies, behavioral performance was designated as the primary endpoint and biomarker levels as secondary endpoints. Samples were selected randomly, and mouse experiments were conducted using randomization and double-blind procedures. Statistical tests were selected according to the experimental design and number of comparison groups and are described in the Statistical analysis section.

## Generation and Identification of Humanized *Atxn1*$^{h60Q/2Q}$ Knock-in Mouse Model

The humanized *Atxn1*$^{h60Q/2Q}$ knock-in mouse model was generated by Biocytogen Pharmaceuticals upon our commission. A homologous recombination vector (targeting vector) was constructed by inserting the human ATXN1 CDS (corresponding to transcript NM_000332.3, containing a 60-glutamine (60Q) tract), followed by a WPRE-bGHpolyA cassette, downstream of the ATG start codon in exon 7 of the mouse *Atxn1* genomic sequence. The Cas9/sgRNA and targeting vector were microinjected into fertilized eggs of C57BL/6J mice. Surviving fertilized eggs were then transplanted into pseudopregnant females for gestation and birth. F0 chimeric mice were identified and further bred to produce F1 offspring to establish a stable humanized *Atxn1*$^{h60Q/2Q}$ knock-in mouse model.

Subsequent genotype identification was performed using mouse tail biopsies. Briefly, tail tissues were incubated in an alkaline lysis solution (100 mM NaOH, 50 μL per sample) at 95 °C for 15 minutes. The lysis was terminated by adding a neutralization solution (1 M Tris-HCl, pH 6.8, 5 μL

per sample) to obtain genomic DNA-containing lysates, which were then amplified via polymerase chain reaction (PCR). The PCR reaction mixture consisted of 2 × Rapid Taq Master Mix (Vazyme P222), forward and reverse primers (10 μM each), template DNA (2 μL), and ddH2O. The PCR cycling conditions were as follows: initial denaturation at 95 °C for 3 min; 5 touchdown cycles (94 °C for 30 s, 65 °C for 30 s with a 1 °C decrease per cycle, and 72 °C for 30 s); 30 cycles of 94 °C for 30 s, 60 °C for 30 s, and 72 °C for 30 s; and a final extension at 72 °C for 5 min. The Genotyping primer sequences are listed in Table S1 of the Supplementary Materials.

Mice were maintained in the university animal facility at 22 °C under a 12-hour light/dark cycle. All animal procedures were conducted in accordance with the ARRIVE (Animal Research: Reporting of In Vivo Experiments) guidelines[53] and complied with all relevant ethical regulations. The animal experimental protocol was approved by the Laboratory Animal Management and Use Committee, Institute of Developmental Biology and Molecular Medicine at Fudan University (IDMIACUC, Animal Protocol ID: IDM2024006b).

**Cell Cultures and Generation of Stable Cell Lines**

Daoy cells were purchased from ATCC and maintained in MEM (Gibco, cat. no. 11095-080) supplemented with 10% (v/v) fetal bovine serum (FBS; Thermo Fisher Scientific, cat. no. 10082-147). HEK293T cells were obtained from ATCC and cultured in DMEM (Cytiva, cat. no. SH30022.01) containing 10% (v/v) FBS. All mammalian cell lines were maintained at 37 °C in a humidified incubator with 5% CO2.

Stable Daoy cell lines expressing ATXN1-2Q, 2Q-GFP, 60Q, 72Q, 72Q (ΔNLS), 72Q-GFP, or 72Q-GFP-p2A-mCherry were established through lentiviral infection. The cDNAs encoding full-length human wild-type (2Q) or mutant ATXN1 with various polyQ lengths, with or without the indicated fluorescent reporter sequences, were subcloned into the multiple cloning site of the pLVX-IRES-puro vector. Lentiviruses were then packaged in HEK293T cells and used to infect parental Daoy cells. Stably transduced cells were selected and maintained in MEM supplemented with 10% FBS and either puromycin (1 μg/mL) or blasticidin S (BSD; 4 μg/mL), as appropriate.

For primary cultures of mouse cortical neurons, tissues were isolated from postnatal day 0 (P0) pups following genotype identification. Dissection was performed in ice-cold Dissection Medium (DM). The tissues were minced and digested in a solution containing 0.25% trypsin and DNase I (0.1 mg/mL) at 37 °C for 20 min. Digestion was terminated by the addition of DMEM supplemented with 10% FBS. After centrifugation, the cell pellet was collected, gently triturated to dissociate the cells, and filtered through a 70-μm cell strainer to obtain a single-cell suspension. The neurons were then seeded onto poly-L-lysine-coated dishes at a density of $7 \times 10^5$ cells/mL for Western blot analysis and $3 \times 10^5$ cells/mL for immunofluorescence. After 3 h, the plating medium was replaced with Neurobasal A medium supplemented with 1 × B-27. Subsequently, half of the medium was refreshed every 3.5 days.

**Patient-derived fibroblast culture**

All procedures involving the collection and use of human tissue samples were approved by the Ethics Committee of Huashan Hospital, Fudan University (FE25253R). Skin biopsy specimens were obtained under local anesthesia from patients with SCA1 carrying ATXN1 alleles of 29Q/57Q or 28Q/49Q, as well as from healthy controls. The tissue specimens were minced into small fragments and cultured in Dulbecco's modified Eagle medium (DMEM) supplemented with 10% fetal bovine serum (FBS; Cat. no. 10099-141, Thermo Fisher Scientific, Waltham, MA, USA) and 0.5× Antibiotic-Antimycotic solution (Cat. no. 15240062, Thermo Fisher Scientific). Cells were maintained at 37 °C in a humidified incubator with 5% $CO_2$.

## Generation of ATG5-KO in Daoy and Daoy-ATXN1-60Q Cells

ATG5-knockout (KO) cell lines were generated in both parental Daoy and Daoy-ATXN1-60Q cells using CRISPR/Cas9 technology. The following single-guide RNAs (sgRNAs) were employed: sgRNA1 (AACTTGTTTCACGCTATATC), sgRNA2 (TGATATAGCGTGAAACAAGT), and sgRNA3 (AAGAGTAAGTTATTTGACGT). Sanger sequencing was performed to characterize the editing outcomes at the targeted ATG5 locus. Single-cell-derived ATG5-KO clones were subsequently established and validated via Western blot analysis.

## cDNA Transfection and Lentiviral Packaging

For HEK293T cells, transfection was performed at the time of seeding (1-3 × $10^5$ cells per well) in 12-well plates using Lipofectamine 2000 (Thermo Fisher Scientific) following the manufacturer's protocol. Each well was transfected with 500 ng of Flag-ATXN1-72Q or Flag-ATXN1-72Q (ΔNLS) plasmid. The culture medium was replaced 6 h after transfection. For compound-treatment experiments, cells were allowed to express the transfected constructs for 24 h before treatment with the indicated compounds for an additional 24 h.

For Daoy cells, lentiviral infection was used exclusively for overexpression to avoid significant cytotoxicity associated with transient transfection. Lentiviruses were packaged in HEK293T cells seeded at a density of 5 × $10^6$ cells per 10 cm dish using JetPrime (Polyplus, cat. no. 101000046). Each dish was transfected with 8 μg of the transfer plasmid, 6 μg of the psPAX2 packaging plasmid, and 2 μg of the pMD2.G envelope plasmid. The culture supernatant was collected 48 h post-transfection and centrifuged at 3000 rpm for 10 min at room temperature to remove cell debris. The resulting viral suspension was filtered through a 0.45 μm PVDF membrane (Millipore, cat. no. SLHPR33RB). This suspension was used directly for Daoy cell infection or concentrated 100-fold for primary neuron infection by ultracentrifugation at 100,000 × g for 2 h, followed by resuspension of the viral pellet in PBS containing 1% BSA.

## siRNA-Mediated Gene Knockdown

With the exception of the siDCAF11 SMARTpool (Horizon Discovery, cat. no. M-019051), all other siRNAs used in this study were synthesized by GenePharma or GeneralBiol. The specific sequences are detailed in Table S2 of the Supplementary Materials. For cultured cell lines, siRNA (50 nM) was transfected using Lipofectamine 2000 (Thermo Fisher Scientific). Knockdown efficiency was evaluated by measuring mRNA abundance via reverse transcription quantitative PCR (RT-qPCR) at 72 h post-transfection. Furthermore, protein levels were assessed via Western blot analysis to verify the silencing efficacy. For combined treatment with chemical compounds, the indicated compounds were added 48 h after siRNA transfection and incubated for an additional 24 h.

## Reverse Transcription Quantitative PCR (RT-qPCR)

Total RNA was extracted from siRNA-transfected or compound-treated cells using the RaPure Total RNA Kit (Magen, cat. no. R4011-03), and genomic DNA was eliminated by treatment with DNase I. First-strand cDNA was synthesized using random primers and the FastQuant RT Kit (Tiangen, cat. no. KR106). Quantitative real-time PCR (qPCR) was then performed using the SYBR Green Realtime PCR Master Mix (Toyobo, cat. no. QPK-201). The qPCR reaction mixture consisted of 2 × SYBR Green Realtime PCR Master Mix, forward and reverse primers (10 pmol/μL each), cDNA template (1 μL), and ddH2O. The thermocycling conditions were as follows: initial denaturation at 95 °C for 3 min, followed by 40 cycles of 95 °C for 10 s, 55 °C for 15 s, and 72 °C for 20 s. A melting curve analysis was subsequently performed by gradually increasing the temperature from 55 °C to 95 °C. The qPCR primer sequences are listed in Table S3 of the Supplementary

Materials. Relative gene expression levels were calculated using the $2^{-\Delta\Delta C_T}$ method and normalized to the reference housekeeping genes (ACTB or GAPDH). Primer specificity and amplification efficiency were verified prior to analysis.

**Chemical synthesis of compound 715**

Compound 715 was synthesized by ChemPartner according to the synthetic route shown in Supplementary Materials. Briefly, intermediate A was prepared from SM1 through acetylation with acetic anhydride. Intermediate B was obtained by TBTU-mediated coupling of intermediate A with SM2, followed by methylation to generate intermediate C using trimethyloxonium tetrafluoroborate. Subsequent nucleophilic substitution of intermediate C with SM3 afforded intermediate D. Final compound 715 was obtained through zinc-mediated reduction of intermediate D in the presence of acetic acid. The final product was purified by silica gel chromatography and validated by LC-MS analysis.

**Compound Treatment in Cells and Animals**

The AN1 compound used in this study was purchased from MCE (cat. no. HY-130258) and quality-controlled by nuclear magnetic resonance (NMR) and liquid chromatography-mass spectrometry (LC-MS). Compound 715 was custom-synthesized by ChemPartner and validated via LC-MS (detailed in “Chemical synthesis of compound 715” above and "715 Compound information and validation" in the Supplementary Materials). Other reagents included DMSO (Sigma-Aldrich, cat. no. D2650), NH4Cl (Sigma-Aldrich, cat. no. A9434), chloroquine (Sigma-Aldrich, cat. no. C6628), bafilomycin A1 (Sigma-Aldrich, cat. no. B1793), MG132 (Selleck, cat. no. S2619), epoxomicin (Selleck, cat. no. S7038), TAK-243 (Selleck, cat. no. S8341), pevonedistat (MLN4924; Selleck, cat. no. S7109), VER-155008 (Selleck, cat. no. S7751), Nutlin-3 (MCE, cat. no. HY-50696), Heclin (MCE, cat. no. HY-110204), and Z-VAD-FMK (Selleck, cat. no. S7023).

For in vitro compound treatment, chemicals were prepared in culture medium at 10× the desired final concentrations and added to the cells at one-tenth of the final culture volume. For primary cultured neurons, compounds were administered 6–7 days post-plating. For protein turnover measurements, cells were pretreated with AN1 for 2 h or 715 for 4 h. Subsequently, cycloheximide (CHX, 10 μg/mL; Selleck, cat. no. S7418) was co-administered with MG132 or a DMSO vehicle control. Cells were then imaged every hour for the following 12 h using an Incucyte live-cell analysis system.

For *in vivo* compound administration via intraperitoneal (i.p.) injection or oral gavage (p.o.), mice were weighed daily to calculate the appropriate administration volume based on body weight. Compound 715 was formulated in a vehicle consisting of 2% DMSO (Sigma-Aldrich, cat. no. D2650), 40% PEG300 (Selleck, cat. no. S6704), 5% Tween-80 (Selleck, cat. no. S6702), and 53% saline at final concentrations of 0.5 mg/mL for i.p. injection and 1.7 mg/mL for oral gavage. The solutions were administered to each mouse via i.p. injection or p.o. gavage at a volume of 0.1 mL per 10 g of body weight. Vehicle-control mice received the same formulation without 715 and were administered identically. For repeated-dose studies, 715 or vehicle was administered once daily for the duration specified for each experimental paradigm until the designated endpoint or tissue collection.

**Protein Extraction from Cells and Tissues**

To sufficiently extract the nuclear-localized ATXN1 protein, cells or cultured neurons were washed twice with ice-cold PBS after removing the culture medium. Lysis buffer consisting of RIPA (Strong) Lysis Buffer (Beyotime, cat. no. P0013B), 1 × BeyoZonase™ (Beyotime, cat. no. D7121),

and 1 × complete protease inhibitor cocktail (Roche, cat. no. 4693159001) was directly added to the dishes. The samples were incubated at 4 °C for 30 min, followed by shaking at 800 rpm for 10 min on an orbital shaker. The lysates were collected in Eppendorf tubes for subsequent Western blot or Meso Scale Discovery (MSD) assays.

For mouse brain tissue extraction, mice were anesthetized and transcardially perfused with 0.9% NaCl. Brains were harvested, and the cerebellum was rapidly dissected on ice and snap-frozen in liquid nitrogen. Tissues were homogenized using a handheld tissue grinder. The homogenate was then mixed with lysis buffer [RIPA (Strong) Lysis Buffer, 4 × BeyoZonase™, 1 × phosphatase inhibitor cocktail (Beyotime, cat. no. P10082), and 1 × complete protease inhibitor cocktail] and incubated at 4 °C with continuous rotation for 1 h. Following five rapid freeze-thaw cycles between liquid nitrogen and a 25 °C water bath, the lysates were centrifuged at 13,200 rpm for 10 min at 4 °C. The resulting supernatant was collected for Western blot or MSD assays.

For all samples, protein concentrations of the lysates were determined using a BCA Protein Assay Kit (Beyotime, cat. no. P0011) to ensure equal protein loading.

**Western Blot Analysis**

For Western blot analysis, protein samples were loaded onto SDS-PAGE gels (GenScript, cat. nos. M00654, M00657). Resolved proteins were then transferred onto nitrocellulose membranes for subsequent blocking and antibody probing. Following a 1 h incubation with secondary antibodies (Abmart, cat. nos. M21001, M21002), the protein signals were visualized using an enhanced chemiluminescence (ECL) kit (Share-Bio, cat. no. SB WB012). The primary antibodies used for Western blotting included: anti-ATXN1 (Boster, cat. no. PB9422), anti-ATXN1 (Abcam, cat. no. ab201037), anti-polyglutamine (1C2) (AntibodySystem, cat. no. RGK26002), anti-DYKDDDDK-Tag (3B9) (Abmart, cat. no. M20008), anti-SQSTM1/p62 (Abcam, cat. no. ab56416), anti-ATG5 (Proteintech, cat. no. 10181-2-AP), anti-ubiquitin (Proteintech, cat. no. 10201-2-AP), anti-LC3B (Thermo Fisher Scientific, cat. no. PA1-16930), anti-TRIM21 (Proteintech, cat. no. 12108-1-AP), anti-TRIM11 (Proteintech, cat. no. 10851-1-AP), anti-VCP (Proteintech, cat. no. 60316-1-Ig), anti-DAXX (Proteintech, cat. no. 20489-1-AP), anti-DCAF11 (ABclonal, cat. no. A15519), anti-BIRC7 (HUABIO, cat. no. HA723483), anti-β-Tubulin (Abcam, cat. no. ab6046), anti-GAPDH-HRP (KANG CHEN, cat. no. KC-5G5), and anti-β-Actin-HRP (KANG CHEN, cat. no. KC-5A08). The specificity of all antibodies was validated either by prior publications or by our internal knockdown and knockout experiments.

**Proteomic profiling and analysis**

Cells were lysed and proteins were extracted as described above. The prepared protein samples were subjected to liquid chromatography–tandem mass spectrometry (LC–MS/MS) analysis performed by the State Key Laboratory of Genetics and Development of Complex Phenotypes, Fudan University. Raw proteomic intensity data were processed using the DEP workflow. Protein abundance values were variance-stabilizing normalized, and missing values were imputed using the MinProb method ($q = 0.01$). Differential protein abundance between 715-treated and DMSO-treated groups was assessed using linear models with empirical Bayes moderation implemented in the limma framework. All statistical tests were two-sided, and P values were adjusted for multiple comparisons using the Benjamini–Hochberg procedure. Proteins with an adjusted P value (false discovery rate, FDR) < 0.05 and an absolute $\log_2$ fold change > 1.25 were considered significantly altered.

Because conventional proteomic analysis cannot directly distinguish WT ATXN1 from polyQ-expanded ATXN1-72Q signals, the mutant-to-WT ATXN1 ratio obtained from Western blot analysis

of the same samples was used to estimate the relative abundance of ATXN1-72Q in the proteomic dataset.

**MSD assay**

For *Atxn1*$^{154Q/2Q}$ mouse brain tissue samples, a 96-well 1-spot SECTOR plate (MSD, L15XA-3) was coated with an anti-polyglutamine (1C2) antibody (AntibodySystem, cat. no. RGK26002) diluted 1:1000 in PBS for 1 h (50 μL/well). For *Atxn1*$^{h60Q/2Q}$ mouse brain tissue samples, the plate was coated with an anti-polyglutamine (3B5H10) antibody (Sigma, cat. no. P1874) diluted 1:500 in PBS. Subsequently, the plates were washed three times with TBS-Tween 20 (0.1%) wash buffer and blocked with a 3% BSA-TBST blocking solution on a shaker for 2 h. After washing three times with TBST buffer, the tissue lysates were added. Specifically, the tissue lysates were adjusted to a protein concentration of 2 μg/μL with lysis buffer, further diluted to 1 μg/μL with 1% BSA-TBST, and then added to the plate (30 μL/well). The plates were incubated on a shaker for 90 min. Following three washes with TBST buffer, an anti-ATXN1 antibody (Boster, cat. no. PB9422) diluted 1:100 in 1% BSA-TBST was added (50 μL/well) and incubated on a shaker for 1 h. After three additional washes, a Goat Anti-Rabbit IgG antibody (Abmart, cat. no. M21002) labeled with MSD GOLD SULFO-TAG NHS-Ester (MSD, cat. no. R91AO) and diluted 1:500 in 1% BSA-TBST was added (50 μL/well) and incubated on a shaker for 1 h, followed by three washes. Subsequently, MSD-Read buffer (2 ×) (MSD, R92TC) was added (120 μL/well), and the plates were immediately read using a MESO QUICKPLEX SQ 120MM Reader. All incubation steps were performed at room temperature with shaking at 600 rpm unless otherwise indicated. All samples underwent BCA protein concentration determination, and serially diluted tissue lysates were used to assess the linearity and dynamic range of the assay.

**Immunoprecipitation and ubiquitination assay**

To assess ATXN1 ubiquitination, ATXN1 was immunoprecipitated and ubiquitin signals were detected by Western blot analysis. Daoy ATXN1-60Q cells or control Daoy ATXN1-2Q cells were seeded in 10-cm dishes. Before harvesting, cells were treated with 0.1% DMSO or 300 nM 715 in the presence of 1 μM MG132 and 25 μM Z-VAD-FMK for 4 h. Cells were subsequently collected by TrypLE digestion (Thermo Fisher Scientific, cat. no. 12605028) and washed once with PBS. Cells were lysed on ice for 30 min in lysis buffer containing RIPA (Strong) Lysis Buffer (Beyotime, cat. no. P0013B), 1× BeyoZonase™ (Beyotime, cat. no. D7121), 1 × complete protease inhibitor cocktail (Roche, cat. no. 4693159001), and 10 mM N-ethylmaleimide (MCE, cat. no. HY-D0843). Protein concentrations of the lysates were determined using a BCA Protein Assay Kit (Beyotime, cat. no. P0011). Five percent of the lysate was reserved as the whole-cell lysate (Input) control. The remaining lysates were incubated with anti-Flag antibody (3B9) (Abmart, cat. no. M20008) at a 1:100 dilution overnight at 4 °C with gentle rotation. After antibody incubation, 20 μL of pre-blocked Protein A/G Magnetic Beads (Pierce, cat. no. 88802) were added, and the mixture was incubated at room temperature for 90 min with rotation. The bead–protein complexes were subsequently washed three times with RIPA lysis buffer. Immunoprecipitated proteins were eluted by boiling in 1 × LDS loading buffer at 95 °C for 10 min and analyzed by Western blotting as described above.

**Co-immunoprecipitation assay**

To assess the effect of 715 treatment on the interaction between ATXN1 and BIRC7, ATXN1–BIRC7 co-immunoprecipitation assays were performed followed by Western blot analysis of BIRC7. Daoy cells co-expressing ATXN1-GFP (2Q or 72Q) and BIRC7 were seeded in 10-cm dishes. Prior to cell collection, cells were treated with 300 nM 715 or 0.1% DMSO in combination with 1 μM MG132

and 25 μM Z-VAD-FMK for 4 h. Cells were subsequently lysed on ice for 30 min in lysis buffer containing 0.5% NP-40 lysis buffer (Beyotime, cat. no. P0013F; diluted 1:1 with PBS), 1 × BeyoZonase™ (Beyotime, cat. no. D7121), 1 × complete protease inhibitor cocktail (Roche, cat. no. 4693159001), and 1 × PhosSTOP phosphatase inhibitor cocktail (Roche, cat. no. 4906845001). Protein concentrations of the lysates were determined using a BCA Protein Assay Kit (Beyotime, cat. no. P0011). Five percent of the lysate was reserved as the whole-cell lysate (Input) control. The remaining lysates were incubated with 20 μL anti-GFP Nanobody Magarose Beads (AlphaLifeBio, cat. no. KTSM1334) at 4 °C overnight with gentle rotation. The bead–protein complexes were washed three times with 0.5% NP-40 lysis buffer. Immunoprecipitated proteins were eluted by boiling in 1 × LDS loading buffer at 95 °C for 10 min and analyzed by Western blotting as described above.

**CellTiter-Glo® Luminescent Cell Viability Assay**

The CellTiter-Glo® Luminescent Cell Viability Assay (CTG) is a homogeneous method used to determine the number of viable cells in culture based on the quantitation of ATP, an indicator of metabolically active cells. To evaluate drug cytotoxicity, cell viability was measured using the CTG kit (Promega, cat. no. G7570) following the manufacturer's instructions. Briefly, cells seeded in 96-well plates were removed from the incubator. With 30 μL of culture medium remaining in each well, the plates were left at room temperature (RT) for 5 min to equilibrate. The CellTiter-Glo reagent was concurrently equilibrated to RT. Subsequently, the reagent was added to the wells at a 1:1 ratio (v/v). The plates were then mixed on a shaker for 2 min, and the luminescence signals were measured using EnVision 2105 microplate reader.

**Cellular Thermal Shift Assay (CETSA)**

To evaluate whether 715 alters the thermal stability of ATXN1, a cellular thermal shift assay (CETSA) was performed using Daoy ATXN1-72Q cell lysates. Harvested Daoy ATXN1-72Q cell pellets were resuspended in PBS supplemented with 1 × BeyoZonase™ (Beyotime, cat. no. D7121) and 1 × complete protease inhibitor cocktail (Roche, cat. no. 4693159001). Cells were lysed by five rapid freeze-thaw cycles between liquid nitrogen and a 25 °C water bath. The lysates were then centrifuged at 13,200 rpm for 20 min at room temperature, and the supernatant was collected. The cleared lysates were divided into aliquots and incubated with DMSO, 50 μM 715, or PQBP1 protein (as a positive control) at room temperature for 90 min. Following incubation, the samples were divided into equal aliquots in PCR tubes and heated at a series of temperatures ranging from 40 °C to 70 °C for 3 min using a thermal cycler, followed by cooling at room temperature. The samples were subsequently centrifuged at 20,000 × g for 20 min at 4 °C to separate the soluble fractions from the precipitated proteins. The soluble supernatants were collected, mixed with LDS loading buffer, and heated at 75 °C for 10 min. The abundance of soluble ATXN1-72Q and endogenous WT ATXN1 proteins at each temperature point was evaluated by Western blot analysis. Band intensities were quantified using ImageJ software, and normalized intensities were plotted against temperature using GraphPad Prism 10.

**Immunofluorescence Assay**

For the immunofluorescent detection of exogenously overexpressed Flag-ATXN1, the culture medium was removed from the dish, and the cells were washed three times with PBS buffer. The cells were then fixed with 4% paraformaldehyde and permeabilized/blocked with 4% BSA containing 0.3% Triton X-100 for 1 h at room temperature. Subsequently, the cells were incubated with a primary antibody against the DYKDDDDK-Tag (3B9) (Abmart, cat. no. M20008) overnight at 4 °C. Following three washes with PBS, the coverslips were incubated with fluorescently labeled secondary

antibodies (Abcam, cat. no. ab150077) for 2 h at room temperature. Unbound antibodies were removed by washing with PBS, and cell nuclei were counterstained with DAPI (Beyotime, cat. no. C1002). Confocal images were acquired using a Zeiss LSM 880 microscope equipped with an Airyscan module or an Olympus SpinSR spinning disk confocal microscope. The acquired images were analyzed in a blinded manner using ImageJ software.

**Fluorescence Recovery After Photobleaching (FRAP) Assay**

FRAP assays were performed using a Leica Stellaris 5 WLL confocal microscope equipped with a 63 ×/1.4 NA oil-immersion objective. Daoy ATXN1-72Q-GFP and Daoy ATXN1-2Q-GFP cells were cultured in glass-bottom dishes (Cellvia, cat. no. D35-20-1-N) and maintained in a live-cell environmental chamber at 37 °C and 5% $CO_2$ during the imaging process. A region of interest (ROI) was defined within the ATXN1-GFP puncta. After acquiring 3 pre-bleach frames to establish the baseline fluorescence, the ROI was photobleached using a 488 nm laser at 100% laser power for 15 iterations. Fluorescence recovery was recorded every 5 s for 30 frames at a low laser intensity. Fluorescence intensities of the bleached ROI, an unbleached reference ROI (to correct for continuous photobleaching), and a background region were quantified using LAS X software, and the recovery curves were subsequently normalized to the mean pre-bleach fluorescence.

**CRISPR-Cas9 Screen**

A CRISPR-Cas9 screen targeting human ubiquitination-related genes was performed using the Bonifacino Lab Human Ubiquitination-related Proteins CRISPR KO Library (Ubigene Biosciences, cat. no. LIBR-H017-LV1000). The lentiviral library was used to transduce Daoy ATXN1-72Q-GFP-p2A-mCherry cells at a multiplicity of infection (MOI) of 0.4, achieving a transduction efficiency of approximately 30%, to ensure a single sgRNA integration per cell. At 24 h post-transduction, cells were selected with puromycin (1 μg/mL) for 2 days. The surviving cells were pooled and expanded. A fraction of the cells was collected to serve as the unsorted control group, while the remaining cells were divided into a 0.1% DMSO vehicle group and a 300 nM 715 treatment group. Following a 24-h treatment, cells resistant to 715-induced ATXN1-72Q-GFP reduction, along with the corresponding cell population in the DMSO group, were isolated via fluorescence-activated cell sorting (FACS). A minimum library coverage of 500× per sgRNA was maintained throughout the screen. The sorted cells and the unsorted control samples were subsequently sent to Ubigene Biosciences for genomic DNA extraction. The sgRNA-encoding regions were amplified via PCR and subjected to next-generation sequencing (NGS) on an Illumina platform. Sequence data were demultiplexed and analyzed using DrugZ algorithms to identify significantly enriched or depleted sgRNAs and rank candidate genes.

**Pharmacokinetic experiment**

C57BL/6J mice used for the pharmacokinetic experiment were provided by the SIM-Servier joint laboratory of the Shanghai Institute of Materia Medica, Chinese Academy of Sciences. Following a single intraperitoneal (i.p.) dose of 5 mg/kg or oral gavage (p.o.) dose of 8 mg/kg 715, mice were anesthetized at the indicated time points (1, 2, 4, 8, and 16 h). Cardiac blood and brain tissues were collected at each time point. The liquid chromatography-mass spectrometry (LC-MS) analyses were also performed by the SIM-Servier joint laboratory.

**Cerebellar immunofluorescence staining**

To evaluate cerebellar pathological phenotypes, immunofluorescence staining was performed on mouse cerebellar sections. Mice were deeply anesthetized with 1.25% tribromoethanol (Aibei, cat. no.

M2920) and subsequently perfused transcardially. Cerebellar hemispheres were collected and fixed in 4% paraformaldehyde (PFA; Solarbio, cat. no. P1110) at 4 °C for 24 h. Fixed tissues were sequentially dehydrated in 20% and 30% sucrose solutions for 24 h each. After dehydration, excess moisture was removed from cerebellar tissues, followed by embedding in OCT compound (SAKURA, cat. no. 4583). Cerebellar tissues were sectioned at a thickness of 30 μm using a cryostat. Free-floating sections were washed with PBS to remove OCT and subsequently incubated in permeabilization/blocking buffer containing 1% BSA, 0.3% Triton X-100, and 5% goat serum for 2 h at room temperature. The same buffer was used for antibody dilution. Sections were incubated with anti-Calbindin-D28k primary antibody (1:500 dilution; Proteintech, cat. no. 66394-1-Ig) at 4 °C for 48 h, followed by incubation with Alexa Fluor 488-conjugated goat anti-mouse IgG (H+L) secondary antibody (1:500 dilution; Beyotime, cat. no. A0428) at room temperature for 2 h. Nuclei were counterstained with DAPI (Beyotime, cat. no. C1002) diluted 1:1000 in PBS for 10 min. All washing steps were performed with PBS at room temperature for 10 min × 3 times.

Images were acquired using an Evident Olympus VS200 slide scanner with a 20 × objective. Image analysis and quantification were performed using QuPath and ImageJ software.

**Open-field tests**

All behavioral tests were conducted during the light cycle and performed in a blinded manner. Before testing, the mice were allowed to adapt to the testing room for at least 0.5 h. The open-field apparatus consisted of a square plastic arena (50 cm × 50 cm × 50 cm), and each mouse was placed in the center of the box. The locomotion of the mice was captured by a camera mounted above the arena for 10 min. A video tracking system (TopScan Version 3.0) was used to record and analyze the movement trajectories.

**Rotarod**

To assess motor learning, coordination, and balance, the mice were tested on a Rotarod apparatus (MED Associates) with a 3-cm diameter rod. To acclimate the mice to the apparatus, each mouse was trained for 3 consecutive days, which consisted of three 5-min acclimatization trials per day at a constant speed of 4 rpm. During the testing phase, the $Atxn1^{154Q/2Q}$ mice and their corresponding controls were placed on the rotarod with the speed uniformly accelerating from 4 to 40 rpm over 540 s. For the $Atxn1^{h60Q/2Q}$ mice and their controls, the speed was set to uniformly accelerate from 0 to 40 rpm over 240 s. The latency to fall off the rotarod during this period was recorded. Following a modified protocol, each mouse underwent three trials per day for a total of 5 to 7 days, and the mean latency to fall was calculated for statistical analysis.

**Mouse Gait Analysis**

Quantitative assessment of gait behavior was performed using the TreadScan system. Video acquisition was conducted with the BCamCap software provided by Clever Systems. Each mouse was placed in a treadmill chamber with a transparent floor, followed by the initiation of the treadmill. Once the mouse was running stably, a 20-second video of its gait behavior was recorded. The treadmill speed was set to 12 cm/s. A single trial was recorded for each mouse, and the acquired data were subsequently analyzed to extract various gait parameters.

**Morris Water Maze Test**

To evaluate the spatial learning and memory abilities of the mice, the Morris Water Maze (MWM) test was conducted. The experiment was performed in a cylindrical stainless steel pool (1.2 m in diameter) with the water temperature maintained at 22 ± 1 °C. The entire pool was shielded

behind a barrier to prevent the mice from seeing the experimenters, and a dim-light environment was maintained. Food-grade titanium dioxide was added to the water to make it opaque. The pool was conceptually divided into four equal quadrants, and a transparent circular platform (10 cm in diameter) was placed in the center of the target quadrant. The movement trajectories of the mice were recorded and analyzed using the TopScan Version 3.0 video tracking system. To prevent hypothermia, the mice were placed under a warming lamp to dry after each trial. The experiment lasted for a total of 7 days, with the specific procedures as follows:

Visible Platform Training (Days 1-2): The platform was positioned 0.5 cm above the water surface. Mice were released into the water facing the pool wall from predefined starting points located at the midpoint of the pool wall in the non-target quadrants. The time taken to locate the platform within 60 s was recorded. If a mouse failed to find the platform within 60 s, it was manually guided to the platform and allowed to stay there for 20 s to adapt. Each mouse underwent 3 training trials per day.

Hidden Platform Training (Days 3-5): The platform's position remained unchanged, but water was added until the surface was 0.5 cm above the platform. The starting points and the criteria for a single test remained consistent with those of the visible platform training phase. Each mouse underwent 3 training trials per day.

Hidden Platform Test (Day 6): The platform's position and depth remained unchanged. The starting point was fixed at the peripheral center of the opposite quadrant. The time taken by the mice to find the platform within 90 s was recorded. If a mouse did not find the platform within 90 s, it was guided to the platform to rest for 20 s. Each mouse was tested 3 times.

Probe Trial (Day 7): The platform was removed. Mice were released into the water from the peripheral center of the opposite quadrant and allowed to explore the pool freely for 90 s. The swimming speed, the time spent in the target quadrant, and the number of crossings over the previous platform area were recorded to evaluate the spatial memory abilities of the mice. Each mouse was tested 3 times.

**Elevated Plus Maze Test**

To evaluate anxiety-like behaviors in the mice, the elevated plus maze (EPM) test was conducted. The maze was cross-shaped, consisting of two opposite open arms (30 cm × 5 cm), two opposite closed arms (30 cm × 5 cm × 15 cm), and a central platform (5 cm × 5 cm) connecting the four arms. The entire apparatus was mounted on a stand elevated 50 cm above the floor.

The experiment was performed in a quiet, dimly lit, and soundproof room. Prior to testing, the mice, along with their home cages, were moved into the testing room to habituate to the environment for at least 30 min. At the start of the test, each mouse was placed on the central platform facing one of the open arms and allowed to explore the maze freely for 5 min. The movement trajectories of the mice were recorded and analyzed using a camera mounted directly above the maze and the TopScan Version 3.0 video tracking system.

To eliminate the interference of olfactory cues left by the previous animal, the floor and inner walls of the maze were thoroughly wiped with a 75% ethanol solution after each trial. Consecutive tests were conducted only after the ethanol had completely evaporated.

**Animal biosafety evaluation of 715**

For the biosafety evaluation, the mice were anesthetized and sampled after the completion of intraperitoneal or oral gavage. Orbital blood samples were collected in EDTA anticoagulant tubes, mixed well, and then centrifuged at 3,000 rpm for 10 min to generate plasma. The mice were then perfused with 0.9% NaCl to remove residual blood. The liver and kidney samples were dissected and

fixed in 4% paraformaldehyde. The plasma samples were subjected to blood chemistry analysis, including liver and kidney-related biomarkers, using a Sysmex BX-3010 automated chemistry analyzer by Shanghai Model Organisms Center, Inc.

The liver and kidney tissues were processed for histological hematoxylin and eosin (H&E) staining by Shanghai Ribiology Technology Co., Ltd. Briefly, the fresh tissues were fixed in 4% paraformaldehyde for more than 24 h and then dehydrated using an alcohol gradient. The tissues were embedded in paraffin wax and sectioned. The paraffin sections were deparaffinized and rehydrated. The cell nuclei and cytoplasm were stained with hematoxylin and eosin, respectively. Finally, the sections were dehydrated, mounted, and scanned for analysis using an Evident Olympus VS200 slide scanner.

### Statistical analysis

Quantitative data are presented as the mean ± standard error of the mean (SEM), with n representing independent biological replicates for cellular experiments and individual animals for in vivo experiments unless otherwise indicated. Comparisons between two groups were performed using two-tailed unpaired Student's t tests. Comparisons involving more than two groups were performed using one-way ANOVA followed by the appropriate multiple-comparisons test, as specified in the corresponding figure legends. Time-course or longitudinal datasets were analyzed using two-way ANOVA, with the corresponding multiple-comparisons tests specified in the figure legends. Normality was assessed using the Shapiro–Wilk test, and homogeneity of variance was evaluated before parametric testing. Statistical analyses were performed using GraphPad Prism 10. All tests were two-tailed, and $P < 0.05$ was considered statistically significant. All mouse behavioral experiments were conducted in a blinded manner. Data were excluded only in cases of clear experimental artifacts or technical failures, including contamination, unsuccessful transfection or infection, or animal injury.

## List of Supplementary Material

Fig. S1 to S11

Table S1 to S3

715 Compound information and validation

715 Compound synthetic route

References (53)

## References


1 Zoghbi, H. Y. & Orr, H. T. Pathogenic mechanisms of a polyglutamine-mediated neurodegenerative disease, spinocerebellar ataxia type 1. *J Biol Chem* **284**, 7425–7429 (2009). https://doi.org/10.1074/jbc.R800041200

2 Klement, I. A. *et al.* Ataxin-1 nuclear localization and aggregation: role in polyglutamine-induced disease in SCA1 transgenic mice. *Cell* **95**, 41–53 (1998). https://doi.org/10.1016/s0092-8674(00)81781-x

3 Ashizawa, T., Oz, G. & Paulson, H. L. Spinocerebellar ataxias: prospects and challenges for therapy development. *Nat Rev Neurol* **14**, 590–605 (2018). https://doi.org/10.1038/s41582-018-0051-6

4 Ghanekar, S. D., Kuo, S. H., Staffetti, J. S. & Zesiewicz, T. A. Current and emerging treatment modalities for spinocerebellar ataxias. *Expert Rev Neurother* **22**, 101–114 (2022). https://doi.org/10.1080/14737175.2022.2029703

5 Friedrich, J. *et al.* Antisense oligonucleotide-mediated ataxin-1 reduction prolongs survival in SCA1 mice and reveals disease-associated transcriptome profiles. *JCI Insight* **3**, e123193 (2018). https://doi.org/10.1172/jci.insight.123193

6 Matilla, A. *et al.* Mice lacking ataxin-1 display learning deficits and decreased hippocampal paired-pulse facilitation. *J Neurosci* **18**, 5508–5516 (1998). https://doi.org/10.1523/jneurosci.18-14-05508.1998

7 Crespo-Barreto, J., Fryer, J. D., Shaw, C. A., Orr, H. T. & Zoghbi, H. Y. Partial loss of ataxin-1 function contributes to transcriptional dysregulation in spinocerebellar ataxia type 1 pathogenesis. *PLoS Genet* **6**, e1001021 (2010). https://doi.org/10.1371/journal.pgen.1001021

8 Lam, Y. C. *et al.* ATAXIN-1 interacts with the repressor Capicua in its native complex to cause SCA1 neuropathology. *Cell* **127**, 1335–1347 (2006). https://doi.org/10.1016/j.cell.2006.11.038

9 Li, Z. *et al.* Allele-selective lowering of mutant HTT protein by HTT-LC3 linker compounds. *Nature* **575**, 203–209 (2019). https://doi.org/10.1038/s41586-019-1722-1

10 Watase, K. *et al.* A long CAG repeat in the mouse Sca1 locus replicates SCA1 features and reveals the impact of protein solubility on selective neurodegeneration. *Neuron* **34**, 905–919 (2002). https://doi.org/10.1016/s0896-6273(02)00733-x

11 Yamada, M., Sato, T., Tsuji, S. & Takahashi, H. CAG repeat disorder models and human neuropathology: similarities and differences. *Acta Neuropathol* **115**, 71–86 (2008). https://doi.org/10.1007/s00401-007-0287-5

12 Jacobsen, P. F., Jenkyn, D. J. & Papadimitriou, J. M. Establishment of a human medulloblastoma cell line and its heterotransplantation into nude mice. *J Neuropathol Exp Neurol* **44**, 472–485 (1985). https://doi.org/10.1097/00005072-198509000-00003

13 Ford-Roshon, D. *et al.* Spinocerebellar Ataxia Type 1 (SCA1) Cell Models Display Widespread Mitochondrial and Extra-Nuclear Alterations. *J Mol Neurosci* **75**, 131 (2025). https://doi.org/10.1007/s12031-025-02425-5

14 Xu, H. *et al.* Proteomic Profiling of Paclitaxel Treated Cells Identifies a Novel Mechanism of Drug Resistance Mediated by PDCD4. *J Proteome Res* **14**, 2480–2491 (2015). https://doi.org/10.1021/acs.jproteome.5b00004

15 Devos, H., Zoidakis, J., Roubelakis, M. G., Latosinska, A. & Vlahou, A. Reviewing the Regulators of COL1A1. *Int J Mol Sci* **24**, 10004 (2023). https://doi.org/10.3390/ijms241210004

16 Herrera, J., Henke, C. A. & Bitterman, P. B. Extracellular matrix as a driver of progressive fibrosis. *J Clin Invest* **128**, 45–53 (2018). https://doi.org/10.1172/jci93557

17 Hyman, A. A., Weber, C. A. & Jülicher, F. Liquid-liquid phase separation in biology. *Annu Rev Cell Dev Biol* **30**, 39–58 (2014). https://doi.org/10.1146/annurev-cellbio-100913-013325

18 Kim, S., Nollen, E. A., Kitagawa, K., Bindokas, V. P. & Morimoto, R. I. Polyglutamine protein aggregates are dynamic. *Nat Cell Biol* **4**, 826–831 (2002). https://doi.org/10.1038/ncb863

19 Mizushima, N. *et al.* Dissection of autophagosome formation using Apg5-deficient mouse embryonic stem cells. *J Cell Biol* **152**, 657–668 (2001). https://doi.org/10.1083/jcb.152.4.657

20 Kabeya, Y. *et al.* LC3, a mammalian homologue of yeast Apg8p, is localized in autophagosome membranes after processing. *Embo j* **19**, 5720–5728 (2000). https://doi.org/10.1093/emboj/19.21.5720

21 Hyer, M. L. *et al.* A small-molecule inhibitor of the ubiquitin activating enzyme for cancer treatment. *Nat Med* **24**, 186–193 (2018). https://doi.org/10.1038/nm.4474

22 Zhu, G. *et al.* TRIM11 Prevents and Reverses Protein Aggregation and Rescues a Mouse Model of Parkinson's Disease. *Cell Rep* **33**, 108418 (2020). https://doi.org/10.1016/j.celrep.2020.108418
23 Miller, L. V. C. *et al.* Co-opting templated aggregation to degrade pathogenic tau assemblies and improve motor function. *Cell* **187**, 5967–5980 e5917 (2024). https://doi.org/10.1016/j.cell.2024.08.024
24 Kang, A. R., An, H. T., Ko, J. & Kang, S. Ataxin-1 regulates epithelial-mesenchymal transition of cervical cancer cells. *Oncotarget* **8**, 18248–18259 (2017). https://doi.org/10.18632/oncotarget.15319
25 Al-Ramahi, I. *et al.* CHIP protects from the neurotoxicity of expanded and wild-type ataxin-1 and promotes their ubiquitination and degradation. *J Biol Chem* **281**, 26714–26724 (2006). https://doi.org/10.1074/jbc.M601603200
26 Choi, J. Y. *et al.* Co-chaperone CHIP promotes aggregation of ataxin-1. *Mol Cell Neurosci* **34**, 69–79 (2007). https://doi.org/10.1016/j.mcn.2006.10.002
27 Twomey, E. C. *et al.* Substrate processing by the Cdc48 ATPase complex is initiated by ubiquitin unfolding. *Science* **365**, eaax1033 (2019). https://doi.org/10.1126/science.aax1033
28 Darwich, N. F. *et al.* Autosomal dominant VCP hypomorph mutation impairs disaggregation of PHF-tau. *Science* **370**, eaay8826 (2020). https://doi.org/10.1126/science.aay8826
29 Guo, L. *et al.* A cellular system that degrades misfolded proteins and protects against neurodegeneration. *Mol Cell* **55**, 15–30 (2014). https://doi.org/10.1016/j.molcel.2014.04.030
30 Ishov, A. M. *et al.* PML is critical for ND10 formation and recruits the PML-interacting protein daxx to this nuclear structure when modified by SUMO-1. *J Cell Biol* **147**, 221–234 (1999). https://doi.org/10.1083/jcb.147.2.221
31 Zhang, X. *et al.* DCAF11 Supports Targeted Protein Degradation by Electrophilic Proteolysis-Targeting Chimeras. *J Am Chem Soc* **143**, 5141–5149 (2021). https://doi.org/10.1021/jacs.1c00990
32 Xue, G. *et al.* Discovery of a Drug-like, Natural Product-Inspired DCAF11 Ligand Chemotype. *Nat Commun* **14**, 7908 (2023). https://doi.org/10.1038/s41467-023-43657-6
33 Ma, L. *et al.* Livin promotes Smac/DIABLO degradation by ubiquitin-proteasome pathway. *Cell Death Differ* **13**, 2079–2088 (2006). https://doi.org/10.1038/sj.cdd.4401959
34 Okazawa, H. *et al.* Interaction between mutant ataxin-1 and PQBP-1 affects transcription and cell death. *Neuron* **34**, 701–713 (2002). https://doi.org/10.1016/s0896-6273(02)00697-9
35 Jiang, S. *et al.* Generic Diagramming Platform (GDP): a comprehensive database of high-quality biomedical graphics. *Nucleic Acids Res* **53**, D1670–d1676 (2025). https://doi.org/10.1093/nar/gkae973
36 Selimovic, A. *et al.* Sex Differences in a Novel Mouse Model of Spinocerebellar Ataxia Type 1 (SCA1). *Int J Mol Sci* **26**, 2623 (2025). https://doi.org/10.3390/ijms26062623
37 Tezenas du Montcel, S. *et al.* Prediction of the age at onset in spinocerebellar ataxia type 1, 2, 3 and 6. *J Med Genet* **51**, 479–486 (2014). https://doi.org/10.1136/jmedgenet-2013-102200
38 Opal, P. & Ashizawa, T. in *GeneReviews(®)* (eds M. P. Adam *et al.*) (University of Washington, Seattle, Seattle (WA), 2023).
39 Malek, N., Makawita, C., Al-Sami, Y., Aslanyan, A. & de Silva, R. A Systematic Review of the Spectrum and Prevalence of Non-Motor Symptoms in Adults with Hereditary Cerebellar Ataxias. *Mov Disord Clin Pract* **9**, 1027–1039 (2022). https://doi.org/10.1002/mdc3.13532
40 Petit, E. *et al.* Prevalence, Severity, and Progression of Cerebellar Cognitive-Affective Syndrome in Patients With Spinocerebellar Ataxias. *Neurology* **105**, e213980 (2025). https://doi.org/10.1212/wnl.0000000000213980

41 Olmos, V., Gogia, N., Luttik, K., Haidery, F. & Lim, J. The extra-cerebellar effects of spinocerebellar ataxia type 1 (SCA1): looking beyond the cerebellum. *Cell Mol Life Sci* **79**, 404 (2022). https://doi.org/10.1007/s00018-022-04419-7
42 Bürk, K. *et al.* Cognitive deficits in spinocerebellar ataxia type 1, 2, and 3. *J Neurol* **250**, 207–211 (2003). https://doi.org/10.1007/s00415-003-0976-5
43 Serra, H. G. *et al.* RORalpha-mediated Purkinje cell development determines disease severity in adult SCA1 mice. *Cell* **127**, 697–708 (2006). https://doi.org/10.1016/j.cell.2006.09.036
44 Tichanek, F. *et al.* Hippocampal mitochondrial dysfunction and psychiatric-relevant behavioral deficits in spinocerebellar ataxia 1 mouse model. *Sci Rep* **10**, 5418 (2020). https://doi.org/10.1038/s41598-020-62308-0
45 Lamb, E. J. & Price, C. P. Use of azure-D2 for the measurement of uric acid in serum. *Eur J Clin Chem Clin Biochem* **33**, 595–601 (1995).
46 Kayamori, Y., Katayama, Y. & Urata, T. Nonenzymatic elimination of ascorbic acid in clinical samples. *Clin Biochem* **33**, 25–29 (2000). https://doi.org/10.1016/s0009-9120(99)00082-x
47 Bekes, M., Langley, D. R. & Crews, C. M. PROTAC targeted protein degraders: the past is prologue. *Nat Rev Drug Discov* **21**, 181–200 (2022). https://doi.org/10.1038/s41573-021-00371-6
48 Winter, G. E. *et al.* DRUG DEVELOPMENT. Phthalimide conjugation as a strategy for in vivo target protein degradation. *Science* **348**, 1376–1381 (2015). https://doi.org/10.1126/science.aab1433
49 Kronke, J. *et al.* Lenalidomide causes selective degradation of IKZF1 and IKZF3 in multiple myeloma cells. *Science* **343**, 301–305 (2014). https://doi.org/10.1126/science.1244851
50 Neklesa, T. K. *et al.* Small-molecule hydrophobic tagging-induced degradation of HaloTag fusion proteins. *Nat Chem Biol* **7**, 538–543 (2011). https://doi.org/10.1038/nchembio.597
51 Bennett, C. F., Krainer, A. R. & Cleveland, D. W. Antisense Oligonucleotide Therapies for Neurodegenerative Diseases. *Annu Rev Neurosci* **42**, 385–406 (2019). https://doi.org/10.1146/annurev-neuro-070918-050501
52 Zu, T. *et al.* Recovery from polyglutamine-induced neurodegeneration in conditional SCA1 transgenic mice. *J Neurosci* **24**, 8853–8861 (2004). https://doi.org/10.1523/jneurosci.2978-04.2004
53 Percie du Sert, N. *et al.* The ARRIVE guidelines 2.0: Updated guidelines for reporting animal research. *PLoS Biol* **18**, e3000410 (2020). https://doi.org/10.1371/journal.pbio.3000410

**Acknowledgement**

We would like to thank Drs. Huaixiang Hao and Nan Ji at PAQ Therapeutics for their assistance with the generation and provision of the humanized *Atxn1*$^{h60Q/2Q}$ knock-in mouse model.

**Funding**

We are grateful for the following funding resources:
Brain Science and Brain-like Intelligence Technology-National Science and Technology Major Project (grant no. 2025ZD0214800) (to BL).
National Natural Science Foundation of China (grant nos. 82525103, 82450901, and 82394422) (to BL).
The New Cornerstone Science Foundation (grant no. NCI202242) (to BL).
UK Dementia Research Institute through UK DRI Ltd (principally funded by the Medical Research Council) (to DCR).

**Author contributions**

Conceptualization: BL
Methodology: BL, HT, XJ

Investigation: HT, XJ, JC
Formal analysis: HT, XJ, JC, YL
Visualization: HT, YL
Resources: JW, YF, YS
Validation: HT, XJ, JC
Funding acquisition: BL
Project administration: BL
Supervision: BL, DCR, JW
Writing - original draft: HT
Writing - review & editing: BL, HT, DCR, XJ

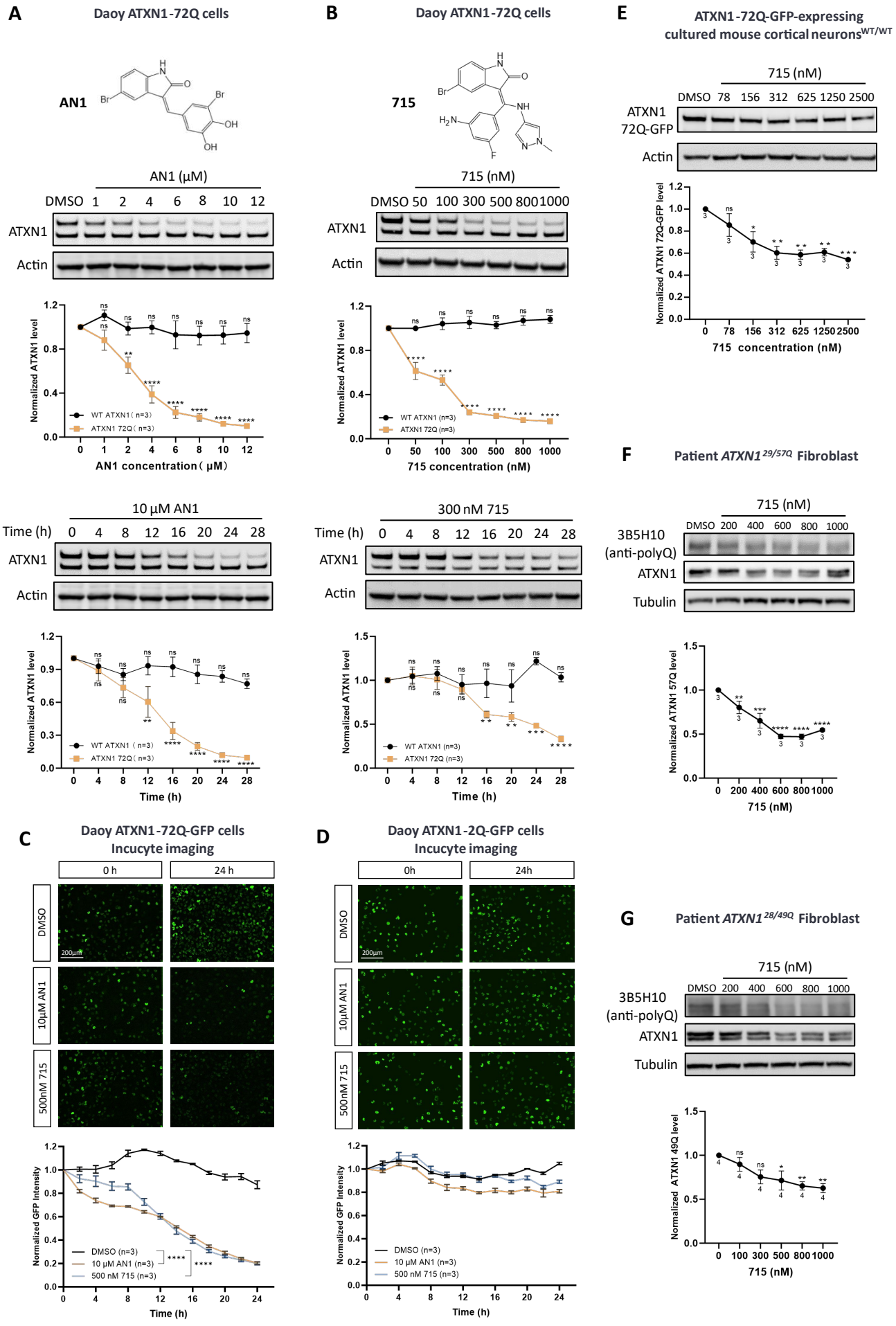
**Competing interests**

DCR has consulted for or is a consultant for Drishti Discoveries, PAQ Therapeutics, MindRank AI, Retro Biosciences, Alexion Pharma International Operations Limited, Carlyle Investment Management LLC, Aladdin Healthcare Technologies Ltd, Nido Biosciences, ProtosBio, and is a co-founder of Acuity Technologies Ltd. BL has consulted for and is a shareholder of PAQ Therapeutics and Shanghai ATTEC Biotechnology Co., Ltd.

**Data and materials availability**

All data supporting the findings of this study are available in the main text or the supplementary materials. The synthesis and characterization of compound 715 are described in the supplementary materials. Additional materials generated in this study are available from the corresponding author upon reasonable request and may be subject to a material transfer agreement.

# Figures


A
Daoy ATXN1-72Q cells
AN1
AN1 (μM)
DMSO 1 2 4 6 8 10 12
ATXN1
Actin
Normalized ATXN1 level
WT ATXN1 (n=3)
ATXN1 72Q (n=3)
AN1 concentration (μM)
B
Daoy ATXN1-72Q cells
715
715 (nM)
DMSO 50 100 300 500 800 1000
715 concentration (nM)
E
ATXN1-72Q-GFP-expressing cultured mouse cortical neurons WT/WT
715 (nM)
DMSO 78 156 312 625 1250 2500
ATXN1 72Q-GFP
Normalized ATXN1 72Q-GFP level
715 concentration (nM)
10 μM AN1
Time (h) 0 4 8 12 16 20 24 28
Time (h)
300 nM 715
F
Patient ATXN1 29/57Q Fibroblast
DMSO 200 400 600 800 1000
3B5H10 (anti-polyQ)
Tubulin
Normalized ATXN1 57Q level
C
Daoy ATXN1-72Q-GFP cells
Incucyte imaging
0 h
24 h
DMSO
10μM AN1
500nM 715
Normalized GFP Intensity
DMSO (n=3)
10 μM AN1 (n=3)
500 nM 715 (n=3)
D
Daoy ATXN1-2Q-GFP cells
Incucyte imaging
0h
24h
G
Patient ATXN1 28/49Q Fibroblast
Normalized ATXN1 49Q level

1213

**Fig. 1. Identification of AN1 and 715 as potent, allele-selective mutant ATXN1 degraders.**

**(A-B)** Chemical structures (Top), representative Western blots, and densitometric quantification showing dose-(Middle) and time-(Bottom) dependent reduction of ATXN1-72Q by AN1 (A) and its optimized derivative 715 (B) in Daoy ATXN1-72Q stable cells. **(C-D)** Live-cell GFP imaging and quantification showing selective reduction of ATXN1-72Q-GFP (C), but not ATXN1-2Q-GFP (D), in Daoy ATXN1-72Q-GFP cells treated with DMSO, 10 μM AN1, or 500 nM 715 for 24 h. **(E)** Representative Western blot and quantification showing dose-dependent reduction of lentivirally expressed ATXN1-72Q-GFP by 715 in WT primary cortical neurons. **(F)** Representative Western blots and densitometric analyses showing the dose-dependent reduction of ATXN1 57Q by 715 in SCA1 patient-derived fibroblasts ($ATXN1^{29Q/57Q}$). **(G)** Representative Western blots and densitometric analyses showing the dose-dependent reduction of ATXN1 49Q by 715 in SCA1 patient-derived fibroblasts ($ATXN1^{28Q/49Q}$). For all panels, n represents the number of independent biological replicates. Data are presented as mean ± SEM. $*P < 0.05$, $**P < 0.01$, $***P < 0.001$, $****P < 0.0001$. Data were normalized to the corresponding control group. Statistical analyses were performed using one-way ANOVA followed by Dunnett's multiple comparisons test for (A-B) and (E-G), and two-way ANOVA followed by Šídák's multiple comparisons test for (C-D).

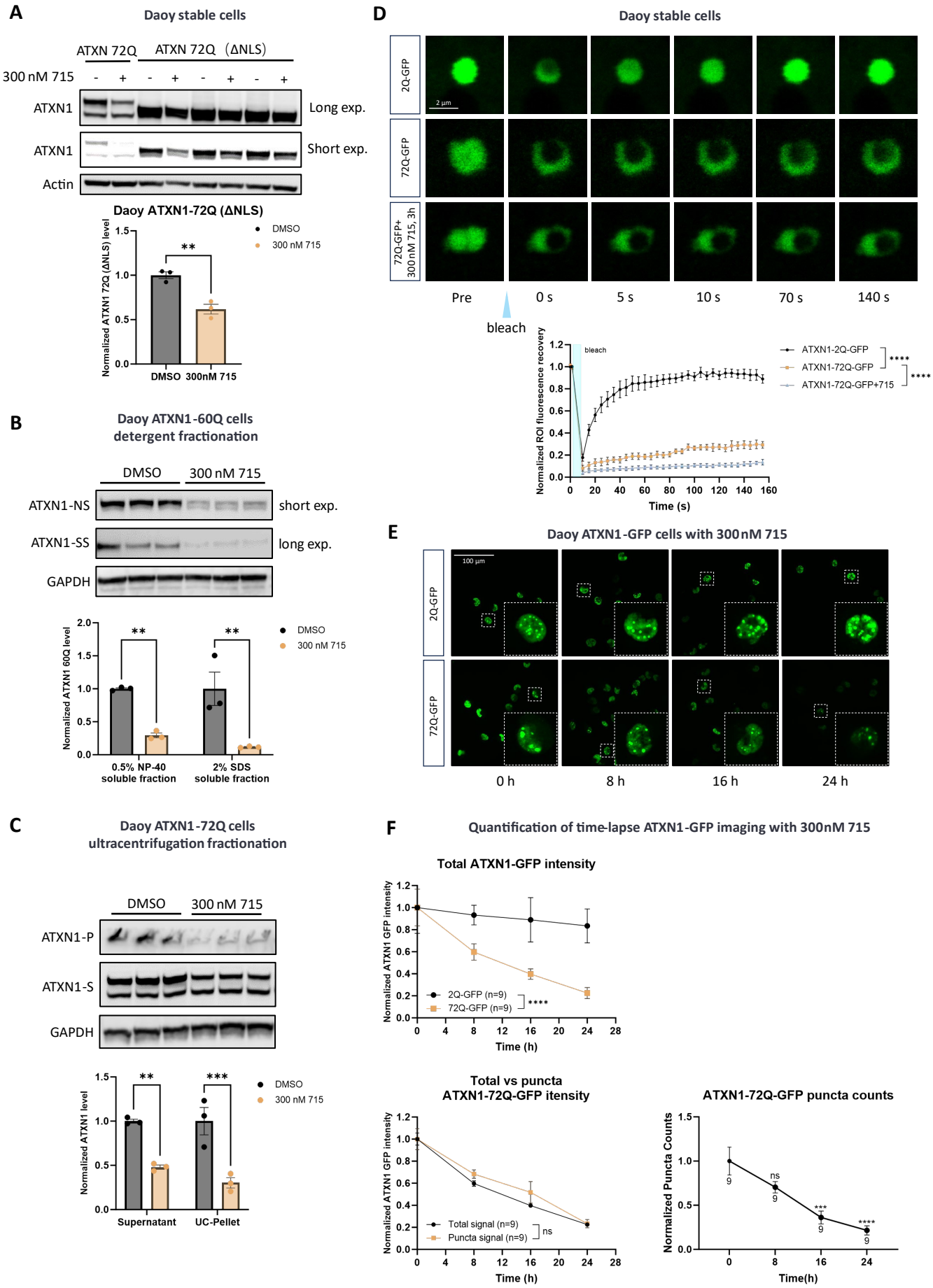



**Fig. 2. 715 degraded both diffuse and aggregate-associated mutant ATXN1 across distinct subcellular localizations.**

**(A)** Representative Western blot showing reduction of nuclear ATXN1-72Q and cytoplasmic ATXN1-72Q ΔNLS after 300 nM 715 treatment in Daoy cells. Quantification of cytoplasmic ATXN1-72Q ΔNLS levels after 715 treatment is shown ($n$ = 3 independent biological replicates). **(B)** Representative Western blots and densitometric quantification of 0.5% NP-40-soluble (NS) and 2% SDS-soluble (SS) ATXN1 fractions from Daoy ATXN1-60Q cells treated with DMSO or 300 nM 715 for 24 h ($n$ = 3 independent biological replicates). **(C)** Representative Western blots and densitometric quantification of soluble and insoluble ATXN1 fractions isolated from Daoy ATXN1-72Q cells treated with DMSO or 300 nM 715 for 24 h. Following mild RIPA lysis, soluble and insoluble fractions were separated by ultracentrifugation. Insoluble ATXN1 signals retained in the gel wells were included in quantification ($n$ = 3 independent biological replicates). **(D)** Fluorescence recovery after photobleaching (FRAP) analysis of ATXN1-GFP mobility in Daoy ATXN1-2Q-GFP and ATXN1-72Q-GFP cells, with or without 300 nM 715 treatment for 3 h. Data were collected from three independent experiments. **(E)** Representative time-lapse confocal images tracking ATXN1-GFP fluorescence in Daoy ATXN1-2Q-GFP and ATXN1-72Q-GFP cells treated with 300 nM 715 over 24 h. **(F)** Quantification of time-lapse ATXN1-GFP imaging in **E**. Plots show total ATXN1-GFP intensity in 2Q-GFP and 72Q-GFP cells, total versus puncta-associated ATXN1-GFP intensity in 72Q-GFP cells, and puncta counts per cell in 72Q-GFP cells. Total signal was calculated as total GFP intensity per cell; puncta signal was calculated as puncta GFP intensity per punctum. Quantification was performed across three independent experiments with three fields of view analyzed per experiment. For quantitative analyses, data are presented as mean ± SEM. *$P < 0.05$, **$P < 0.01$, ***$P < 0.001$, ****$P < 0.0001$. Data were normalized to the corresponding control group. Statistical analyses were performed using a paired two-tailed t-test for A, two-way ANOVA followed by Šídák's multiple comparisons test for (B-D) and (F) (except puncta number quantification), and one-way ANOVA followed by Dunnett's multiple comparisons test for puncta number quantification in (F).

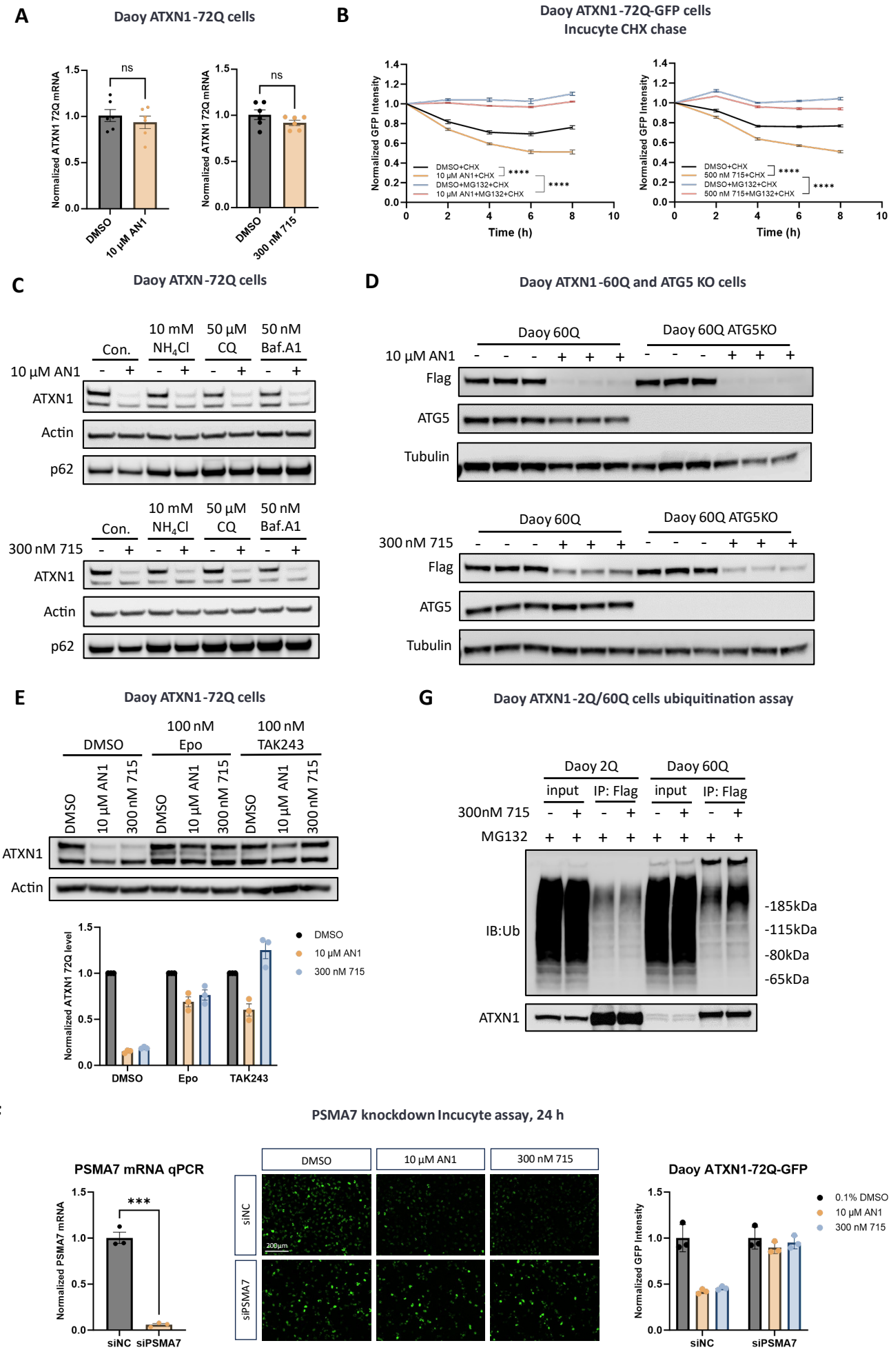

A
Daoy ATXN1-72Q cells
Normalized ATXN1 72Q mRNA
ns
DMSO
10 μM AN1
300 nM 715
B
Daoy ATXN1-72Q-GFP cells
Incucyte CHX chase
Normalized GFP Intensity
Time (h)
DMSO+CHX
10 μM AN1+CHX
DMSO+MG132+CHX
10 μM AN1+MG132+CHX
500 nM 715+CHX
500 nM 715+MG132+CHX
****
C
Daoy ATXN-72Q cells
Con.
10 mM NH4Cl
50 μM CQ
50 nM Baf.A1
10 μM AN1
300 nM 715
ATXN1
Actin
p62
D
Daoy ATXN1-60Q and ATG5 KO cells
Daoy 60Q
Daoy 60Q ATG5KO
Flag
ATG5
Tubulin
E
Daoy ATXN1-72Q cells
DMSO
100 nM Epo
100 nM TAK243
Normalized ATXN1 72Q level
G
Daoy ATXN1-2Q/60Q cells ubiquitination assay
Daoy 2Q
input
IP: Flag
300nM 715
MG132
IB:Ub
-185kDa
-115kDa
-80kDa
-65kDa
F
PSMA7 knockdown Incucyte assay, 24 h
PSMA7 mRNA qPCR
Normalized PSMA7 mRNA
siNC
siPSMA7
Daoy ATXN1-72Q-GFP
0.1% DMSO

**Fig. 3. AN1 and 715 promoted mutant ATXN1 degradation via the ubiquitin-proteasome system rather than autophagy.**

**(A)** qPCR analysis of ATXN1-72Q mRNA levels in Daoy ATXN1-72Q cells treated with 10 μM AN1 or 300 nM 715 for 24 h ($n$ = 6 independent biological replicates). **(B)** Incucyte GFP monitoring in Daoy ATXN1-72Q-GFP cells treated with AN1 or 715 following CHX-induced protein synthesis inhibition, with or without MG132 ($n$ = 3 independent biological replicates). **(C)** Western blot analysis of Daoy ATXN1-72Q cells treated with 10 μM AN1 or 300 nM 715 in the presence of autophagy/lysosomal inhibitors NH4Cl, chloroquine, or bafilomycin A1. **(D)** Western blot analysis of 10 μM AN1- and 300 nM 715-mediated ATXN1 reduction in Daoy ATXN1-60Q cells with or without ATG5 knockout. **(E)** Western blot analysis of Daoy ATXN1-72Q cells co-treated with 10 μM AN1 or 300 nM 715 and the proteasome inhibitor epoxomicin or E1 inhibitor TAK-243 ($n$ = 3 independent biological replicates). **(F)** qPCR validation of PSMA7 knockdown in Daoy ATXN1-72Q cells (Left). Representative Incucyte endpoint images (Middle) and quantification (Right) of ATXN1-72Q-GFP fluorescence are shown after 24 h treatment with DMSO, 10 μM AN1, or 300 nM 715 following PSMA7 knockdown ($n$ = 3 independent biological replicates). **(G)** ATXN1 ubiquitination assay in Daoy ATXN1-2Q and ATXN1-60Q cells co-treated with 300 nM 715 and MG132, followed by Flag-IP and immunoblotting for ubiquitin. For quantitative analyses, n represents the number of independent biological replicates. Data are presented as mean ± SEM. *$P$ < 0.05, **$P$ < 0.01, ***$P$ < 0.001, ****$P$ < 0.0001. Data were normalized to the corresponding control group. Statistical analyses were performed using two-tailed unpaired t-tests for (A) and the qPCR analysis in (F), and two-way ANOVA followed by Šídák's multiple comparisons test for (B).

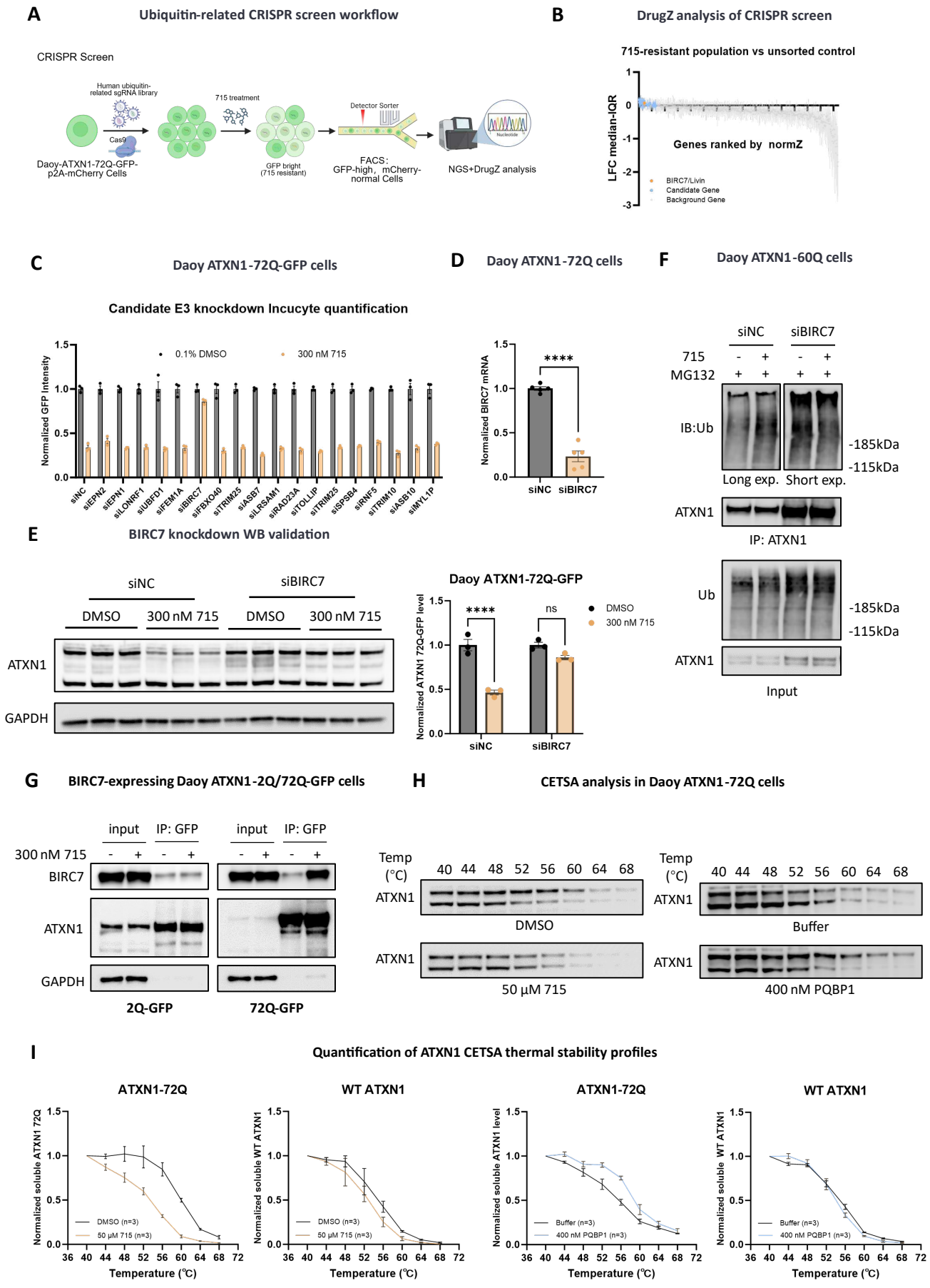
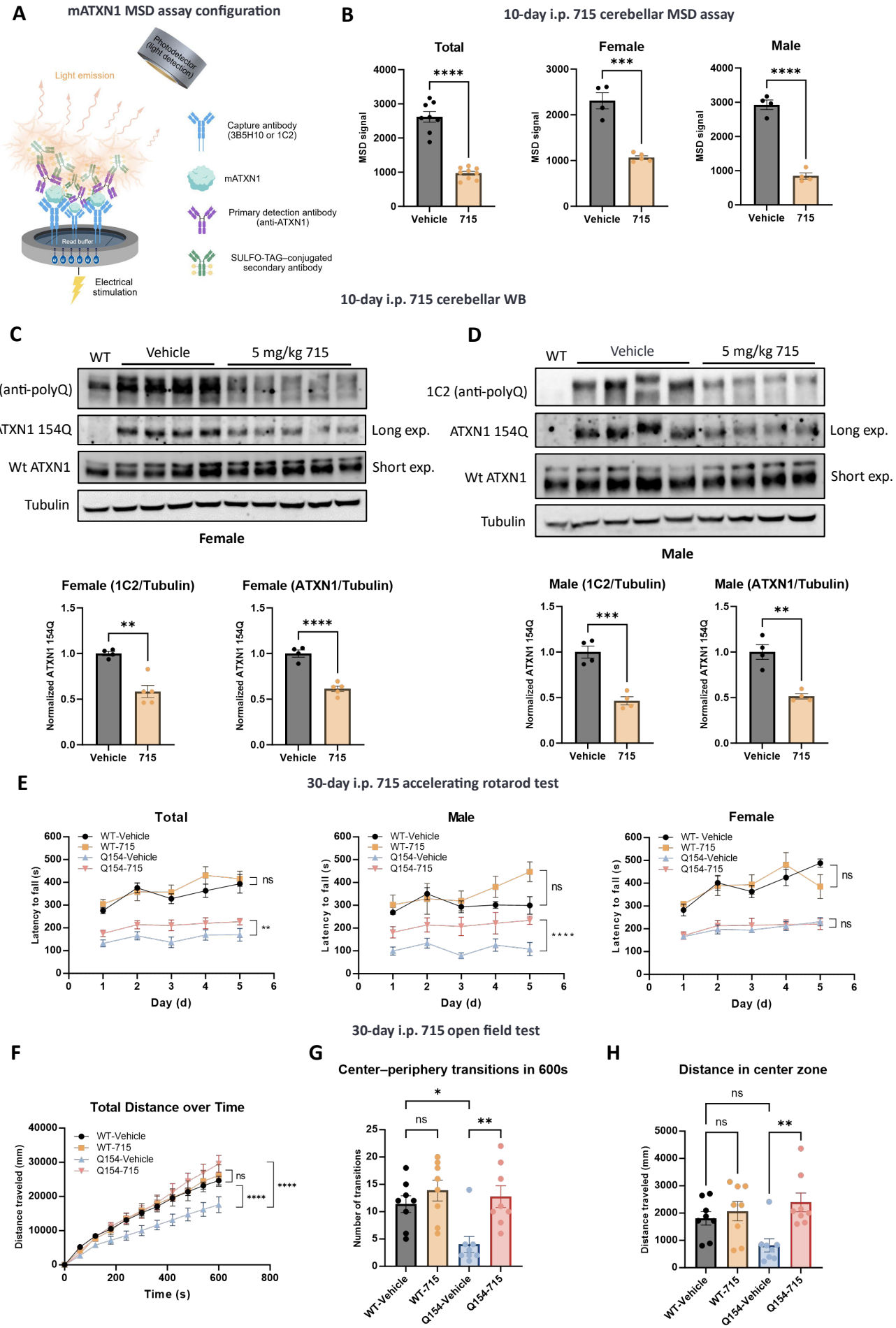



**Fig. 4. A functional CRISPR screen revealed BIRC7 as the primary E3 ligase mediating 715-induced mATXN1 clearance.**

**(A)** Schematic workflow of the ubiquitin-related CRISPR-Cas9 knockout screen in Daoy ATXN1-72Q-GFP-p2A-mCherry cells. Cells were transduced with a human ubiquitin-related sgRNA library, treated with 715, and 715-resistant cells with high ATXN1-72Q-GFP but preserved mCherry signal were isolated by FACS for NGS-based sgRNA enrichment analysis. Schematic created with BioRender.com. **(B)** DrugZ analysis of enriched sgRNAs in the 715-resistant population relative to the unsorted control. The x-axis shows candidate genes ranked by the normalized Z score (normZ) calculated by DrugZ, with normZ reflecting the relative enrichment of sgRNAs targeting each gene in the 715-resistant population. The y-axis represents the distribution of $\log_2$ fold changes (LFCs) for sgRNAs corresponding to each gene, summarized by the median and interquartile range (IQR). Candidate E3 ubiquitin ligases are highlighted in blue, with BIRC7/Livin specifically indicated in orange. **(C)** Incucyte live-cell imaging validation of candidate E3 ligase knockdowns in Daoy ATXN1-72Q-GFP cells during 715 treatment. **(D)** RT-qPCR validation of BIRC7 knockdown in cells transfected with siNC or siBIRC7 ($n = 5$ independent biological replicates). **(E)** Western blot validation of the effect of BIRC7 knockdown on 715-induced ATXN1-72Q-GFP degradation ($n = 3$ independent biological replicates). **(F)** ATXN1 ubiquitination assay following BIRC7 knockdown under 715 treatment and MG132-mediated proteasomal blockade, assessed by ATXN1/Flag immunoprecipitation and ubiquitin immunoblotting. **(G)** Co-immunoprecipitation (Co-IP) analysis of BIRC7 and ATXN1 interaction under 715 treatment in Daoy cells co-expressing ATXN1 (2Q or 72Q)-GFP and BIRC7. **(H)** Representative Western blots from CETSA assays assessing ATXN1 thermal stability in the presence of 400 nM PQBP1 or 50 μM 715. PQBP1 was included as a positive control for validation of the ATXN1 CETSA assay, whereas 715 treatment was used to assess its engagement with mutant ATXN1. **(I)** Quantification of the CETSA thermal stability profiles shown in (H), comparing WT ATXN1 and ATXN1-72Q in the presence of 400 nM PQBP1 and evaluating the thermal stability of mutant ATXN1 following 50 μM 715 treatment ($n = 3$ independent biological replicates). For quantitative analyses, n represents the number of independent biological replicates. Data are presented as mean ± SEM. *$P < 0.05$, **$P < 0.01$, ***$P < 0.001$, ****$P < 0.0001$. Data were normalized to the corresponding control group. Statistical analyses were performed using two-tailed unpaired t-test for (D) and two-way ANOVA followed by Šídák's multiple comparisons test for (E).


A
mATXN1 MSD assay configuration
Photodetector (light detection)
Light emission
Capture antibody (3B5H10 or 1C2)
mATXN1
Primary detection antibody (anti-ATXN1)
SULFO-TAG–conjugated secondary antibody
Read buffer
Electrical stimulation
B
10-day i.p. 715 cerebellar MSD assay
Total
Female
Male
MSD signal
Vehicle
715
10-day i.p. 715 cerebellar WB
C
WT
Vehicle
5 mg/kg 715
1C2 (anti-polyQ)
ATXN1 154Q
Long exp.
Wt ATXN1
Short exp.
Tubulin
Female
D
Male
Female (1C2/Tubulin)
Female (ATXN1/Tubulin)
Male (1C2/Tubulin)
Male (ATXN1/Tubulin)
Normalized ATXN1 154Q
E
30-day i.p. 715 accelerating rotarod test
WT-Vehicle
WT-715
Q154-Vehicle
Q154-715
Latency to fall (s)
Day (d)
ns
30-day i.p. 715 open field test
F
Total Distance over Time
Distance traveled (mm)
Time (s)
G
Center–periphery transitions in 600s
Number of transitions
H
Distance in center zone

1316

**Fig. 5. Intraperitoneal administration of 715 selectively lowered cerebellar mutant ATXN1 and improved behavioral deficits in *Atxn1*$^{154Q/2Q}$ mice.**

**(A)** Schematic of the ATXN1 MSD assay configuration. ATXN1 is captured by immobilized 3B5H10 or 1C2 and detected using an anti-ATXN1 primary antibody followed by a SULFO-TAG–conjugated secondary antibody. Schematic created with BioGDP.com[35]. **(B)** MSD-based quantification of cerebellar mATXN1 levels in *Atxn1*$^{154Q/2Q}$ mice after 10 days of daily i.p. vehicle or 5 mg/kg 715 treatment ($n$ = 4 mice per group for each sex). **(C-D)** Western blot analysis of cerebellar ATXN1 levels in 5-month-old female (C) and male (D) *Atxn1*$^{154Q/2Q}$ mice following daily i.p. administration of vehicle or 5 mg/kg 715 for 10 days ($n$ = 4 mice per group for each sex). **(E)** Accelerating rotarod performance of 7-month-old *Atxn1*$^{154Q/2Q}$ mice following daily i.p. administration of vehicle or 5 mg/kg 715 for 30 days. Rotarod was accelerated from 4 to 40 rpm over 9 min ($n$ = 8 mice per group). **(F–H)** Open field test analysis of *Atxn1*$^{154Q/2Q}$ mice following daily i.p. administration of vehicle or 5 mg/kg 715 for 30 days. Total distance traveled over time (F), center–periphery transitions during the 600-s test (G), and distance traveled in the center zone (H) are shown ($n$ = 8 mice per group). For quantitative analyses, n represents the number of animals analyzed per group. Data are presented as mean ± SEM. *$P$ < 0.05, **$P$ < 0.01, ***$P$ < 0.001, ****$P$ < 0.0001. Statistical analyses were performed using two-tailed unpaired t-test for (B-D), two-way ANOVA followed by Šídák's multiple comparisons test for (E-F), and one-way ANOVA followed by Dunnett's multiple comparisons test for (G-H).

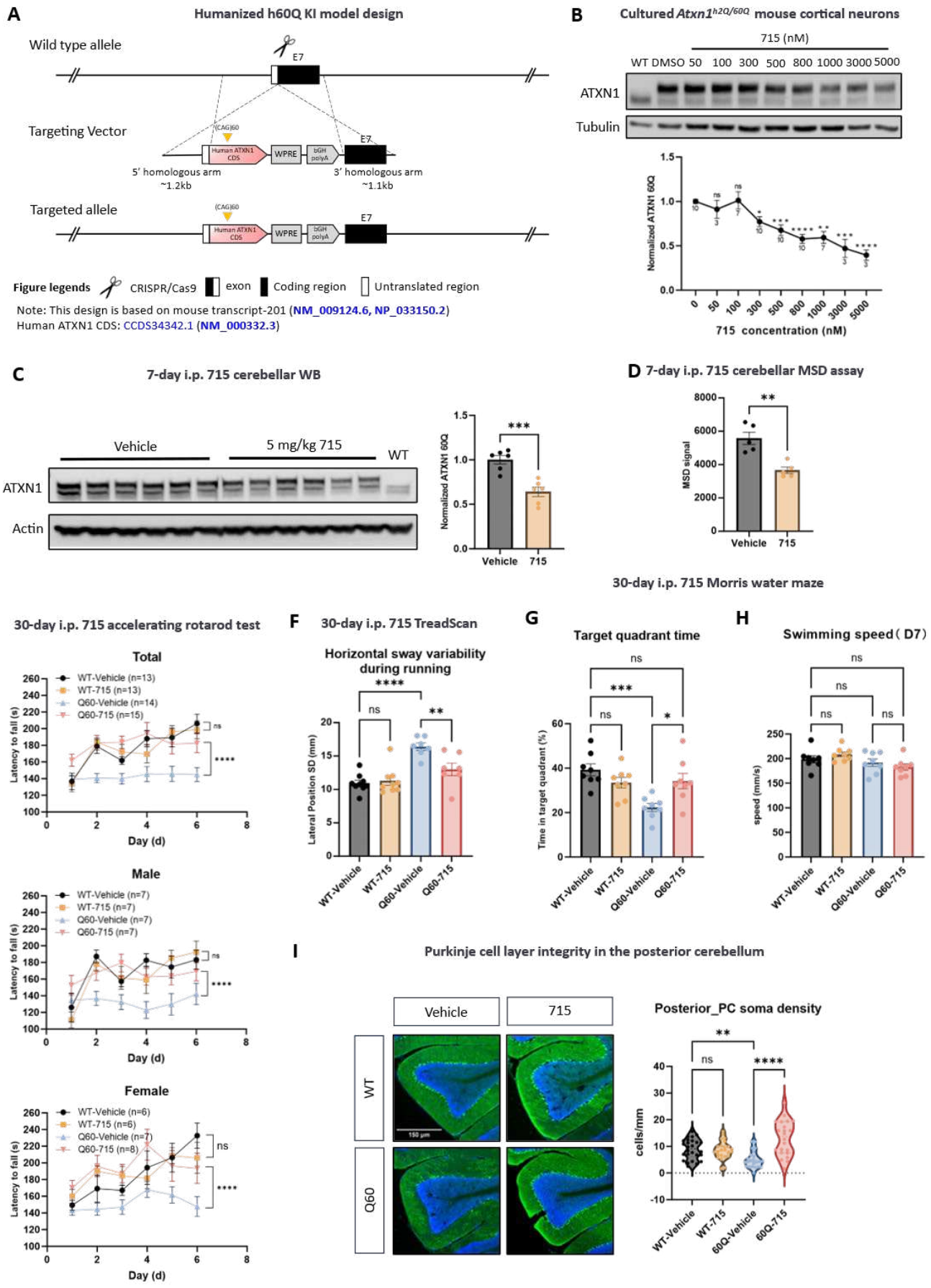



**Fig. 6. Intraperitoneal 715 reduced endogenous mutant ATXN1 and rescued multimodal motor, cognitive, and pathological deficits in *Atxn1*$^{h60Q/2Q}$ knock-in mice.**

**(A)** Schematic illustration of the humanized *Atxn1*$^{h60Q/2Q}$ knock-in mouse model, in which the human ATXN1 CDS containing 60 CAG repeats was integrated into the mouse Atxn1 locus. **(B)** Dose-dependent reduction of endogenous mutant ATXN1 in primary cortical neurons derived from neonatal *Atxn1*$^{h60Q/2Q}$ mice following 715 treatment. **(C)** Western blot analysis of cerebellar ATXN1-60Q levels in 9-month-old *Atxn1*$^{h60Q/2Q}$ mice following daily i.p. administration of vehicle or 5 mg/kg 715 for 7 days ($n$ = 6 mice per group). **(D)** MSD-based quantification of cerebellar ATXN1-60Q levels in 9-month-old *Atxn1*$^{h60Q/2Q}$ mice following daily i.p. administration of vehicle or 5 mg/kg 715 for 7 days ($n$ = 5 mice per group). **(E)** Accelerating rotarod performance of 13-month-old WT and *Atxn1*$^{h60Q/2Q}$ mice following daily i.p. administration of vehicle or 5 mg/kg 715 for 30 days. **(F)** Treadmill-based gait analysis using TreadScan in 13-month-old *Atxn1*$^{h60Q/2Q}$ mice following daily i.p. administration of vehicle or 5 mg/kg 715 for 30 days. Horizontal sway variability was quantified as the standard deviation of lateral position during running (WT, $n$ = 9 mice per group; *Atxn1*$^{h60Q/2Q}$, $n$ = 7 mice per group). **(G-H)** Morris water maze probe trial analysis of 13-month-old WT and *Atxn1*$^{h60Q/2Q}$ mice following daily i.p. administration of vehicle or 5 mg/kg 715 for 30 days, showing time spent in the target quadrant (G) and swimming speed (H) ($n$ = 8 mice per group). **(I)** Representative immunofluorescence images of lobule VIII in the posterior cerebellum and quantification of Purkinje cell body linear density along the Purkinje cell layer. Calbindin (green) and DAPI (blue) were used to visualize Purkinje cells and nuclei, respectively. Quantification was performed from four sections per mouse from four mice per group. For quantitative analyses, n represents the number of independent biological replicates, animals, or samples analyzed as indicated. Data are presented as mean ± SEM. *$P < 0.05$, **$P < 0.01$, ***$P < 0.001$, ****$P < 0.0001$. Statistical analyses were performed using one-way ANOVA followed by Dunnett's multiple comparisons test for (B) and (F-I), two-tailed unpaired t-test for (C-D), and two-way ANOVA followed by Šídák's multiple comparisons test for (E).

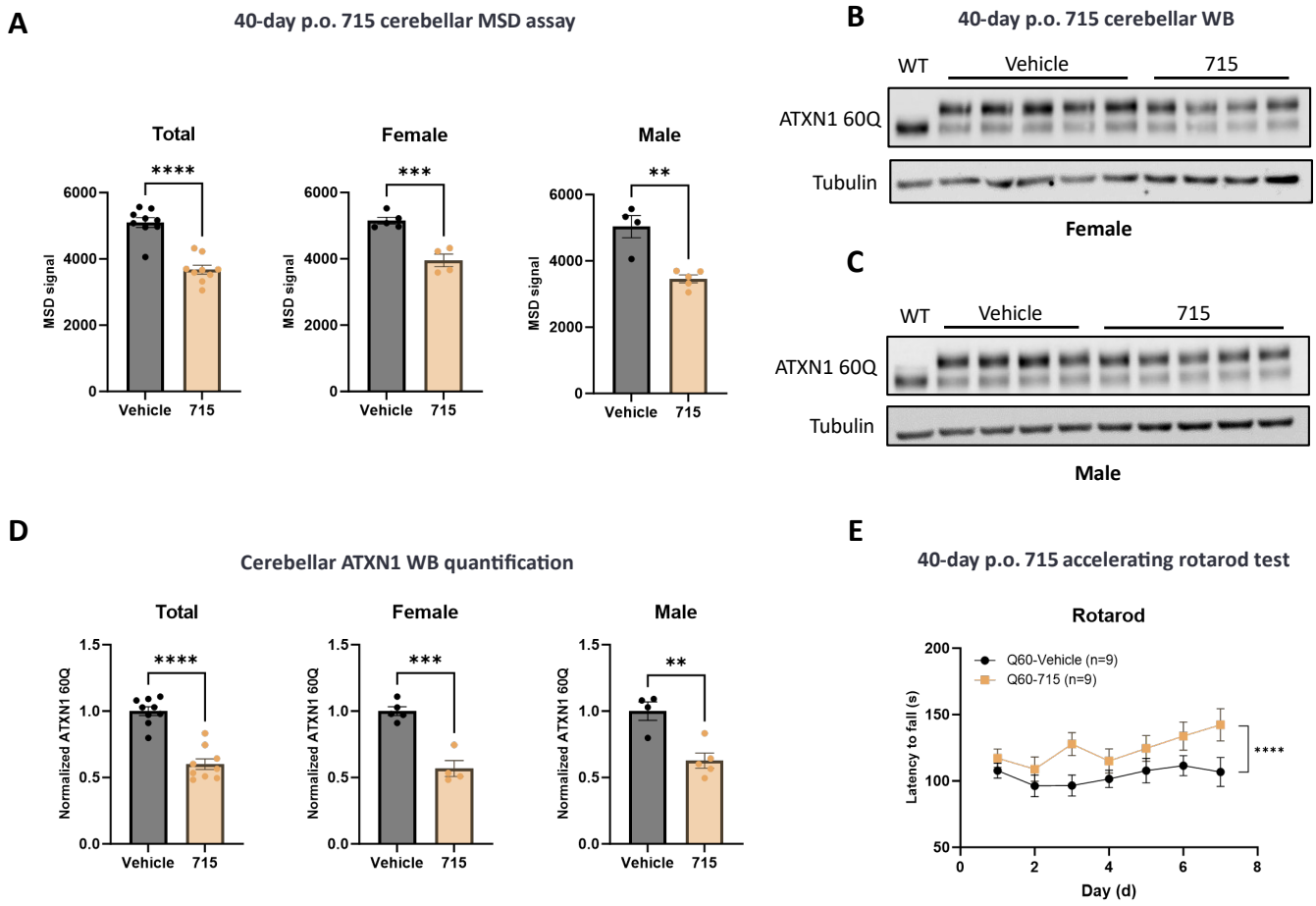



**Fig. 7. Oral administration of 715 reduced cerebellar mutant ATXN1 levels and improved motor performance in *Atxn1*$^{h60Q/2Q}$ mice.**

**(A)** MSD-based quantification of cerebellar mATXN1 levels in *Atxn1*$^{h60Q/2Q}$ mice following 40-day oral administration of 17 mg/kg 715 (female: vehicle, $n = 5$; 715, $n = 4$; male: vehicle, $n = 4$; 715, $n = 5$). **(B-C)** Representative Western blots showing cerebellar ATXN1 levels in female (B) and male (C) *Atxn1*$^{h60Q/2Q}$ mice following 40-day oral administration of 17 mg/kg 715. **(D)** Densitometric quantification of cerebellar mATXN1 levels from female (B) and male (C) mice, including a pooled analysis of both sexes (female: vehicle, $n = 5$; 715, $n = 4$; male: vehicle, $n = 4$; 715, $n = 5$). **(E)** Accelerating rotarod performance of *Atxn1*$^{h60Q/2Q}$ mice following 40-day oral administration of 17 mg/kg 715. For quantitative analyses, n represents the number of animals analyzed per group. Data are presented as mean ± SEM. $^{*}P < 0.05$, $^{**}P < 0.01$, $^{***}P < 0.001$, $^{****}P < 0.0001$. Statistical analyses were performed using two-tailed unpaired t-test for (A) and (D), and two-way ANOVA followed by Šídák's multiple comparisons test for (E).

Supplementary Materials for

# An orally bioavailable allele-selective mutant ATXN1 degrader ameliorates motor and cognitive deficits in a humanized SCA1 knock-in model

Hailiang Tan *et al.*
Corresponding author: wangjian_hs@fudan.edu.cn (Jian Wang); dcr1000@cam.ac.uk (David Rubinsztein); luboxun@fudan.edu.cn (Boxun Lu).

**The file includes:**

Fig. S1 to S11
Table S1 to S3
715 Compound information and validation
715 Compound synthetic route
References (53)

# Supplementary Figures

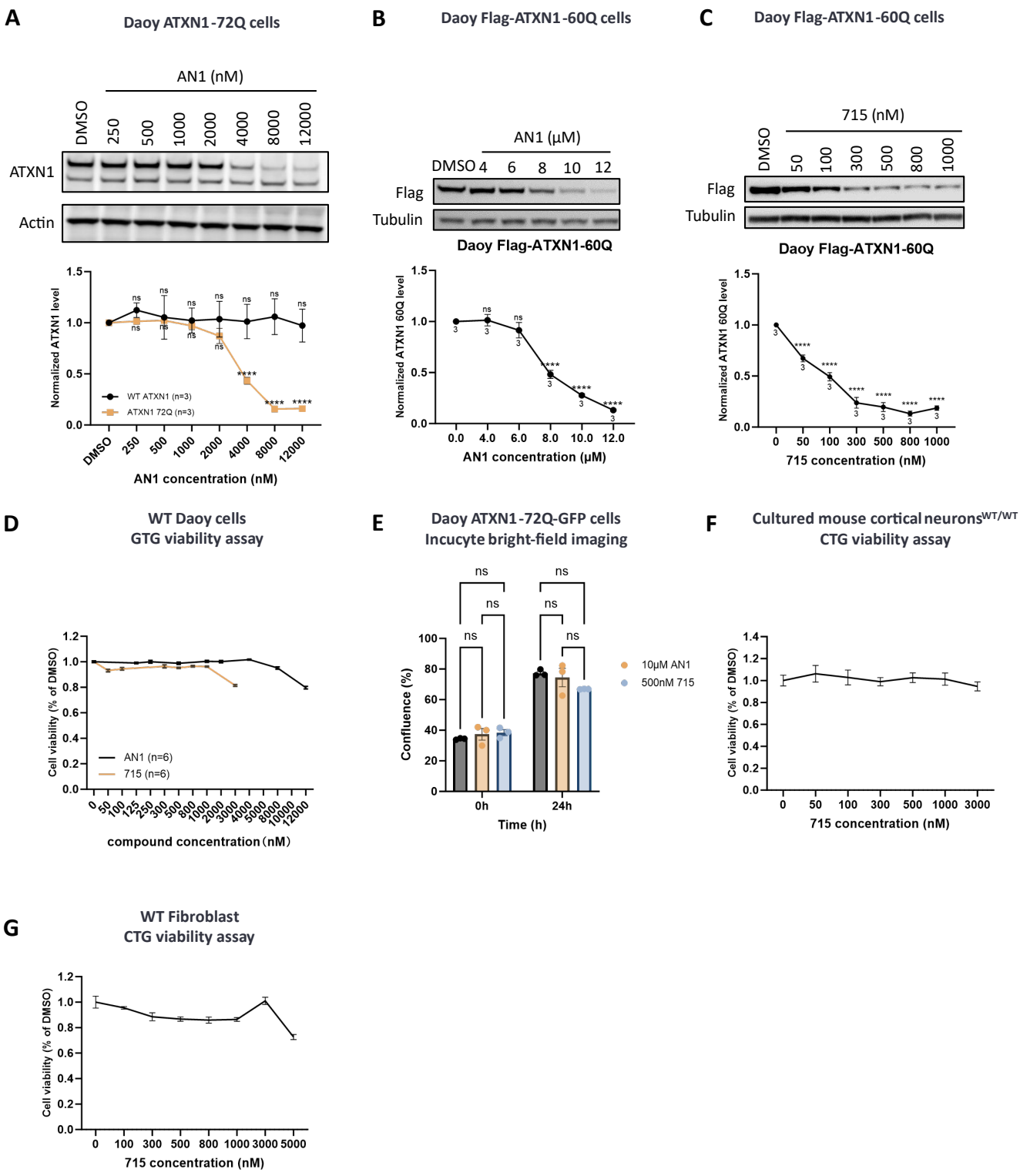


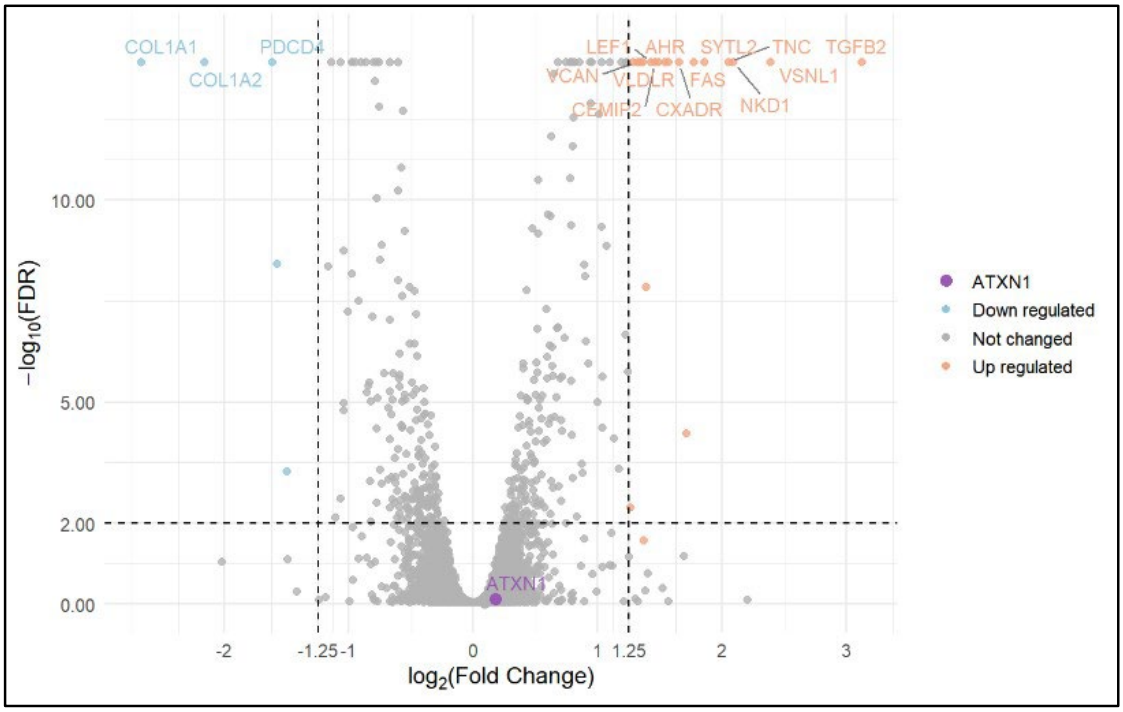

**Fig. S1. relevant to Fig. 1. Supplementary characterization of AN1 and 715 activity, cytotoxicity, and proteome-wide selectivity.**

**(A)** Low-dose AN1 response in Daoy ATXN1-72Q cells. **(B-C)** Dose-dependent reduction of ATXN1-60Q by AN1 (B) or 715 (C) in Daoy ATXN1-60Q cells. **(D)** CTG cell viability assay in Daoy cells treated with AN1 or 715. **(E)** Quantification of cell confluence in Daoy ATXN1-72Q-GFP cells treated with DMSO, 10 μM AN1, or 500 nM 715 for 24 h ($n$ = 3 independent biological replicates). **(F)** CTG cell viability assay in WT primary cortical neurons treated with 715 ($n$ = 5

independent biological replicates). **(G)** CTG cell viability assay in WT primary dermal fibroblasts treated with 715 ($n$ = 5 independent biological replicates). For all panels, n represents the number of independent biological replicates. Data are presented as mean ± SEM. *$P$ < 0.05, **$P$ < 0.01, ***$P$ < 0.001, ****$P$ < 0.0001. Data were normalized to the corresponding control group. Statistical analyses were performed using one-way ANOVA followed by Dunnett's multiple comparisons test for (A-C), and two-way ANOVA followed by Šídák's multiple comparisons test for (E).

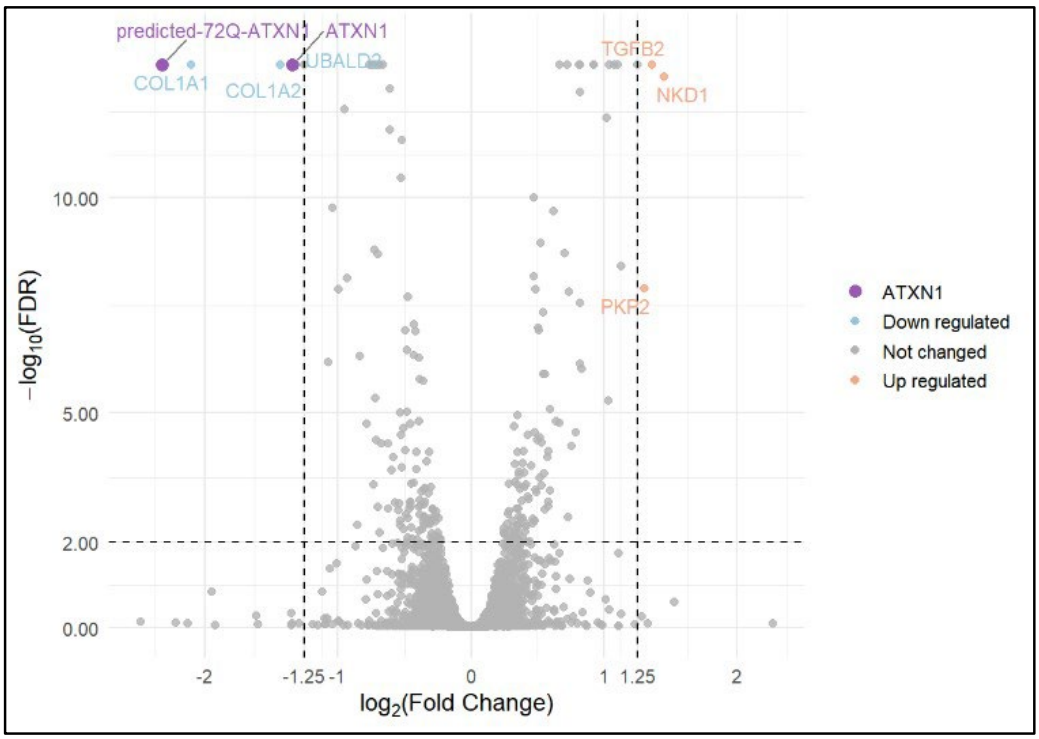
**A**

**WT Daoy cells: 715 vs DMSO proteomics, 24 h**




**B**

**Daoy ATXN1-72Q cells: 715 vs DMSO proteomics, 24 h**




**C**

**WB-based ATXN1-72Q projection for proteomics**

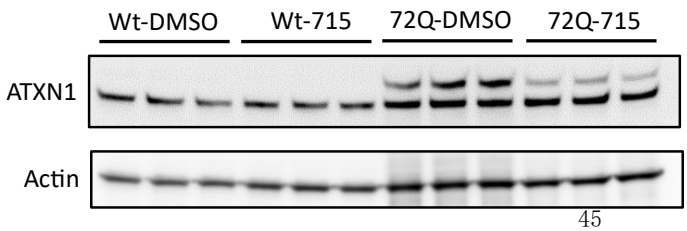


**Fig. S2. relevant to Fig. 1. Proteomic profiling of WT and ATXN1-72Q Daoy cells following 715 treatment.**

**(A, B)** Volcano plots showing proteome-wide changes in WT Daoy cells (A) and Daoy ATXN1-72Q cells (B) after treatment with 300 nM 715 for 24 h compared with DMSO controls ($n$ = 3 biological replicates per condition). Differentially abundant proteins were identified using a DEP/limma-based workflow with Benjamini–Hochberg false discovery rate (FDR) correction. Proteins with FDR < 0.05 and $|\log_2(\text{fold change})| > 1.25$ were classified as significantly altered. Selected differentially abundant proteins are labeled, and ATXN1-related signals are highlighted in purple. **(C)** Representative Western blot of the samples analyzed in (B), used to calculate the mutant-to-WT ATXN1 ratio for ATXN1-72Q proteomic abundance projection.

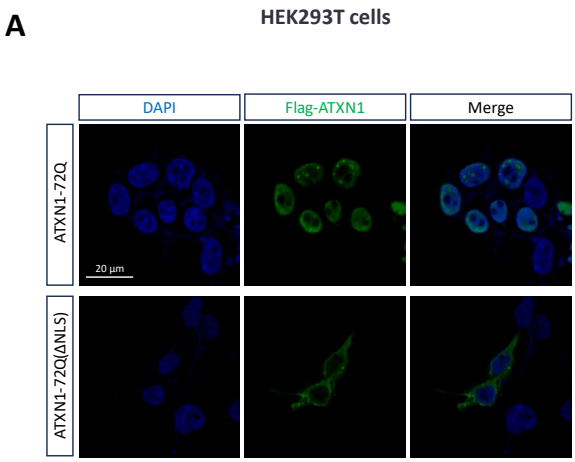



**Fig. S3. relevant to Fig. 2. Validation of ATXN1-72Q ΔNLS cytoplasmic redistribution.**

**(A)** Immunofluorescence (IF) staining of overexpressed Flag-ATXN1 72Q and Flag-ATXN1 72Q (ΔNLS) in HEK293T cells. DAPI marks nuclei and Flag staining marks ATXN1 localization.

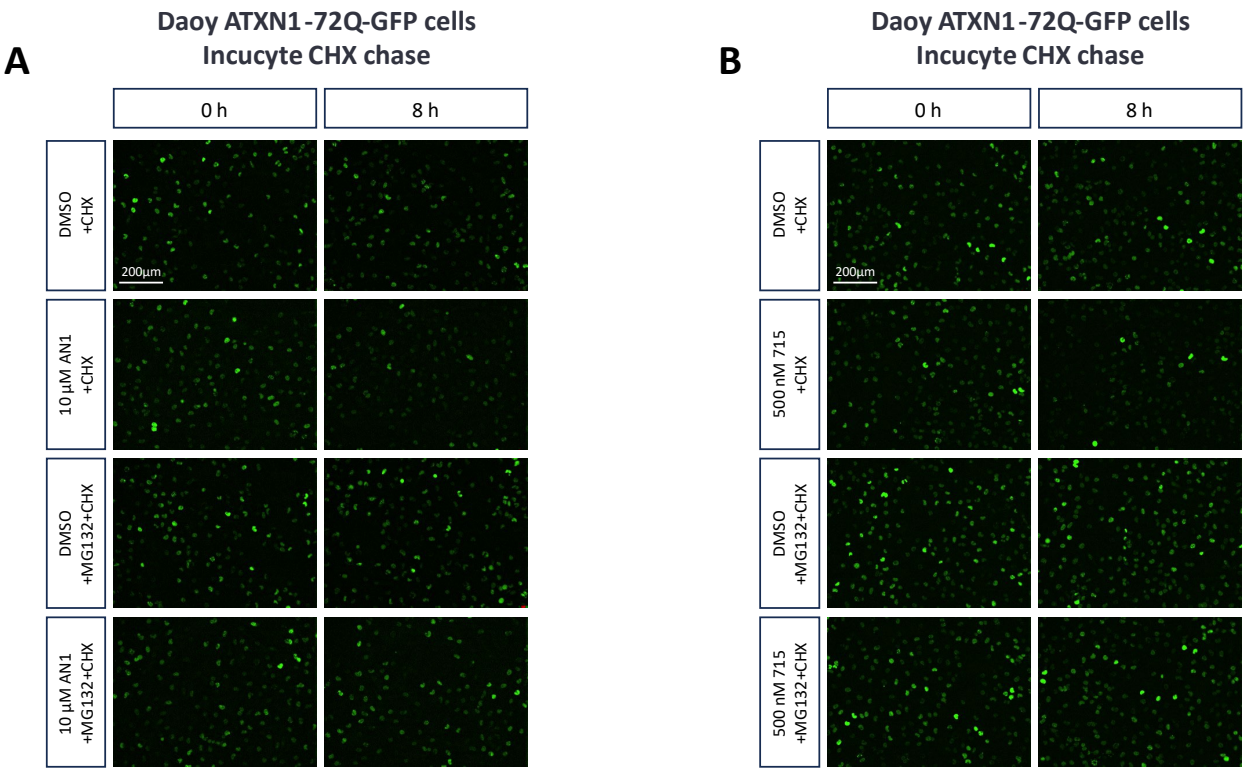
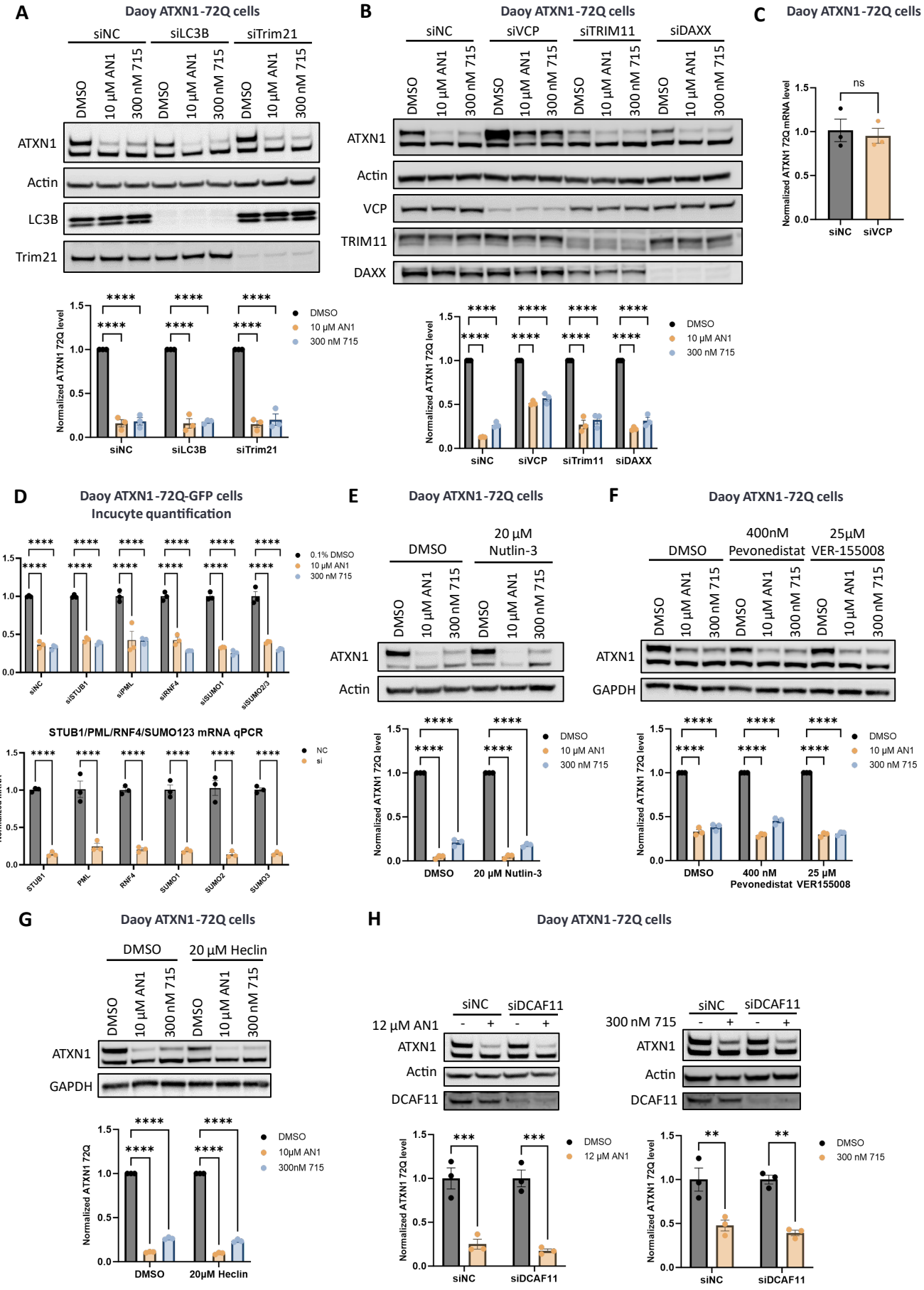



**Fig. S4. relevant to Fig. 3. Representative live-cell imaging of ATXN1-72Q-GFP turnover following AN1 or 715 treatment.**

**(A)** Representative Incucyte images of Daoy ATXN1-72Q-GFP cells at the beginning and end of CHX chase following 10 µM AN1 treatment, with or without MG132. **(B)** Representative Incucyte images of Daoy ATXN1-72Q-GFP cells at the beginning and end of CHX chase following 500 nM 715 treatment, with or without MG132.




1435

1436 **Fig. S5. relevant to Fig. 3. AN1- and 715-mediated mutant ATXN1 degradation was**
1437 **independent of multiple candidate clearance pathways, E3 ligases, chaperones, and unfoldases.**

**(A)** Western blot analysis of 10 μM AN1- and 300 nM 715-mediated ATXN1 reduction following siRNA-mediated knockdown of LC3B or TRIM21 in Daoy ATXN1-72Q cells. **(B)** Western blot analysis of 10 μM AN1- and 300 nM 715-mediated ATXN1 reduction following knockdown of VCP, TRIM11, or DAXX in Daoy ATXN1-72Q cells. **(C)** qPCR analysis of ATXN1-72Q mRNA levels following VCP knockdown. **(D)** Incucyte GFP analysis of 10 μM AN1- and 300 nM 715-mediated ATXN1-72Q-GFP reduction (Top) and qPCR validation (Bottom) following knockdown of STUB1, PML, RNF4, or SUMO1/2/3. **(E)** Western blot analysis of 10 μM AN1- and 300 nM 715-mediated ATXN1 reduction in Daoy ATXN1-72Q cells co-treated with the MDM2 inhibitor Nutlin-3. **(F)** Western blot analysis of 10 μM AN1- and 300 nM 715-mediated ATXN1 reduction in Daoy ATXN1-72Q cells co-treated with the CRL E3 blocker pevonedistat or Hsp70 inhibitor VER-155008. **(G)** Western blot analysis of 10 μM AN1- and 300 nM 715-mediated ATXN1 reduction in Daoy ATXN1-72Q cells co-treated with the HECT E3 inhibitor Heclin. **(H)** Western blot analysis of 12 μM AN1- and 300nM 715-mediated ATXN1 reduction following DCAF11 knockdown in Daoy ATXN1-72Q cells. For all panels, n=3 independent biological replicates. Data are presented as mean ± SEM. *$P < 0.05$, **$P < 0.01$, ***$P < 0.001$, ****$P < 0.0001$. Data were normalized to the corresponding control group. Statistical analyses were performed using two-tailed unpaired t-test for (C), and two-way ANOVA followed by Šídák's multiple comparisons test for others.

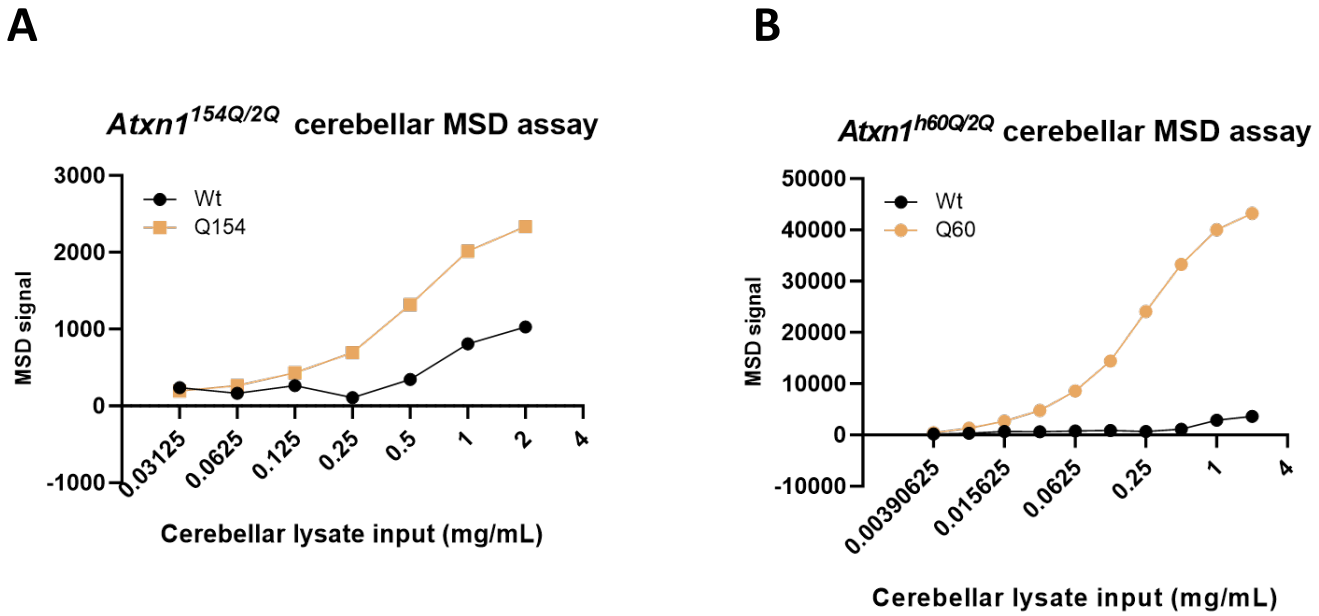
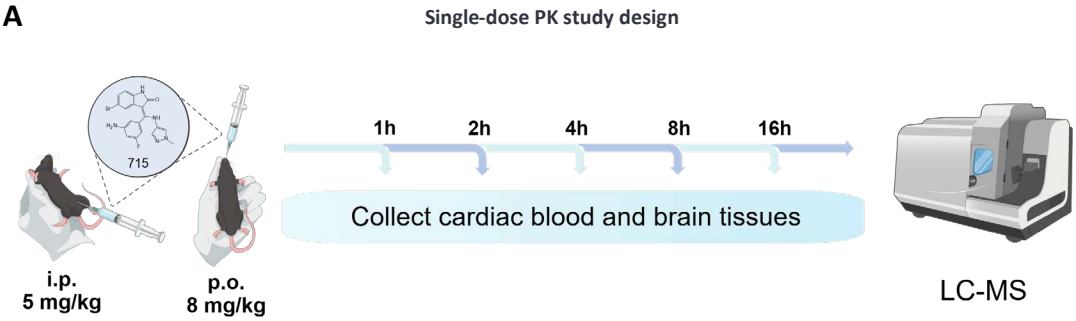


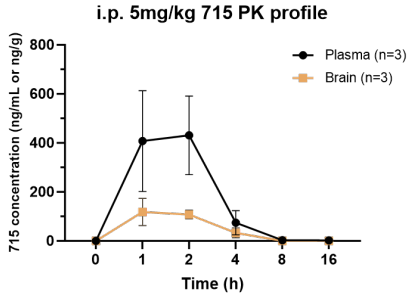

**Fig. S6. relevant to Fig. 5. Validation of the linear dynamic range of the mutant ATXN1 MSD assay in SCA1 mouse cerebellar samples.**

**(A)** Linear dynamic range of MSD assay for *Atxn1*$^{154Q/2Q}$ knock-in mice cerebellar samples (background-subtracted). **(B)** Linear dynamic range of the MSD assay for *Atxn1*$^{h60Q/2Q}$ knock-in mice cerebellar samples (background-subtracted).

**A**



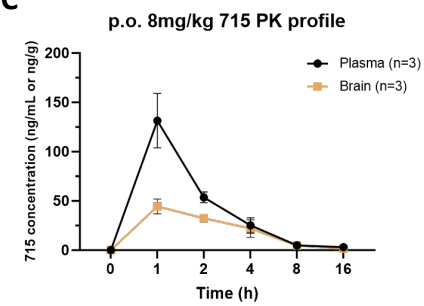

**B**




**Pharmacokinetic parameters of 715 after i.P. administration in mouse**

| | $T_{1/2}$ (h) | $T_{max}$ (h) | $C_{max}$ (ng/mL) | $AUC_{last}$ (h*ng/mL(g)) | $AUC_{INF_obs}$ (h*ng/mL(g)) | $MRT_{INF_obs}$ (h) |
|---|---|---|---|---|---|---|
| Plasma | 2.77 | 2.00 | 431 | 1136 | 1145 | 2.46 |
| Brain | 1.40 | 1.00 | 118 | 331 | 332 | 2.29 |

**C**




**Pharmacokinetic parameters of 715 after p.o administration in mouse**

| | $T_{1/2}$ (h) | $T_{max}$ (h) | $C_{max}$ (ng/mL) | $AUC_{last}$ (h*ng/mL(g)) | $AUC_{INF_obs}$ (h*ng/mL(g)) | $MRT_{INF_obs}$ (h) |
|---|---|---|---|---|---|---|
| Plasma | 1.57 | 1.00 | 132 | 274 | 282 | 2.63 |
| Brain | 2.12 | 1.00 | 44 | 159 | 174 | 3.72 |

**Fig. S7. relevant to Fig. 5-7. Plasma and brain pharmacokinetic profiles of 715 following intraperitoneal versus oral administration.**

**(A)** Experimental design for single-dose pharmacokinetic analysis of 715 in WT mice following i.p. or oral administration. Plasma and brain samples were collected at the indicated time points. Schematic created with BioGDP.com[35]. **(B)** Plasma and brain concentration–time profiles and corresponding pharmacokinetic parameters of 715 following a single i.p. dose of 5 mg/kg. **(C)** Plasma and brain concentration-time profiles and corresponding pharmacokinetic parameters of 715 following a single oral dose of 8 mg/kg. Data are presented as mean ± SEM, and n represents the number of animals analyzed per group.

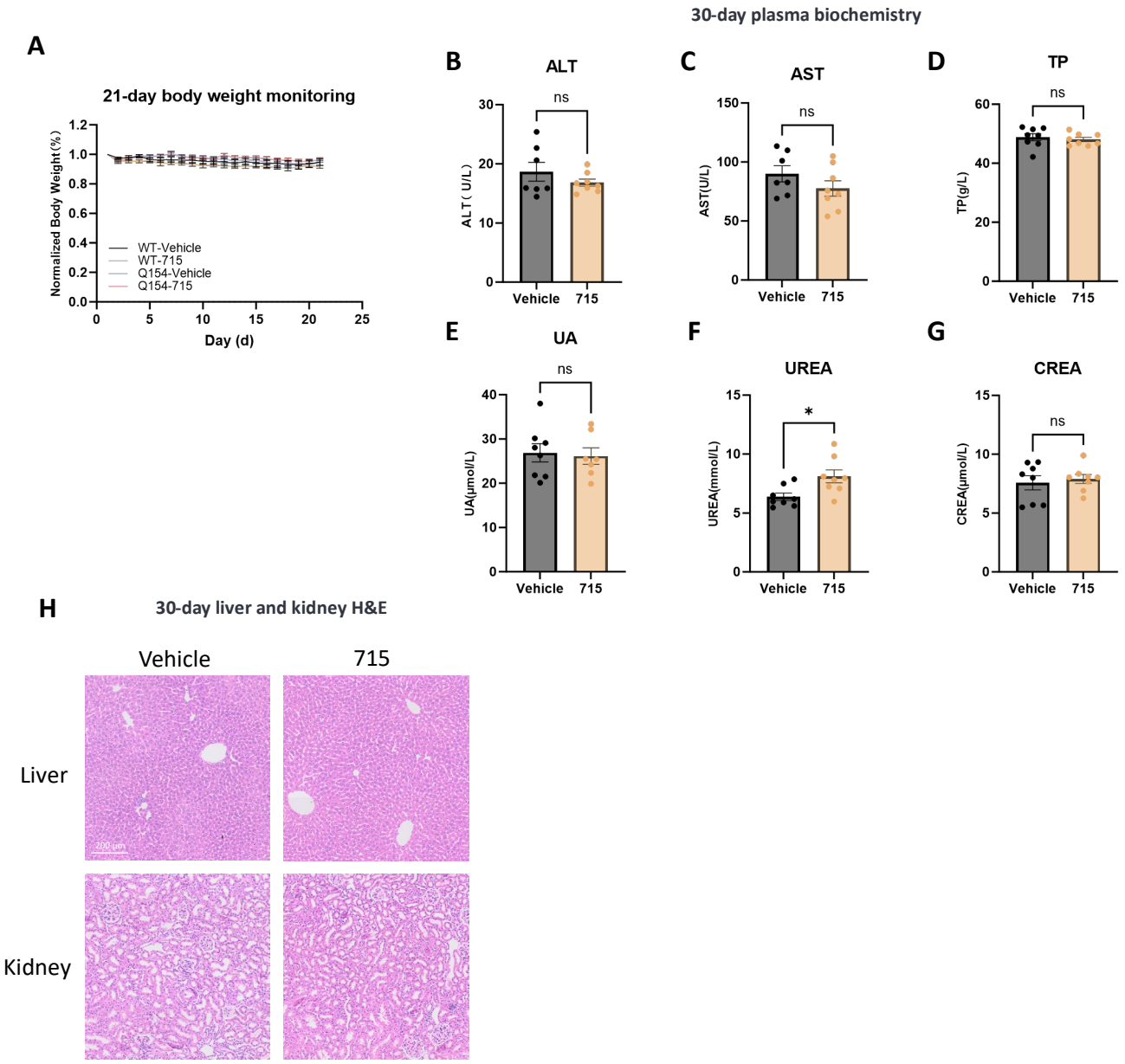



**Fig. S8. relevant to Fig. 5. Prolonged intraperitoneal administration of 715 exhibited a favorable in vivo safety and systemic toxicity profile.**

**(A)** Relative body weight changes of WT and *Atxn1*$^{154Q/2Q}$ mice during 21-day i.p. administration of vehicle or 5 mg/kg 715 ($n$ = 8 mice per group). **(B-G)** Plasma biochemical analysis of WT mice following 30-day i.p. administration of vehicle or 715 ($n$ = 8 mice per group). **(H)** Representative hematoxylin and eosin (H&E) staining of liver and kidney sections from WT mice following 30-day i.p. administration of vehicle or 715. For quantitative analyses, n represents the number of animals analyzed per group. Data are presented as mean ± SEM. *$P$ < 0.05, **$P$ < 0.01, ***$P$ < 0.001, ****$P$ < 0.0001. Statistical analyses were performed using two-tailed unpaired t-test for (B-G).

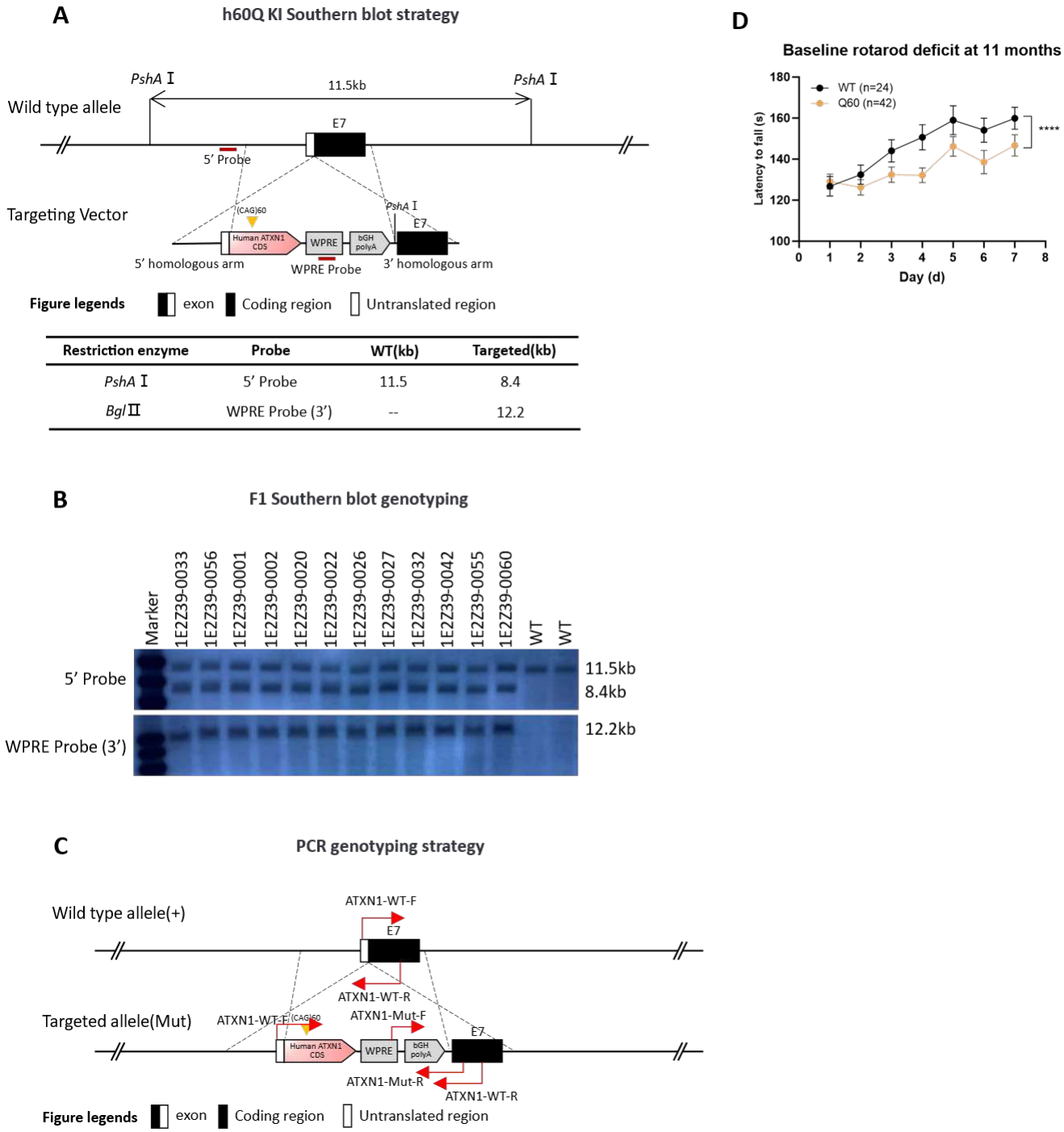



**Fig. S9. relevant to Fig. 6. Generation, molecular validation, and phenotypic characterization of a novel *Atxn1*$^{h60Q/2Q}$ knock-in mouse model.**

**(A)** Schematic design of the Southern blot probe used for screening and identifying the *Atxn1*$^{h60Q/2Q}$ knock-in line. **(B)** Representative Southern blot analysis for genotype identification of F1 generation *Atxn1*$^{h60Q/2Q}$ mice. **(C)** Genotyping primer design for identification of homozygous and heterozygous *Atxn1*$^{h60Q/2Q}$ mice. **(D)** Baseline accelerating rotarod performance of 11-month-old *Atxn1*$^{h60Q/2Q}$ mice. For quantitative analyses, n represents the number of animals analyzed per group. Data are presented as mean ± SEM. *$P < 0.05$, **$P < 0.01$, ***$P < 0.001$, ****$P < 0.0001$. Statistical analyses were performed using two-way ANOVA followed by Šídák's multiple comparisons test for (D).

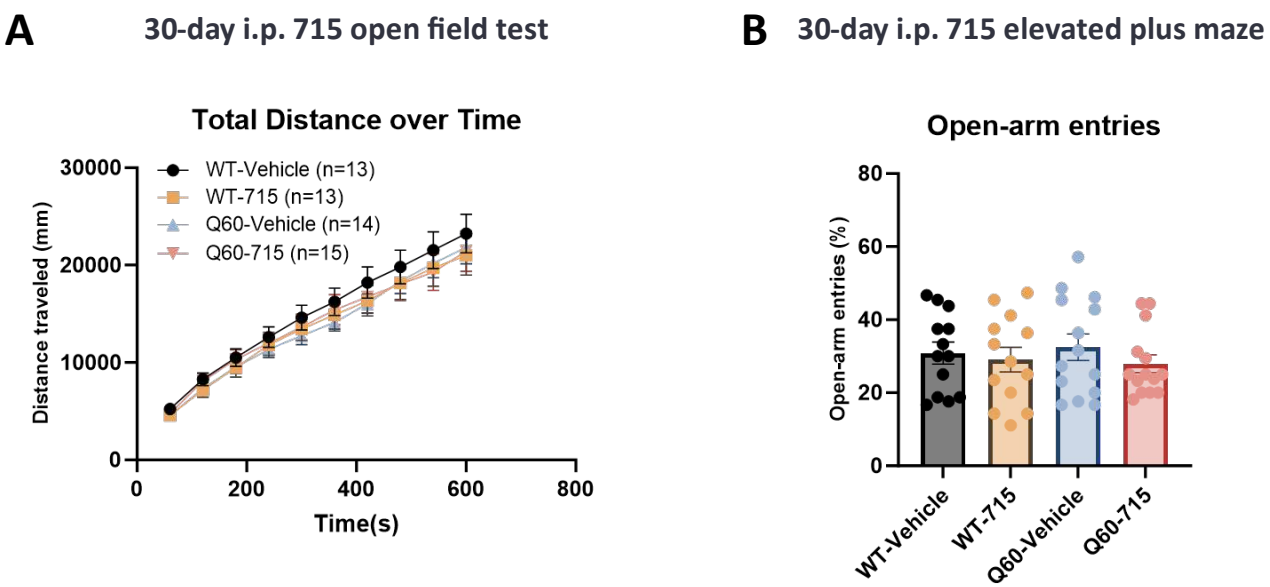



**Fig. S10. relevant to Fig. 6. Chronic 715 treatment did not induce hyperactivity or anxiety-like behaviors in the *Atxn1*$^{h60Q/2Q}$ mice.**

**(A)** Open field test analysis of 13-month-old WT and *Atxn1*$^{h60Q/2Q}$ mice following daily i.p. administration of vehicle or 5 mg/kg 715 for 30 days, assessing general locomotor activity and hyperactivity-related behavioral changes. **(B)** Elevated plus maze analysis of 13-month-old WT and *Atxn1*$^{h60Q/2Q}$ mice following daily i.p. administration of vehicle or 5 mg/kg 715 for 30 days, with anxiety-like behavior assessed by the percentage of open-arm entries (WT, $n$ = 13 mice per group; *Atxn1*$^{h60Q/2Q}$, $n$ = 14 mice per group). Data are presented as mean ± SEM, and n represents the number of animals analyzed per group.

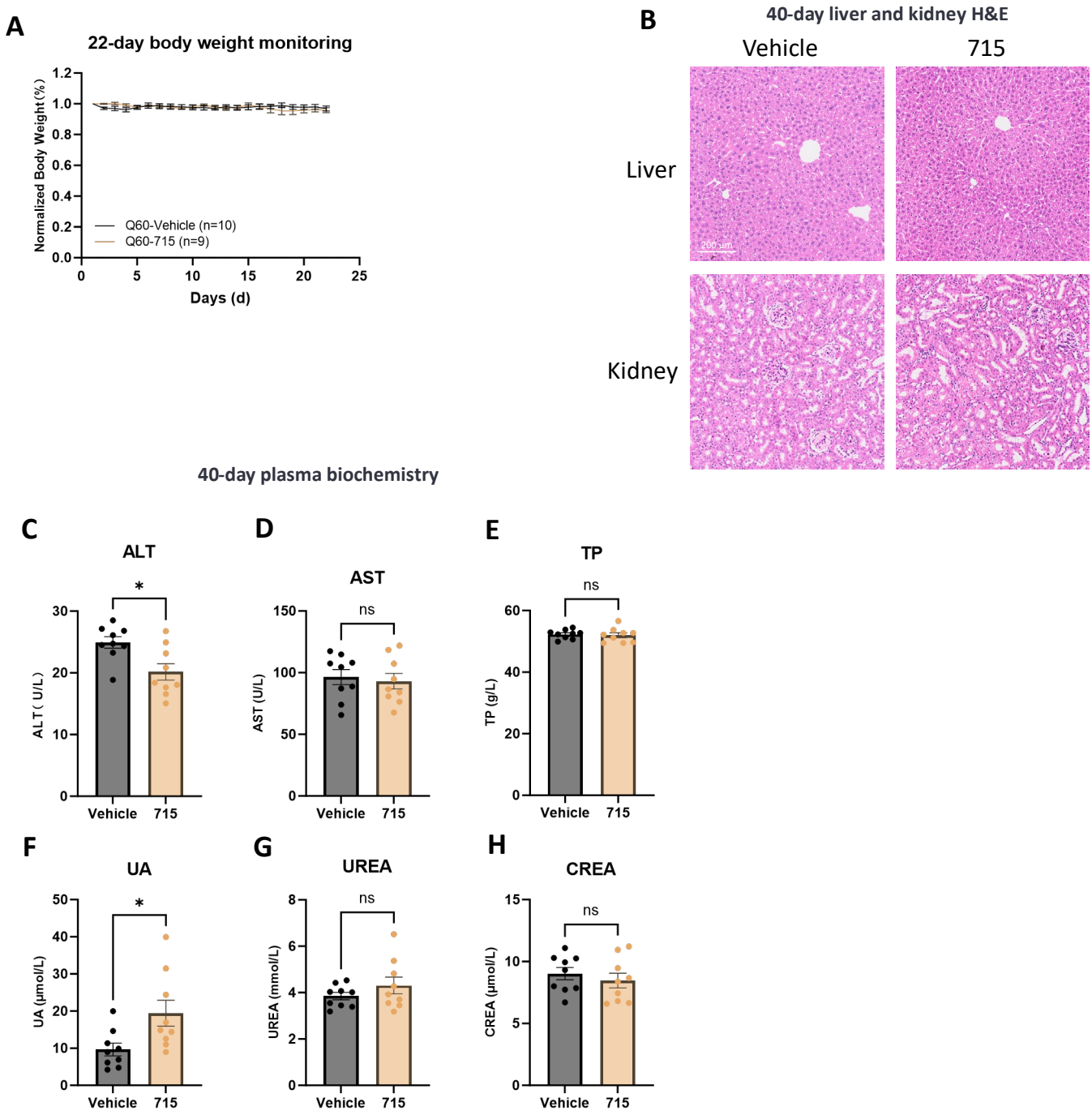



**Fig. S11. relevant to Fig. 7. Systemic safety evaluation after prolonged oral 715 administration.**

**(A)** Relative body weight changes of *Atxn1*$^{h60Q/2Q}$ mice during 22-day oral administration of vehicle or 17 mg/kg 715. **(B)** Representative hematoxylin and eosin (H&E) staining of liver and kidney sections from *Atxn1*$^{h60Q/2Q}$ mice following 40-day oral administration of vehicle or 17 mg/kg 715. **(C-H)** Plasma biochemical analysis of *Atxn1*$^{h60Q/2Q}$ mice following 40-day oral administration of vehicle or 17 mg/kg 715 ($n = 9$ mice per group). For quantitative analyses, n represents the number of animals analyzed per group. Data are presented as mean ± SEM. *$P < 0.05$, **$P < 0.01$, ***$P < 0.001$, ****$P < 0.0001$. Statistical analyses were performed using two-tailed unpaired t-test for (C-H).

# Supplementary Tables

**Table S1 Genotyping Primer Sequences**

| Name | Forward (5'-3') | Reverse (5'-3') |
|---|---|---|
| *Atxn1*$^{154Q/2Q}$ | GTGAGTTTGGGTCTGGCATC | CCAAAAGTTAGGATCACAGCCC |
| *Atxn1*$^{h60Q/2Q}$-WT | CCAATGTGACTCTCTGTTTATCAGAC | GACCCCGGGTTGACTAATCCTGC |
| *Atxn1*$^{h60Q/2Q}$-Mut | GCCCTCAGACGAGTCGGATCTC | CACACCCTCGACACAGTGGTTGTC |

**Table S2 siRNA sequences**

| Name | Sense (5'-3') | Antisense (5'-3') |
|---|---|---|
| siLC3B-1 | GUAUGAGAGUGAGAAAGAUTT | AUCUUUCUCACUCUCAUACTT |
| siLC3B-2 | GUUCGGGAUGAAAUUGUCATT | UGACAAUUUCAUCCCGAACTT |
| siLC3B-3 | GCCGUCGGAGAAGACCUUCTT | GAAGGUCUUCUCCGACGGCTT |
| siTRIM11-1 | CUGAUCCUGUCUGAAGACATT | UGUCUUCAGACAGGAUCAGTT |
| siTRIM11-2 | CAGAAGUUGUGCCUAUGGATT | UCCAUAGGCACAACUUCUGTT |
| siTRIM11-3 | CUAUUCAUCUUUCCCGAGATT | UCUCGGGAAAGAUGAAUAGTT |
| siTRIM11-4 | CUAUUACAAUUCCUCGGAATT | UUCCGAGGAAUUGUAAUAGTT |
| siTRIM21-1 | GCAGCACGCUUGACAAUGATT | UCAUUGUCAAGCGUGCUGCTT |
| siTRIM21-2 | AAUAUUGGAUCACAAGGAUTT | AUCCUUGUGAUCCAAUAUUTT |
| siTRIM21-3 | UCUCAGAGCUAGAUCGAAGTT | CUUCGAUCUAGCUCUGAGATT |
| siTRIM21-4 | GAAUGUGCCUUUACAGGACTT | GUCCUGUAAAGGCACAUUCTT |
| siVCP-1 | GAAUAGAGUUGUUCGGAAUTT | AUUCCGAACAACUCUAUUCTT |
| siVCP-2 | GUAGGGUAUGAUGACAUUGTT | CAAUGUCAUCAUACCCUACUU |
| siVCP-3 | GGGCACAUGUGAUUGUUAUTT | AUAACAAUCACAUGUGCCCTT |
| siDAXX | GGAGUUGGAUCUCUCAGAATT | UUCUGAGAGAUCCAACUCCTT |
| siBIRC7-1 | UGAGGUGCUUCUUCUGCUAUGTT | CAUAGCAGAAGAAGCACCUCATT |
| siBIRC7-2 | UCAGUUCCUGCUCCGGUCAAATT | UUUGACCGGAGCAGGAACUGATT |
| siBIRC7-3 | GAGAGAGGUCCAGUCUGAAAGTT | CUUUCAGACUGGACCUCUCUCTT |
| siPSMA7-1 | GAGGAAGAGACAUUGUUGUTT | ACAACAAUGUCUCUUCCUCTT |
| siPSMA7-2 | GUGCUUUGGAUGACAACGUTT | ACGUUGUCAUCCAAAGCACTT |
| siPSMA7-3 | CCAUUAAGCUGGUGAUCAATT | UUGAUCACCAGCUUAAUGGTT |
| siSTUB1-1 | CCAAGCACGACAAGUACAUTT | AUGUACUUGUCGUGCUUGGTT |
| siSTUB1-2 | CUCUUCGAAUCGCGAAGAATT | UUCUUCGCGAUUCGAAGAGTT |
| siSTUB1-3 | CCUUGUGCUACCUGAAGAUTT | AUCUUCAGGUAGCACAAGGTT |

| Name | Sense (5’-3’) | Antisense (5’-3’) |
|---|---|---|
| siPML-1 | CUCCAAGAUCUAAACCGAGAATT | UUCUCGGUUUAGAUCUUGGAGTT |
| siPML-2 | CACCCGCAAGACCAACAACAUTT | AUGUUGUUGGUCUUGCGGGUGTT |
| siRNF4-1 | CCCUGUUUCCUAAGAACGAAATT | UUUCGUUCUUAGGAAACAGGGTT |
| siRNF4-2 | UAGGCCGAGCUUUGCGGGAAATT | UUUCCCGCAAAGCUCGGCCUATT |
| siRNF4-3 | AAGACUGUUUCGAAACCAACATT | UGUUGGUUUCGAAACAGUCUUTT |
| siSUMO1-1 | UCAAGAAACUCAAAGAAUCTT | GAUUCUUUGAGUUUCUUGATT |
| siSUMO1-2 | GACAGGGUGUUCCAAUGAATT | UUCAUUGGAACACCCUGUCTT |
| siSUMO1-3 | GGUUUCUCUUUGAGGGUCATT | UGACCCUCAAAGAGAAACCTT |
| siSUMO1-4 | GAAUAAAUGGGCAUGCCAATT | UUGGCAUGCCCAUUUAUUCTT |
| siSUMO2/3-1 | CCCAUUCCUUUAUUGUACATT | UGUACAAUAAAGGAAUGGGTT |
| siSUMO2/3-2 | CAGAGAAUGACCACAUCAATT | UUGAUGUGGUCAUUCUCUGTT |
| siSUMO2/3-3 | CAGUUAUGUUGUCGUGUAUTT | AUACACGACAACAUAACUGTT |
| siNC | UUCUCCGAACGUGUCACGUTT | ACGUGACACGUUCGGAGAATT |

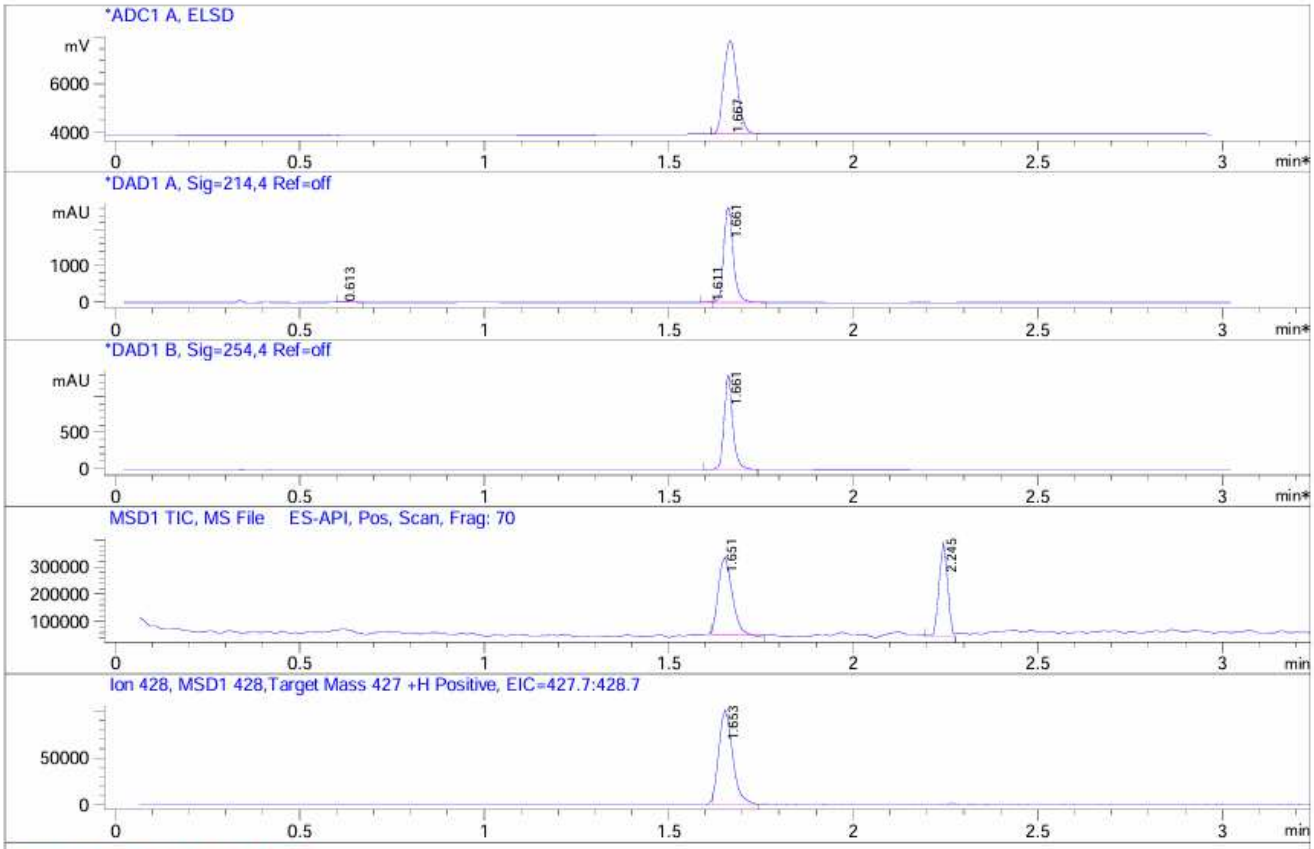
**Table S3 qPCR Primer Sequences**

| Name | Forward (5’-3’) | Reverse (5’-3’) |
|---|---|---|
| human ATXN1 | CAGAACCAGTACGTCCACATTT | GGCGTATTGCATGACGACCT |
| Exp. ATXN1 72Q | GGAGGTCTATATAAGCAGAGCTCGTT | CTCGATCTTCTGGGCCTCAAA |
| human β-ACTIN | CATGTACGTTGCTATCCAGGC | CTCCTTAATGTCACGCACGAT |
| human BIRC7 | TGTCCACAGTGTGCAGGAGACT | GGCACTTTCAGACTGGACCTCT |
| human PSMA7 | CAATGCCATAGGTCGGGGTG | TTTGCCACCTGACTGAACCA |
| human STUB1 | GCCAATCTGCAGCGAGCTTA | CAATGCTGTTCCAGCGCTTC |
| human PML | ACCCGCAAGACCAACAACAT | CATCCTCGGCAGTAGATGCT |
| human RNF4 | TCAGAAGCGAACTCGGGAAG | GATCAACCACCACAGGCTCT |
| human SUMO1 | ATGTCTGACCAGGAGGCAAA | TCTCACTGCTATCCTGTCCA |
| human SUMO2 | AGGATGGTTCTGTGGTGCAG | TCCTCCATTTCCAACTGTCGT |
| human SUMO3 | AGGAGGGTGTGAAGACAGAGA | ATCTTGAACTGCACCACGGA |

# 715 Compound information and validation

LC/MS Report

```
File D:\DATA\C60\MONITOR\CP-0042148-097-P-07642-LCMSA014.D
Injection Date    : 20 Jan 25  11:57 am +0800       Tgt Mass(EZX) : 427.00
Sample Name       : CP-0042148-097-P                     Location : P2-E-09
Acq. Operator     : C60-MONITOR                             Inj : 1
Spec. Reported    : MS Integration                    Inj Volume : 3 ul
Acq. Method       : D:\METHODS\1-POS-3MIN.M
Analysis Method   : D:\METHODS\1-POS-3MIN.M
Sample Info : Easy-Access Method: '1-POS-3MIN'  427.00
Method Info : Mobile Phase:  A: water(0.01%TFA)  B:ACN(0.01%TFA)
              Gradient: 5%B increase to 95%B within 1.4 min,95%B for 1.6min
              Flow Rate:2.0ml/min
              Column :SunFire C18, 4.6*50mm, 3.5um
              Oven Temperature :45C
              Detection:UV(214,4nm) and MS(ESI,Pos mode,132 to 1500 amu)
```




Integration Results for ADC1 A, ELSD

| RetTim | Width | Area | Height | Area% |
|---|---|---|---|---|
| 1.67 | 0.04 | 10095.13 | 3942.60 | 100.00 |

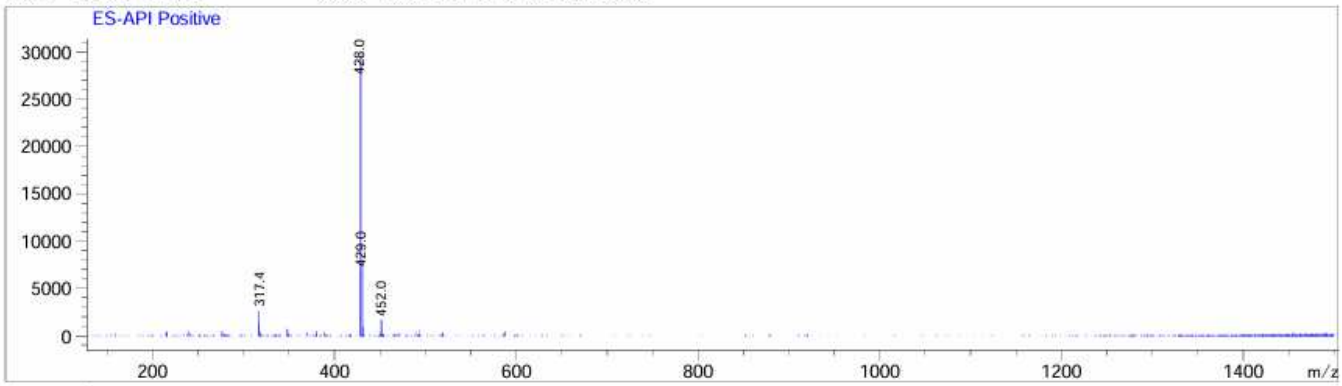
Integration Results for DAD1 A, Sig=214,4 Ref=off

| RetTim | Width | Area | Height | Area% |
|---|---|---|---|---|
| 0.61 | 0.03 | 14.21 | 7.29 | 0.29 |
| 1.61 | 0.02 | 24.57 | 20.34 | 0.50 |
| 1.66 | 0.03 | 4829.71 | 2646.83 | 99.20 |

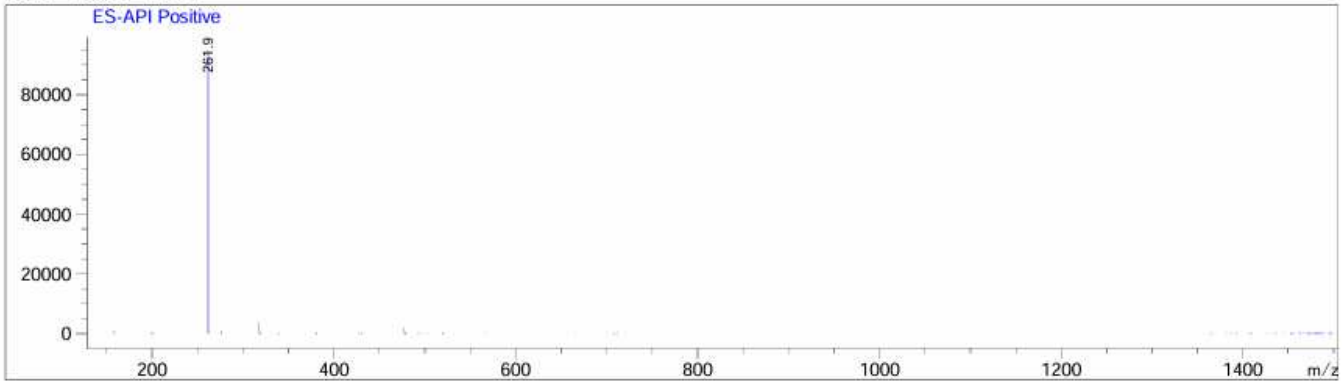
Integration Results for DAD1 B, Sig=254,4 Ref=off

| RetTim | Width | Area | Height | Area% |
|---|---|---|---|---|
| 1.66 | 0.02 | 2173.51 | 1321.45 | 100.00 |

Ret. Time: 1.65 <<<< POSITIVE SPECTRA >>>>

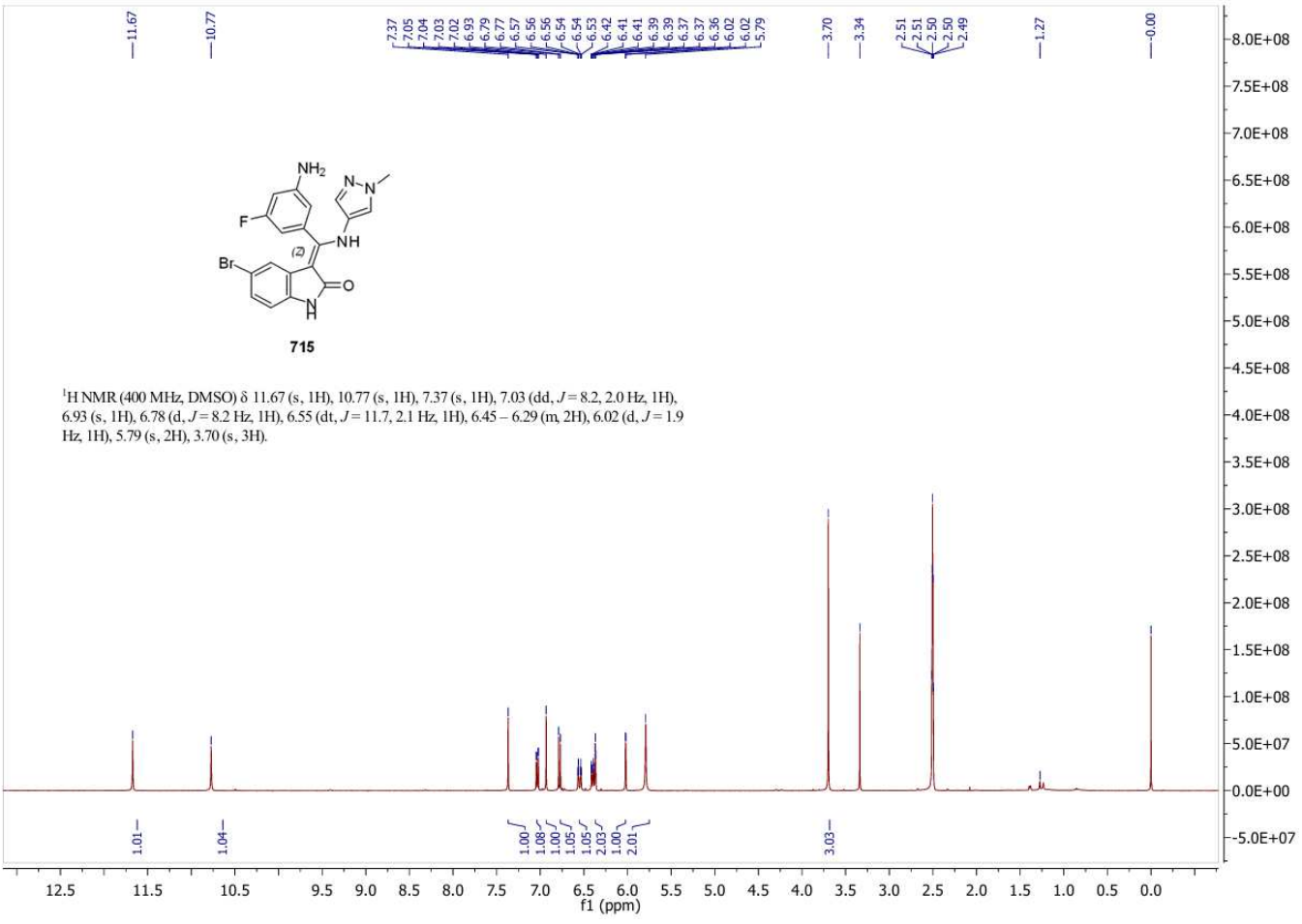



Ret. Time: 2.24

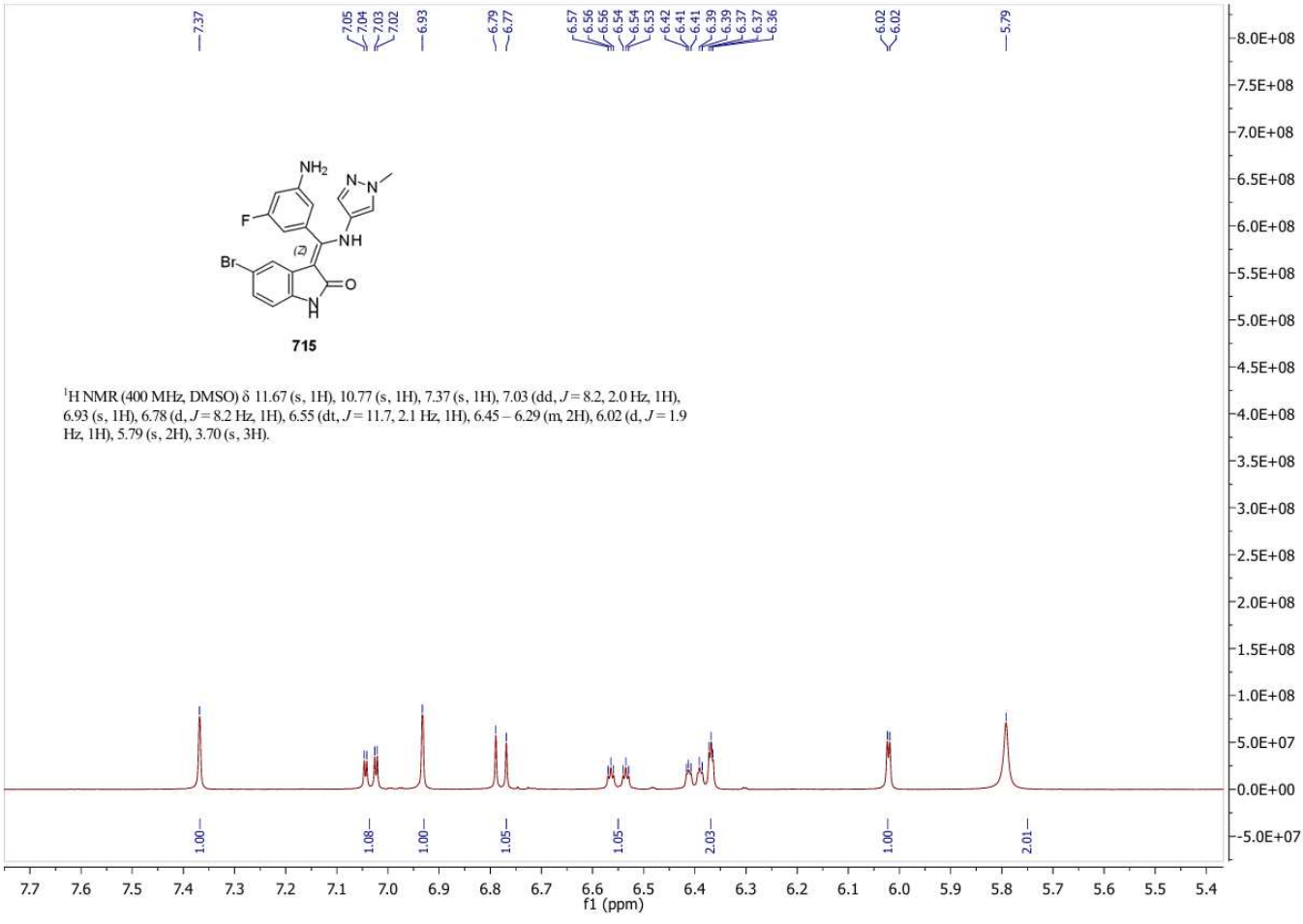



1529

1530

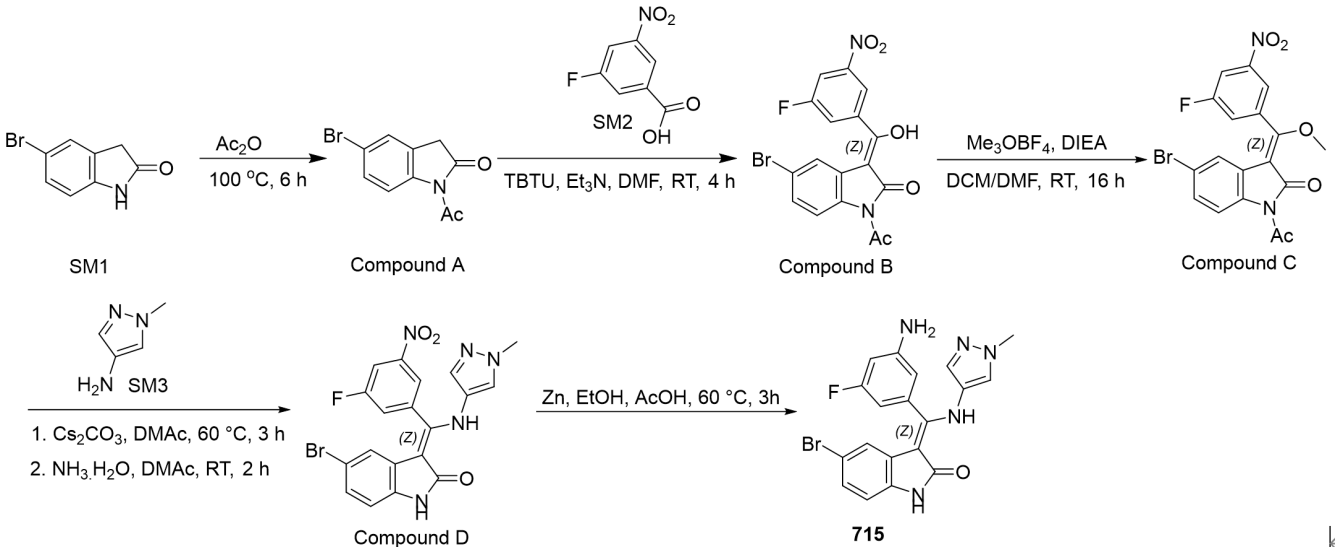

11.67
10.77
7.37
7.05
7.04
7.03
7.02
6.93
6.79
6.77
6.57
6.56
6.56
6.54
6.54
6.53
6.42
6.41
6.41
6.39
6.39
6.37
6.37
6.36
6.02
6.02
5.79
3.70
3.34
2.51
2.51
2.50
2.50
2.49
1.27
0.00
NH2
F
N
N
NH
(Z)
Br
O
N
H
715
1H NMR (400 MHz, DMSO) δ 11.67 (s, 1H), 10.77 (s, 1H), 7.37 (s, 1H), 7.03 (dd, J = 8.2, 2.0 Hz, 1H), 6.93 (s, 1H), 6.78 (d, J = 8.2 Hz, 1H), 6.55 (dt, J = 11.7, 2.1 Hz, 1H), 6.45 – 6.29 (m, 2H), 6.02 (d, J = 1.9 Hz, 1H), 5.79 (s, 2H), 3.70 (s, 3H).
1.01
1.04
1.00
1.08
1.00
1.05
2.03
1.00
2.01
3.03
f1 (ppm)

1531


7.37
7.05
7.04
7.03
7.02
6.93
6.79
6.77
6.57
6.56
6.56
6.54
6.54
6.53
6.42
6.41
6.41
6.39
6.39
6.37
6.37
6.36
6.02
6.02
5.79
NH2
F
N
N
NH
(Z)
Br
O
N
H
715
1H NMR (400 MHz, DMSO) δ 11.67 (s, 1H), 10.77 (s, 1H), 7.37 (s, 1H), 7.03 (dd, J = 8.2, 2.0 Hz, 1H), 6.93 (s, 1H), 6.78 (d, J = 8.2 Hz, 1H), 6.55 (dt, J = 11.7, 2.1 Hz, 1H), 6.45 – 6.29 (m, 2H), 6.02 (d, J = 1.9 Hz, 1H), 5.79 (s, 2H), 3.70 (s, 3H).
1.00
1.08
1.00
1.05
1.05
2.03
1.00
2.01
f1 (ppm)

1532

# 715 Compound synthetic route



## Supplementary Files

This is a list of supplementary files associated with this preprint. Click to download.

- SCA1715SupplementaryMaterialsNCB.pdf